SPECTRAL AND TEMPORAL INTERROGATION OF CEREBRAL HEMODYNAMICS VIA HIGH SPEED LASER SPECKLE CONTRAST IMAGING

by

Rex Chin-Hao Chen

A Thesis Submitted in

Partial Fulfillment of the

Requirements for the Degree of

Master of Science

in Engineering

at

The University of Wisconsin-Milwaukee

December 2015

ABSTRACT

SPECTRAL AND TEMPORAL INTERROGATION OF CEREBRAL HEMODYNAMICS VIA HIGH SPEED LASER SPECKLE CONTRAST IMAGING
by

Rex Chin-Hao Chen

The University of Wisconsin-Milwaukee, 2015
Under the Supervision of Professor Ramin Pashaie

Laser Speckle Contrast Imaging (LSCI) is a non-scanning wide field-of-view optical imaging technique specifically developed for cerebral blood flow (CBF) monitoring. In this project, a versatile Laser speckle contrast imaging system has been designed and developed to monitor CBF changes and examine the physical properties of cerebral vasculature during functional brain activation experiments.

The hardware of the system consists of a high speed CMOS camera, a coherent light source, a trinocular microscope, and a PC that does camera controlling and data storage. The simplicity of the system's hardware makes it suitable for biological experiments.

In controlled flow experiments using a custom made microfluidic channel, the linearity of the CBF estimates was evaluated under high speed imaging settings. Under the camera exposure time setting in the range of tens of micro-seconds, results show a linear relationship between the CBF estimates and the flow rates within the microchannel. This validation permitted LSCI to be used in high frame rate imaging and the method is only limited by the camera speed. In an in vivo experiment, the amount of oxygen intake via breathing by a rat was reduced to 12% to induce the dilation of the vessels. Results demonstrated a positive correlation between the

system’s CBF estimates and the pulse wave velocity derived from aortic blood pressure.

To exemplify the instantaneous pulsatility flow study acquired at high sampling rate, a pulsatile cerebral blood flow analysis was conducted on two vessels, an arteriole and a venule. The pulsatile waveform results, captured under sampling rate close to 2000 Hz. The pulse of the arteriole rises 13ms faster than the pulse of the venule, and it takes 6ms longer for the pulse of the arteriole to fall below the lower fall-time boundary. By using the second order derivative (accelerated) CBF estimates, the vascular stiffness was evaluated. Results show the arteriole and the venule have increased-vascular-stiffness indices of 0.95 and 0.74. On the other side, the arteriole and the venule have decreased-vascular-stiffness indices of 0.125 and 0.35. Both vascular stiffness indices suggested that the wall of arteriole is more rigid than the venule.

The proposed LSCI system can monitor the mean flow over function activation experiment, and the interrogation of blood flow in terms of physiological oscillations. The proposed vascular stiffness metrics for estimating the stroke preliminary symptom, may eventually lead to insights of stroke and its causes.

Keywords: Cerebral Blood Flow Monitoring, Blood Flow Pulse Wave Analysis, High Speed Laser Speckle Contrast Imaging, Vascular Stiffness Index.

To
my father, Harry Chen, my mother, Amy Lin,
and
Richard Harrod

TABLE OF CONTENTS

LIST OF FIGURES

LIST OF TABLES

ACKNOWLEDGMENTS

My most sincere thanks go to my advisor and mentor, Dr. Ramin Pashaie. I thank him for introducing me to the wonders and frustrations of scientific research. I thank him for his guidance, encouragement and support during the development of this work. He has been teaching me all about self-discipline in career development, laboratory work and scientific communication. Especially, during the last moment of thesis revision and defense preparation, his instructions and patients allow me to grow tremendously in scientific communication skills. Without his help and support, I could not finish this dual Master's degree program.

I am indebted to my committee members: Dr. Brian Armstrong, Dr. Kevin Rarick, and Dr. Yongjin Yuan. They have provided, with kindness, their insight and suggestions, which are precious to me.

Dr. Kevin Rarick is the first biologist that I work with. His expertise and insights helped the project significantly. I am deeply grateful to him for the long experiments and discussions we had, which helped me gain valuable experiences in biological study and exploration of unknown research questions.

My sincere thanks also go to Dr. R David Heathcote, who provided the living tadpoles as the project sample, and Dr. Woo Jen Cheng, who provided the resource of microfabrication facilities and gave me specific instructions on making microfluidic devices.

I want to express my sincere gratitude to past and present members of Bio-Inspired Sciences and Technologies (BIST) Lab. Especially, I thank Mehdi Azimipour, Farid Atry, Mahya Sheikhzadeh, Ghazal Azarfar, Israel De La Rosa, Alana Soeharto,

Tamara Omari, Sarvenaz Memarzadeh, Amy Kaczmarowski, Ryan Baumgartner, and Seth Frye for their support and friendship.

I would like to express my eternal gratitude to my father and my mother for their everlasting love and support.

Chapter 1

Introduction

1.1 Background and Motivation

Brain strokes are known as cerebrovascular incidents. They happen when poor blood flow in the brain results in cell death. Strokes can lead to permanent loss of sensory functions, disabilities or death. They are the third leading cause of death in the United States and are the major cause of adult disability. More than 14,000 people die each year from strokes in the United States, and approximately 795,000 people suffer from strokes. About 600,000 of these are first attacks, and 185,000 are recurrent attacks. Strokes have significant impact on the society.

There are many causes which can lead to strokes. Typical causes are bleeding and blockages. In particular, blockages happen when arteries become too narrow, and blood cells collect and form blood clots. On the other hand, vascular autoregulation dysfunction is the major cause of hemorrhagic strokes where the high blood pressure flow causes the diseased vessels to burst.

The use of genetic modified animals with sophisticated imaging instrumentation can provide insights to the causes of strokes and support the improvement of surgical treatments to minimize the damage induced to the brain.

The standard instruments currently used to study the hemodynamics of cerebral blood flow are Laser Speckle Contrast Imaging (LSCI), Doppler Ultrasound Spectroscopy, Doppler Optical Coherence Tomography (OCT) and 2-photon Microscopy. Since these instruments have limitations and because the blood flow

activity spans a great scale in spatial and temporal resolutions, these instruments have been used interchangeably. In particular, there are three main challenges that are faced by blood flow imaging in cerebral cortex:

1. Lack of spatial resolution
2. Inability to monitor blood flow vascular geometry simultaneously
3. Lack of temporal resolution

Lack of Spatial Resolution and Inability to Monitor Blood Flow Vascular Geometry Simultaneously

There are two common in vivo blood flow monitoring techniques including Laser Doppler Flowmetry (LDF), which measures the changes of CBF as a single value over a circular region with high temporal resolution, and Particle Image Velocity (PIV), which detects blood flow velocity within one single vessel segment with high spatial resolution. However, due to LDF's limited spatial resolution and since PIV is limited to single vessel segments, neither method can monitor the spatiotemporal process of developing strokes and the way brain reacts to cerebrovascular incidents.

Lack of Temporal Resolution

Arteriovenous malformations (AVM) are the tangle of abnormal blood vessels connecting arteries and veins in the brain and the inexistence of the capillaries between arterioles and a venule. AVM often causes lack of autoregulation of blood flow. As a result, the pressured flow enters venules and veins, and potentially cause damages to the vascular wall of venules or induce hemorrhagic strokes.

In fact, the blood flow in the brain, instead of being stable and constant, it is highly pulsated by the heart beats and is an oscillatory flow wave. The amplitude of

this oscillatory wave can address the difference between the blood flow of AVM's venule and the normal venule.

When monitoring the hemodynamics of the tangle part of AVM, the instrument with superior temporal resolution is needed, because superior temporal resolution can allow the oscillatory part of blood flow information being characterized and analyzed.

The dynamical aspect of cerebral blood flow has not been a primary focus of the clinical community, and only minimum experimental data has been acquired over the last sixty years. The primary reason for this deficit is the limitation of temporal resolution of our current instruments.

Table 1. 1 Blood flow monitoring techniques

Method	Velocity components	Spatial resolution (um)	Measure-ment duration (s)	Perfusion information of	Remarks
Scanning laser Doppler	**1**	**10^{1}[a]**	**10^{0}[b]**	**Vascular geometry**	**Standard diagnostics tool[c]**
Multi-probe (full field) laser Doppler	**1**	**10^{2}[d]**	**10^{-2}[e]**	**Vascular geometry**	**Under development**
Profile laser Doppler	**Standard 1[f], up to 3[g]**	**10^{-1}[h]**	**10^{-3}**	**N.A.**	**The technique has not yet been applied to in vivo blood flow monitoring**
Laser speckle contrast imaging	**1**	**10^{1}[i]**	**10^{-2}[j]**	**Vascular geometry**	**Standard research tool for animal model**
Particle image velocimetry	**Standard 2, up to 3[k]**	**10^{-1}[l]**	**10^{-3}**	**Vessel segments**	**Used in animal research**
Ultrasound particle image velocimetry	**2**	**10^{2}[m]**	**10^{-2}[n]**	**Vessel segments**	**Used in animal research**
Nuclear magnetic resonance imaging	**Standard 1, up to 3[o]**	**10^{2}[p]**	**10^{-2}[q]**	**Vessel segments**	**Used in human research**
Doppler OCT	**1**	**10^{0}[r]**	**10^{1}**	**Vascular geometry**	**Used in both human and animal research**

[a] Retina perfusion measurements Michelson et al. (1995) [1]
[b] For a 256 · 64 pixel area Michelson et al. (1995) [1]
[c] Briers (2001) [2] and Pape et al. (2001) [3]
[d] Typical value for skin perfusion measurements. Systems are rather optimized for large imaging areas
[e] For a 256 · 256 pixel area inclusive data processing Serov et al. (2005) [4]
[f] Czarske et al. (2002)[5]
[g] Two components: Büttnerand Czarske (2006) [6]. Three components introduced at the GALA Fachtagung 2006, Göttingen
[h] Büttner et al. (2005)[7]
[i] Typical value for cerebral blood flow measurements
[j] Yuan et al. (2005) [8]
[k] Three components can be measured with a two camera set-up. Arroyo and Greated (1991)[9]
[l] Smith et al. (2003)[10]
[m] Zheng et al. 2006 [11]. Limited by the wavelength of ultrasound.
[n] Zheng et al. 2006 [11]
[o] Markl et al. (2003) [12]
[p] Bauer et al. (2001) [13]
[q] Per slice (Markl et al. (2003)[14]; Nezafat et al. 2005 [15])
[r] Devor et al. (2012) [16]

1.2 Whole Field Blood Flow Measuring Techniques

Among all the in vivo blood flow imaging methods, there are some techniques that can monitor the whole vascular geometry simultaneously including scanning Laser Doppler Flowmetry (SLDF), Full Field Laser Doppler Flowmetry (FFLDF), Laser speckle contrast imaging (LSCI) and Doppler Optical Coherence Tomography (DOCT).

In the cortical area of a human, the size of vessels range from sub-millimeters to micrometers. The following table shows the sizes of vessels in a human vascular network. By using LSCI and SLDF in cortical vascular imaging, the resolution can resolve down to the level of arterioles and venules. DOCT can resolve the vessels down to the capillary level with volumetric velocity information. Despite the limited resolution of Laser Doppler Flowmetry, it has other applications in monitoring skin perfusion.

Table 1. 2 Vascular sizes in human

	Aorta	Arteries	Arterioles	Capillaries	Venules	Veins	Vena cava
Diameter (mm)	**25**	**4**	**0.05**	**0.008**	**0.02**	**5**	**30**

Pulsatile flows additionally require a temporal resolution that is at least half the period of the highest relevant harmonic. Particularly, rats' heart rate are usually around 300-400 beats per minutes, which is about 5 times larger than human. To resolve the rats' pulsatility without introducing aliasing distortion, a hundred data point would require within one cardio cycle. Among current techniques that can provide velocity information within a vascular geometry, only LSCI have achieved the sample rate of 200 Hz with the 5ms exposure time.

In conclusion, in terms of the spatial resolution SLDF, DOCT might provide adequate resolution or even superior resolution compared to LSCI, but considering the temporal resolution required, the LSCI becomes the best candidate that can provide higher temporal resolution while maintaining adequate spatial resolution.

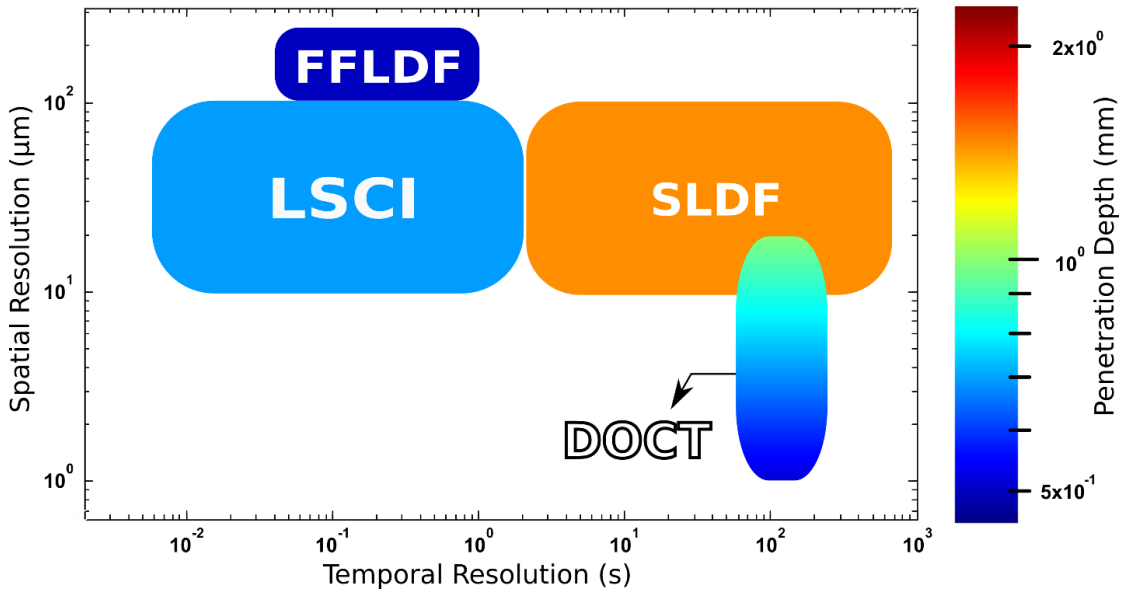

Figure 1. 1 Whole field blood flow monitoring techniques

1.3 Goals

Stroke has a complicated development process. In particular, the cerebral hemodynamics response is a time varying response controlled by many physical and biological factors. To investigate what's under the hood, a tool that has integrated features can help researchers to record and analysis data. Currently, integrated cerebral blood flow monitoring devices are still not fully available. The standard tools either lack spatial resolution or temporal resolution. In this project, monitoring the temporal and spatial variation of cerebral hemodynamic response are the project's main focus. A monitoring instrument that integrated present Laser Speckle Contrast Imaging techniques with the theorem of pulse wave analysis had been developed.

From the theory and empirical verification, the developed system not only provide the capability to monitor hemodynamic responses, but also can assist researchers to investigate the properties of vascular structure, and may eventually provide further understanding of cerebrovascular functions. The front-end of the system consists of a coherent source, a focusing lens and a camera. The back-end of the system are acquisition and analysis software developed for a PC. The major purposes of developing this system are:

a. monitoring the spatial and temporal variations of relative mean flow,
b. spontaneous monitoring of pulse wave contour within individual vessels ,
c. analyzing vascular stiffness within individual vessels.

Monitoring the spatial and temporal variations of relative mean flow

Ischemic stroke happens when blockage occurs in a focal region and lasts for 3-15 minutes. This type of analysis can allow regional blood flow variation to be monitored during the process of ischemic stroke and treatment practice. It can provide insights for building the mechanism of cerebrovascular function and recovery.

Spontaneous monitoring of pulse wave contour within individual vessels

This technique has an enhanced sample rate to resolve the pulse wave contour on specific vessel. The obtained pulse wave contour can provide dynamic parameters describing vascular structure.

Analysis of vascular stiffness in individual vessels

Through the blood flow pulse wave analysis, the second order derivative of pulse wave can provided characteristic of vascular stiffness.

Chapter 2

Literature Review and Theoretical Framework

2.1 Literature Review- Laser Speckle Contrast Imaging

In 1976, Goodman [17] pointed out that due to our lack of knowledge regarding the detailed structure of microscopic structures, it is necessary to discuss speckle patterns statistically. He published statistics that describe such speckle patterns. This statistical result has been well verified experimentally by the results published in 1970 [18].

In 1981, Briers and Fercher [19] applied the work of Goodman [20] on the statistical properties of speckles and developed the first theoretical model linking speckle contrast and speckle correlation time which can indicate the relative perfusion of blood flow.

In 1981, Briers and Ferchers claimed the particle speed related to correlation time has a ratio of $V_p \approx 0.1/\tau_c\ \mu m/s$. In the same year, Bonner and Nossal [21] took more factors into account (i.e. particle size), and the relation reduced to $3.5/\tau_c\ \mu m/s$. These results show the exact physical relation between ICTs (Inverse Correlation Time) and the particle speed requires further examination.

In 1981, Briers and Fercher [19] related correlation time to speckle contrast level by assuming the sample undergoes a Lorenztian Velocity distribution [19]. This relationship was later expanded by Bandyopadhyay [22] in 2005 via incorporating a more rigorous relationship initially proposed by Goodman [17].

In 2001, Dunn was the first one who applied it to study Cerebral Blood Flow (CBF) in a rat brain [23], and then many studies of functional brain activation were conducted in the rat somatosensory cortex [24], cortical spreading depression of the migraine model [25], and vasoconstrictive vascular coupling during focal ischemic depolarizations [26], and collectively LSCI was also adopted for many blood flow research projects in skin burn recovery [27] and retinal vasculature imaging [19].

In 2005, the blood flow levels asserted by LSCI was compared and validated against results produced by Scanning Laser Doppler Flowmetry [28].

In 2006, Li et al. [29] used temporal sampling to estimate the speckle contrast, instead of spatial sampling, can offer a better spatial resolution.

In 2008, Duncan brought detailed insight to optimize speckle contrast imaging, in terms of the effect of speckle size [30] and window size [31] on speckle contrast. In the same year, he proposed a proper statistical model [32] for velocity distribution, and stated blood flow dynamics would be better described by Volgit distribution which is a combination of both Brownian (Lorenztian distribution) and ordered (Brownian distribution) motion.

In 2007, Cheng *et al.* [33] proposed the use of $1/K^2$, the inverse of squared contrast level, to be a metric of LSCI instead of Inverse correlation time.

In 2008, Parthasarathy *et al.* [34] used a suspension of microspheres to verify the overall nonlinear relationship between the contrast level, exposure time and correlation. Parthasarathy *et al.* [34] proposed a modified speckle model that takes multiple exposure time images into account for reducing the estimation error.

Up to 2009, typical Laser Speckle Contrast Imaging frame rate lies between 10 to 30 frames. Duncan [35] used a 200 frames per second CMOS camera to explore the possibility of acquiring pulse wave velocity within the rat brain.

The simplicity of LSCI setup has made possible to integrate this method with many other modalities. In 2008, Jones et al. integrated LSCI with multi-reflectance imaging for acquiring oxygenation level [36] along with cerebral blood flow. In 2014, Kalchenko et al. [37] and Gramer et al. [38] integrated LSCI with fluorescent imaging and positron emission tomography (PET).

In 2010, Rege *et al.* [39] showed the cross line of 27 vessels' Blood Velocity Profiles (BVP) were well curved fitted with parabolic curves, and claimed that their observation supported the consistency of LSCI with the fluid dynamics.

In 2012, Dunn et al. [29] integrated 2-photon and LSCI and investigated the penetration depth of LSCI and suggested that the scattering properties in the sample should also be calibrated.

In 2015, Kazmi el at. [42] highlighted the use of calibre variation to correct the tissue scattering properties in ICTs produced by LSCI.

2.2 Speckle and its Origins

When an object is illuminated by a highly coherent light source, a granular pattern is produced. Figure 2.1 shows a typical Speckle Pattern. This granular pattern is produced through the mutual interference of a set of wave fronts.

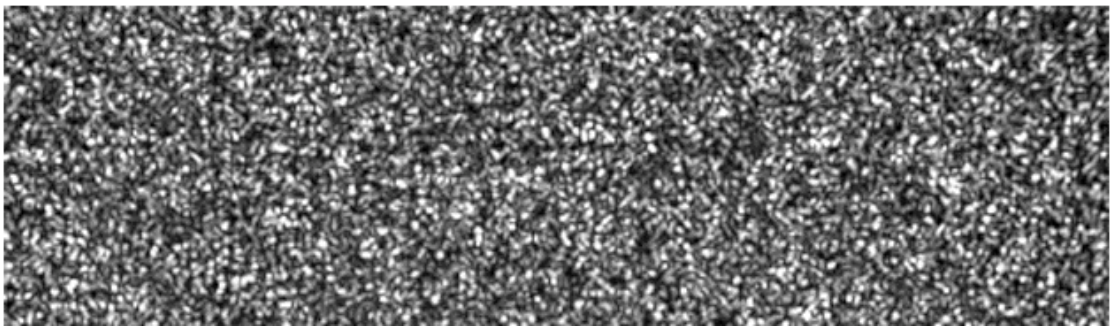

Figure 2. 1 Laser speckle pattern reproduced from [43]

Figure 2.2 (a) shows the free space laser speckle is a random interference pattern produced by the coherent addition of scattered laser light with slightly different path lengths and every point on the receiving screen receives photons coming from everywhere in the illuminated area, and result in the point on the receiving screen consisting of photons that have random combination of phases to create a grainy pattern known as speckle pattern.

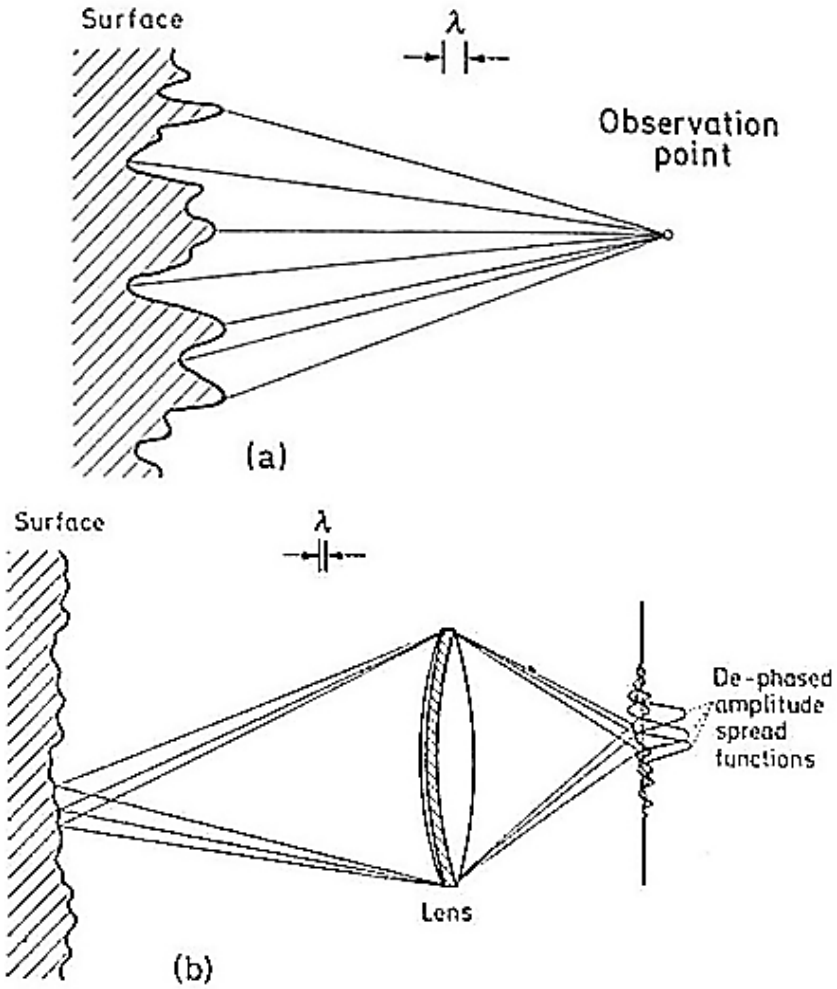

Figure 2. 2 Physical origin of speckle for (a) free-space propagation, (b) an imaging system. Reproduced from [44].

In Figure 2.2 (b), a optical rough surface is illuminated by laser light. The scattered photons are collected and imaged onto a camera through a lens. When the diffraction limited point-spread function of the lens is broad compared to surface variations, many de-phased coherent contribution coming from many independent surface areas add at each image point and result in constructive and destructive interference which produces a granular pattern known as the speckle pattern.

2.3 Dynamic Speckle

As most imaging systems consider speckle as noise that degrade image quality, considerable effort has been spent for eliminating speckles. In fact, speckle is an information carrier that carries information of the scattering site, such as scattering site dynamics or geometry, which can be obtained by analyzing speckle pattern.

For example, if the scattering site undergoes fluidic motion with moving scatterers such as red blood cells, then a rapid changing speckle pattern is observed, due to the constant changes of the scattering site geometry, the speckle pattern would constantly decorrelate from the previous pattern .

In particular, the type of movement of speckles is often described as boiling movement, which holds no obvious relationship with its previous moment. It is randomized and also holds no obvious relationship with the type of movement the scattering media undergoes. However, as the scattering media flow rate increases, the scattering site geometry changes more rapidly and the speckle pattern decorrelates from its previous pattern faster. Therefore, approaches such as quantifying the temporal or spatial statistic of speckle can provide some information about the scattering site.

2.4 Laser Speckle Contrast Imaging (LSCI)

Laser speckle contrast imaging (LSCI) is a wide field view optical technique that is specifically developed to imaging cerebral blood flow. In LSCI, a stack of time-integrated speckle pattern is acquired through a digital camera, and the acquired speckle patterns are analyzed through statistical analysis in both spatial and temporal approaches. Figure 2.6 shows a typical schematic of laser speckle contrast imaging

setup. A sample is illuminated by a highly coherent light source with 45 degree incident angle. Then, the scattered light is collected by the focusing optics and projected onto a camera sensor.

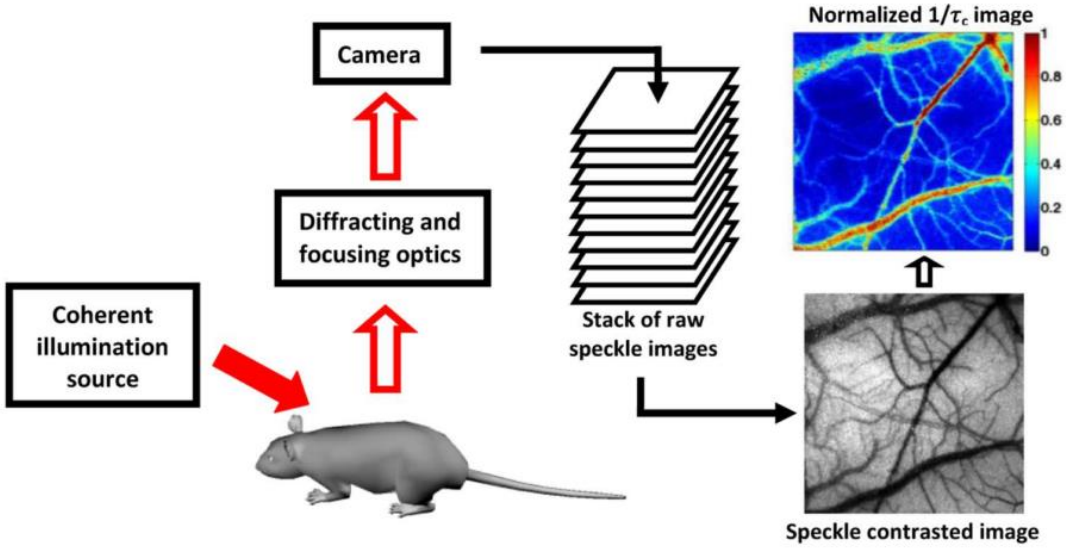

Figure 2. 3 Laser Speckle Contrast Imaging (LSCI) framework. Reproduced from [45].

Traditionally, a spatial and temporal highly coherent light source with wavelengths around 600 nm to 900 nm are used. However, a wavelength outside of this range can also be tailored according to the application. For example, the brain tissue has lower absorbance at larger wavelengths. Small wavelengths produce smaller speckles which increases the spatial resolution.

Typically, a CCD/ CMOS camera with more than 8 bit dynamic range is used. Since In animal studies, the fluidic motion undergoes in the sample varies significantly from sample to sample. The exposure time setting is specifically chosen for different animals or different parts of the body. In rodent cerebral blood flow imaging, typical choices are 5 ms to 20 ms.

Next, a stack of raw speckle images are collected and speckle contrast analysis is applied to obtain speckle contrast images. Each pixel contrast value can then be

converted into a value $1/\tau$ indicative of the speed to construct a relative blood flow map.

Frame rates typically lie between 10 to 30 frames per second. However, higher frame rates are achievable. In particular, the advanced CMOS cameras might bring up new applications. Duncan [35] used a 200 frames per second CMOS camera to explore the pulse wave velocity within the rat brain.

The simplicity of this setup has made it possible to integrate this system with many other modalities such as fluorescent imaging [37] as shown in Figure 2.4 (i), positron emission tomography [38], two-photon microscopy for 3D blood flow dynamic analysis [40], [41], multi-reflectance imaging for acquiring the oxygenation level [36] and surgical microscope for a surgeon to observe the blood flow during an operation as shown in Figure 2.4 (ii). The miniature system allows animal freely moving while observing the cerebral blood flow as displayed in Figure 2.4 (iii).

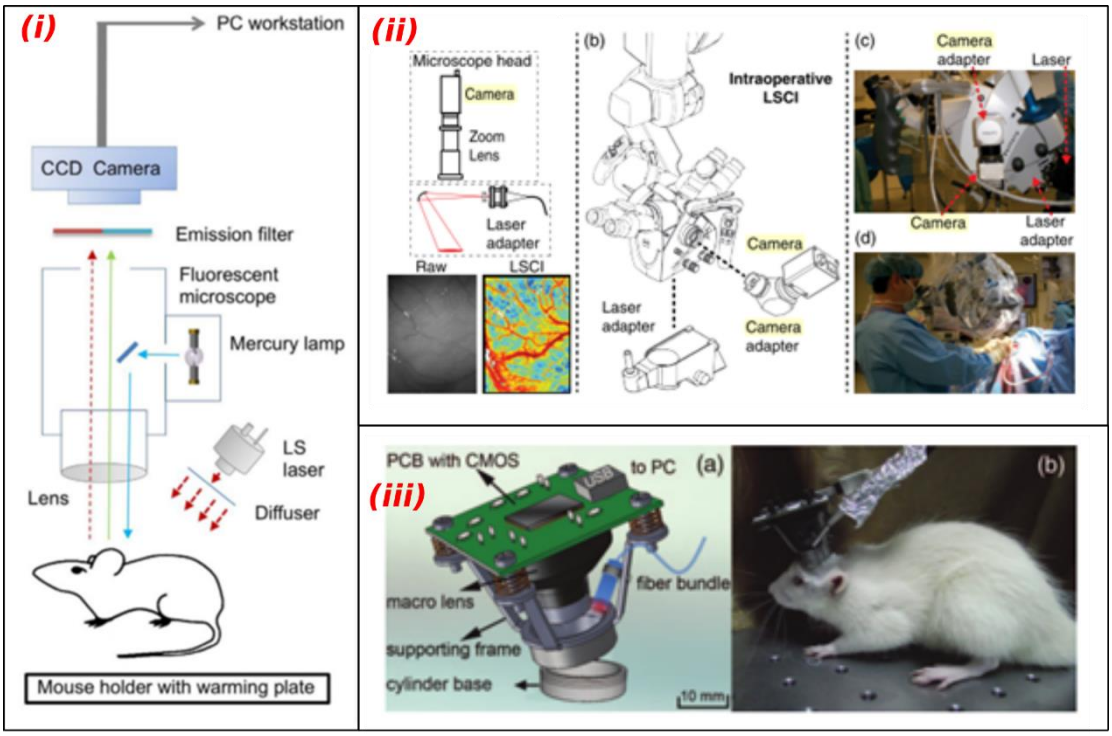

Figure 2. 4 (i) LSCI integrated with fluorescent imaging [37] *(ii) LSCI integrated with an intraoperative surgical microscope* [46] *(iii) Miniature system LSCI* [47]

2.5 Speckle Contrast

In LSCI, the sample is illuminated at 45 degree incident angle. Then the scattered light is collected by a focusing optics and imaged onto a camera sensor. Since the speckle patterns captured by camera sensor are time integrated patterns, any alternation of the instantaneous speckle pattern within the exposure time of camera can cause blurring effect on the captured images. When the site geometry is fixed (the instantaneous speckle pattern is fixed), then the time-integrated speckle pattern is observed without blurriness. However, when the sample site undergoes fluidic motions (the instantaneous speckle pattern alternates during the exposure time), then a blurred time-integrated speckle pattern is observed. The following images demonstrate that the blurring effect caused by flow rate increases for the same exposure time setting.

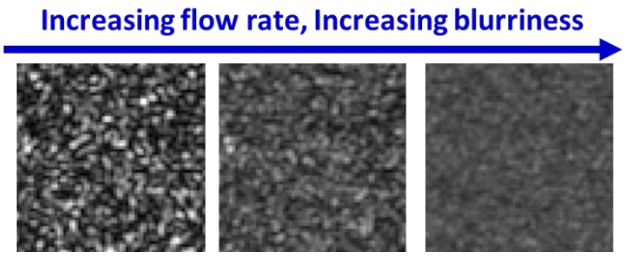

Figure 2. 5 Time-integrated speckle patterns with increasing flow from left to right. Reproduced from [48].

Speckle contrast Ks is a quantitative estimate of the degree of blurriness. In a typical analysis window, a square window of 5 by 5 pixels or 7 by 7pixels is selected. Then, the speckle contrast Ks is calculated through the standard deviation over the mean intensity within the window:

$$Ks = \frac{\sigma_s}{\langle I \rangle_s}.$$

Equation 2. 1

Three time-integrated speckle patterns above are then converted into speckle contrast maps. The speckle contrast maps show a decreasing trend as the flow rate increases.

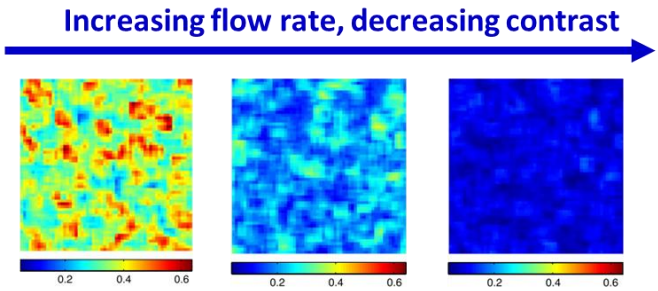

Figure 2. 6 Speckle contrast maps with increasing flow rate from left to right. Reproduced from [48].

The very essence of the LSCI is to quantify speckle contrast for a given exposure duration, and then relate the speckle contrast to the absolute normalized electric field autocorrelation function $g1\,(\tau)$. A subsequent connection between scattering sites dynamics can then be made. In particular, the flow rate of a scattering site is the main interest. Briers and Fercher [5] had brought the first model that links the speckle contrast to the scattering site speckle correlation time. Later, Bandyopadhyay [22] pointed out that there is some mathematical error and inconsistency in Briers and Ferchers model. In the following section, the introduction of the model proposed by Bandyopadhyay, and the way the correlation time relates to the scattering sites dynamics are explained.

2.6 LSCI- Blood flow Index

Laser speckle contrast imaging enables the rapid visualization of blood flow. The contrast level obtained from the ratio of standard deviation and mean intensity is a nonlinear function of both exposure and correlation times. By relating the contrast

level to correlation time and correlation time to particle speed, the quantitative measure of particle speed can be estimated.

Relating Particle Velocity to Correlation Time

A dynamic speckle pattern can be described by the power spectrum of temporal intensity fluctuations. Alternatively, it can also be described as the autocorrelation function of intensity fluctuations. One of the important foci of the autocorrelation function is the correlation time. This variable describes the amount of time needed for the instantaneous speckle pattern to decorrelate into a new independent speckle pattern. The inverse of correlation time (ICT) is related to the rate by which light is being scattered off when it is incident on a moving particle. It is a commonly reported metric by Dynamic Light Scattering (DLS) techniques, such as Laser Doppler Flowmetry and Diffusive Laser Spectroscopy.

To estimate the relation between the particle speed and ICTs, many researchers had assumed the sample dynamics follow a random Gaussian or Lorentzian velocity distribution with a mean around zero. This correlation time, τ_c, can be related to the particle velocity, V_p, by:

$$V_p = \frac{\lambda}{2\pi\,\tau_c},$$

Equation 2. 2

where λ is the wavelength of the incident light. When a red laser is used, the relation reduces to $V_p \approx 0.1/\tau_c\ \mu m/s$ (Brier *et al.* [49]). Bonner and Nossal [21] took more factors into account (i.e. particle size), and the relation reduced to $3.5/\tau_c\ \mu m/s$.

Since the factor that relates correlation time to particle velocity (proposed by Brier *et al. and* Bonner *et al.)* have 1.5 order of magnitude difference, the exact physical relation of the ICTs with particle speed requires further examination, where more specimen structure and/or scattering properties such as particle density needed to take into account.

Relating Correlation Time to Speckle Contrast Level

For Laser speckle flowmetry methods, the need for relating the correlation time to the speckle contrast level is clearly shown. By assuming that the sample undergoes a Lorenztian Velocity distribution, Fercher and Briers first proposed a simplified model that related the speckle contrast values to the speckle correlation time, τ_c, which was later expanded by Bandyopadhyay [22] by incorporating a more rigorous relationship initially proposed by Goodman.

Therefore, the speckle correlation time can be extracted from the following relationship [22]:

$$K = \frac{\sigma_s(T)}{\langle I \rangle_s} = (\beta \frac{e^{-2x} - 1 + 2x}{2x^2})^{1/2},$$

Equation 2. 3

where $x = \frac{T}{\tau_c}$. This relationship highlights that the observed contrast is a function of the exposure duration of the camera as well as the speckle correlation time and the instrumentation factor β [22]. Based on the relationship, a small value of the speckle contrast corresponds to a small value of τ_c which indicates fast moving speckle pattern and a contrast level close to unity corresponds to a large value of τ_c and that is a stationary speckle pattern.

Ramirez-San-Juan *et al.* has further investigated three types of the velocity distribution: Lorentzian, Gaussian and modified Gaussian [50].

Duncan *et al.* [51]pointed out that Lorentzian distribution can only describe Brownian motion.

$$K = \frac{\sigma_s(T)}{\langle I \rangle_s} = \sqrt{\frac{\tau_c}{2T}\left(1 - \exp\left(-\frac{2T}{\tau_c}\right)\right)},$$

Equation 2. 4

Secondly, Ramirez *et al*. [50] investigated the same relation for ordered motion assuming the velocity distribution is Gaussian. The resulting equation is given,

$$K = \frac{\sigma_s(T)}{\langle I \rangle_s} = \sqrt{\frac{\sqrt{\pi}}{2}\frac{\tau_c}{T} erf\left(\frac{T}{\tau_c}\right)},$$

Equation 2. 5

where the integration of the normalized autocorrelation function of a velocity distribution should be equal to the correlation time τ_c. However, this is not the case in the above equation. As a result, Ramirez *et al.* proposed using the following alternative Gaussian expression:

$$K = \frac{\sigma_s(T)}{\langle I \rangle_s} = \sqrt{\frac{1}{2}\frac{\tau_c}{T} erf\left(\frac{\sqrt{\pi}\,T}{\tau_c}\right)}.$$

Equation 2. 6

In Figure 2.10, speckle contrast value is plotted as a function of the exposure time over τ_c under the assumption of Lorentzian, Gaussian and Gaussian modified velocity distribution. For high speckle contrast level, Gaussian and Lorentzian

distribution show an order of magnitude difference, whereas the Gaussian modified distribution shows good agreement with the Lorentzian distribution when the contrast level is less than 0.5. In fact, as Duncan stated Blood flow dynamics would be better described by Volgit distribution which is a combination of both Brownian (Lorenztian distribution) and ordered (Gaussian distribution) motions.

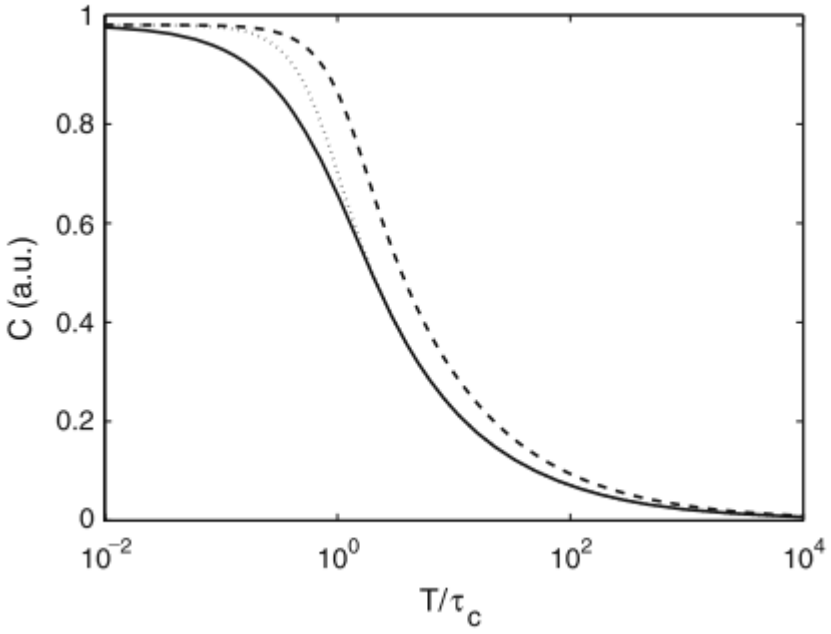

lab

Figure 2. 7 Contrast (C) vs integrated time/Correlation time for Lorentzian velocity distribution (solid), Gaussian velocity distribution (dashed) and alternate Gaussian velocity distribution (dotted).Reproduced from [50].

Conclusion on Relating Contrast Value to Particle Speed

From the time speckle contrast was used as a measure of dynamic speckle and a relation between autocorrelation function and contrast, discovered by Goodman, to the point people deduced the correlation time by assuming the velocity distribution and related the correlation time to the particle velocity, many challenges have been dealt with over the last two decades. There are still several unsolved issues including an unknown ratio between particle speed and correlation time due to the unknown particle size and an ill-posed issue when relating speckle contrast to the correlation due to the

complex velocity distribution, which is preventing LSCI and other laser Doppler and/or speckle flowmetry techniques from measuring the absolute particle velocity.

Nonetheless, strong correlations between speckle-based flow measures and alternative perfusion indices across single vascular suggest that flow dynamics within any given region of interest may be accurately captured and can be used to quantify the temporal variations as well as the hemodynamic response in the cerebral blood flow.

For all practical purposes, the ICT still serves as a regional perfusion index in arbitrary physical units.

This is still an active research area. Each year, many advances and improvements are made to better estimate flow dynamics relevant to monitoring cerebral blood flow.

Application of Correlation Time Model

Brier and Ferchers [19] were the first group officially enabled the technology of laser speckle contrast imaging and they also proposed a correlation time model (equation 2.3). Since then many have pointed out its mathematical error and inappropriate assumption of flow distribution. Several papers were published new corrections; however, the latest proposed models did not bring much changes numerically. Equation 2.7 is a commonly used equation proposed by Bandyopadhyay [22]

$$K(T,\tau_c) = \frac{\sigma_s(T)}{\langle I \rangle_s} = \beta^{0.5}\left\{\frac{\tau_c}{T} + \frac{\tau_c}{2T^2}\left[\exp\left(-\frac{2T}{\tau_c}\right) - 1\right]\right\}^{0.5}$$

Equation 2. 7

According to Bandyopadhyay's model [19], the speckle contrast equation has a variable which is the ratio between speckle correlation time and the camera's exposure time. To demonstrate the relationship of correlation time and exposure time, we assume a sample perfusion brings a correlation time of 0.03 ms to 31 ms. A relation between speckle contrast versus camera's exposure time ranging from 10μs to 5s are demonstrated in Figure 2.7. At a fixed exposure time, higher flow rate (represented by lower correlation time) has lower contrast value. Dunn and Boas reported a typical cerebral blood flow correlation time ranging from 0.2ms to 5ms [52]. The highlighted envelope shows the correlation time of typical cerebral blood flow changing from 0.2ms to 5ms. Since, in this envelop, the largest difference in contrast values happens at 5ms exposure time, this proves that 5ms exposure time can provide the largest sensitivity for rodent cerebral blood flow applications.

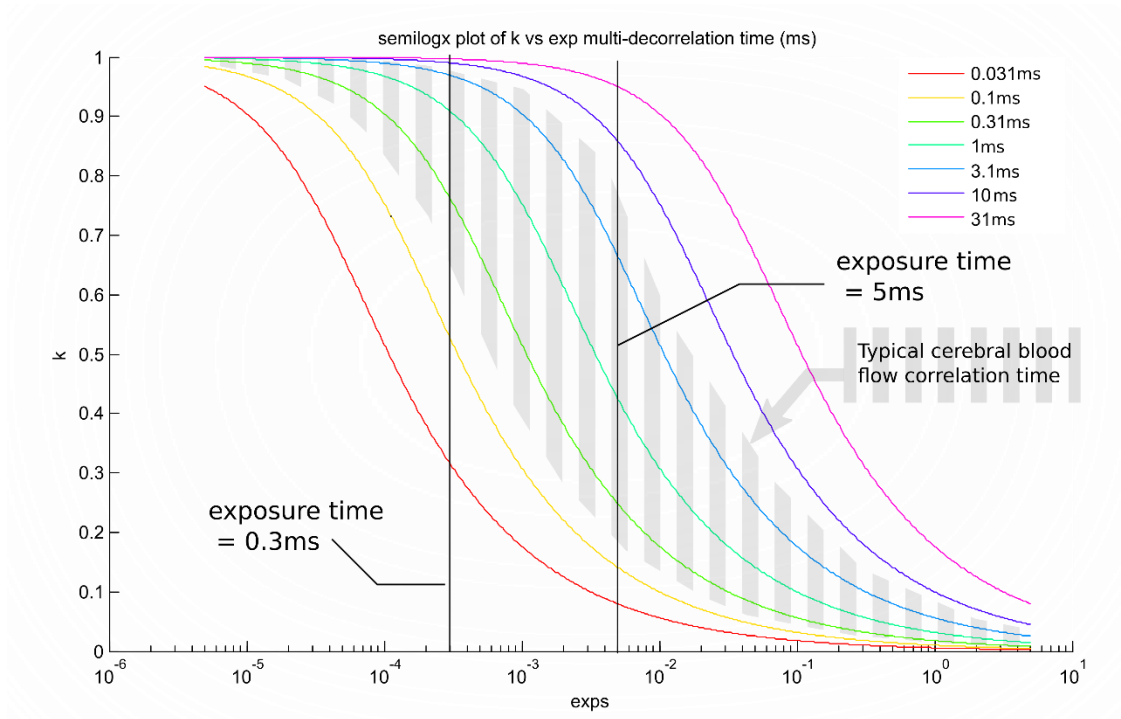

Figure 2. 8 Spatial contrast K versus exposure time T when the object correlation time ranges from 0.03 ms to 30ms

Factors that Affect Correlation Time Estimate

There are many factors that affect the perfusion index. The first group of factors is the factors of specimen imaging geometry, such as static scattering, hematocrit, depth of scatterers, and structural scattering properties. This group of factors vary from sample to sample and are the major obstacle that prevent LSCI measuring the absolute velocity of scatterers. However, it does not prevent quantitative relative cerebral blood flow to be measured. Since the imaging geometry properties do not change drastically, the ICT blood flow index, relative to the baseline ICT, can accurately capture and describe the temporal fluctuations of blood flow within any given region of interest.

The second group of factors are the parameters of the imaging system and speckle contrast analysis, such as speckle to pixel size, non-polarized detection and analysis window size. The effect of mismatch between the speckle and pixel size, non-polarized light detection would result in the reduction of speckle contrast estimation. Analysis window size affects the amount of speckle that the method takes into account for the estimation and it holds the trade-off between estimation accuracy and the spatial resolution.

Penetration Depth

LSCI is based on the dynamic scattering of temporal coherent photons within a volume of tissue. It served as a volumetric motion detector that integrates the motion volumetrically to produce a 2D perfusion map. The penetration depth of LSCI depends on the degree of multiple scattering and the local vascular anatomy of tissue. Up to 700 μm deep is accounted for 95% of acquired signal [53]. He et al. [54] have improved

the penetration depth further by using line beam scanning illumination; however, that penetration depth obtain at the expense of the sample rate.

2.7 LSCI- Imaging Parameters

The hardware of laser speckle contrast imaging typically consists of three major parts: a coherent light source, imaging optics and a camera.

Coherent Source

The first major component is a highly coherent light source which incorporates a non-aspheric lens that expand the beam size to cover the region of interest which ranging from a few millimeters to several centimeters depending on the sample under study. An incident angle of normal to 45 degrees are used to collect backscattered photons and eliminate the photons which experienced specular reflection at superficial area. The choices of wavelength arise from 600nm to near inferred, since the diffraction ratio outweigh the absorption ratio for wavelengths larger than 600nm within the brain tissue. For the speckle pattern to be fully evolved, a longitudinal laser source is suggested and its bandwidth would determine the coherent length which further affects the largest scattering path. The typical coherence length of a narrow bandwidth laser governs the largest scattering path in the brain tissue and allows the blood flow to be sampled [42]. Adequate amount of photons falling on the camera sensor can allow the use of the full sensor dynamic range. In both of the following settings, the choice of having higher laser power would be required.

First, when the system incorporates with a polarizer to increase speckle contrast and reduce the specular reflection, more than half of the power is filtered out.

Secondly, to enable the high sample rate for imaging, a short exposure time is used. To allow adequate amount of light falling on the senor within this short period, a high power laser is required.

Imaging Optics

The second major part is the imaging optics. When coherent light illuminates an optically rough surface, backscattered photons are collected by a focusing lens or an objective and then imaged onto a camera sensor. Several imaging parameters are discussed here. The magnification of focusing lens/objective is decided based on the area of interest. Typically, a low magnification of 2x-10x are preferred in cerebral blood flow imaging to obtain a wide field of view (i.e. few millimeters by few millimeters). Speckle size is a major parameter of the imaging optics. It affects the contrast-analysis-window size and the highest obtainable contrast value of the system. A window size that is 3-5 times larger than the speckle size is needed to establish a meaningful statistics. When a larger window is used for larger speckle size, the specificity performance of the system is lowered. On the other hand, if smaller speckles relative to pixel size are obtained, a single pixel will receive the intensity that is spatially averaged by several speckles, and ultimately this spatially-averaged intensity causes some reduction in the spatial variance of acquired intensities, and reduces the highest obtainable speckle contrast of the system.

Speckle size

Since there is a tradeoff between high specificity and establishing statistical robustness, the size of speckle has to be chosen carefully. By determining the diffraction limit, the smallest speckle radius can be calculated as

$$r_{speckle} = 2.44\lambda(1 + M)\, f/\#,$$

Equation 2. 8

where λ is the wavelength of light, M is the magnification of the imaging system, and $f/\#$ is the f number of the system. Kirkpatrick *et al.* [30] reported the result of spatial sampling rate against the speckle contrast (showed in Figure 2.8) achieved by both simulations and experiments. They stated that if the speckle pattern is sampled below the Nyquist rate, which is the ratio N=2 ($r_{speckle}/r_{pixel}$), the contrast value of the speckle pattern rapidly falls well below the theoretical asymptotic limit of unity. They also reported that to maximize the range of observed contrast values, the minimum speckle size should be greater than 2 [30]. Before Kirkpatrick et al report, it was suggested that the matching speckle size and pixel size (N=1) would maximize the contrast value. Experimental results show the speckle contrast is underestimated by 20% if N=1. Underestimating the speckle contrast would result in a systematic error in the estimation of correlation time τ_c, which can be absorbed through introducing parameter β in speckle model which determines the correlation time τ_c. However, this reduction of highest obtainable speckle contrast would still reduce the sensitivity of spatial and temporal variations during speckle contrast imaging.

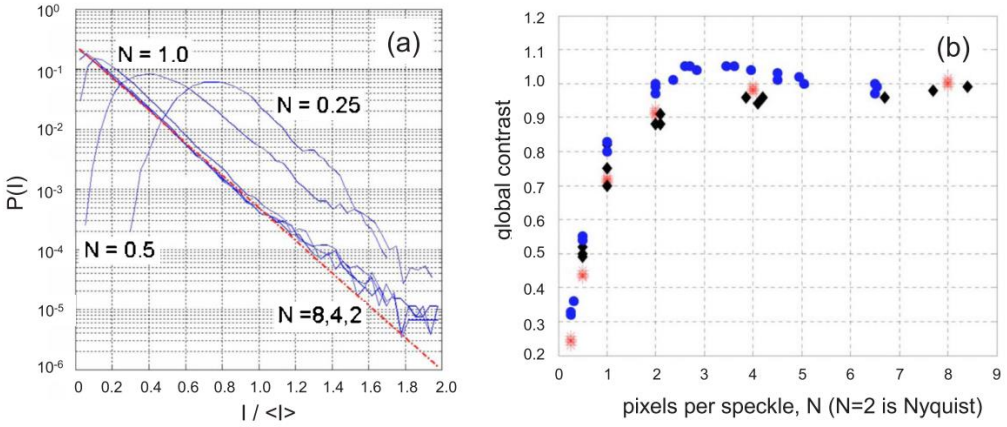

Figure 2. 9 (a) Speckle intensity probability distribution function considering different numbers of pixels per speckle N and the distribution is an exponential for N=2. (b) The

speckle contrast for a static medium equals its expected value of 1 when N=2. Reproduced from [55].

Polarized light detection

When a group of coherent polarized photons are passing through a dense random material (such as biological tissue), scattering happens which modifies the direction and polarization of the incident photons as Figure 3.3 illustrates.

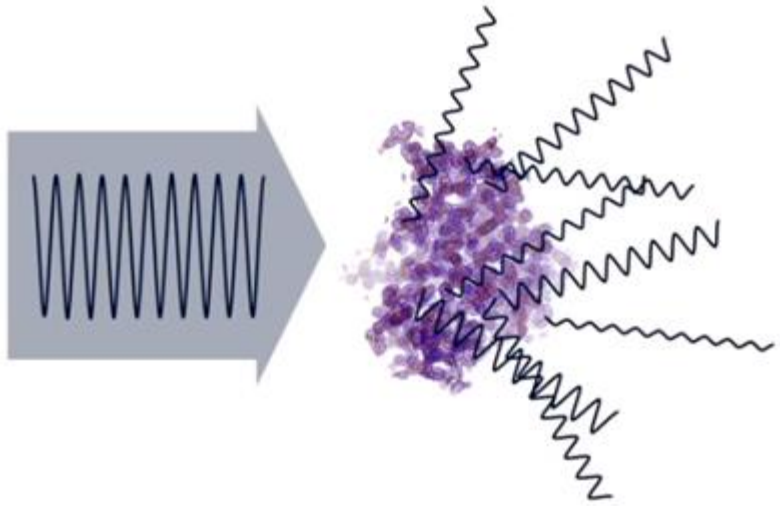

Figure 2. 10 Scattering of polarized light. Reproduced from [56].

Furthermore, when polarized photons backscatter from polarized-light-illuminating sample, some photons might experience surface reflection, and some experience multiple scattering where they have a random polarization distribution. By doubling the incident light power and placing a polarizer between the sample and camera with the polarization that is normal to the polarization of the laser as Figure 3.4 illustrates, reflected photons that contain no sample dynamic information can be filtered out, since the polarization of laser is preserved through the reflection. Other photons carrying information about the sample's dynamics experience multiscattering within the sample. Part of these photons pass through the polarizer and arrive at the camera sensor.

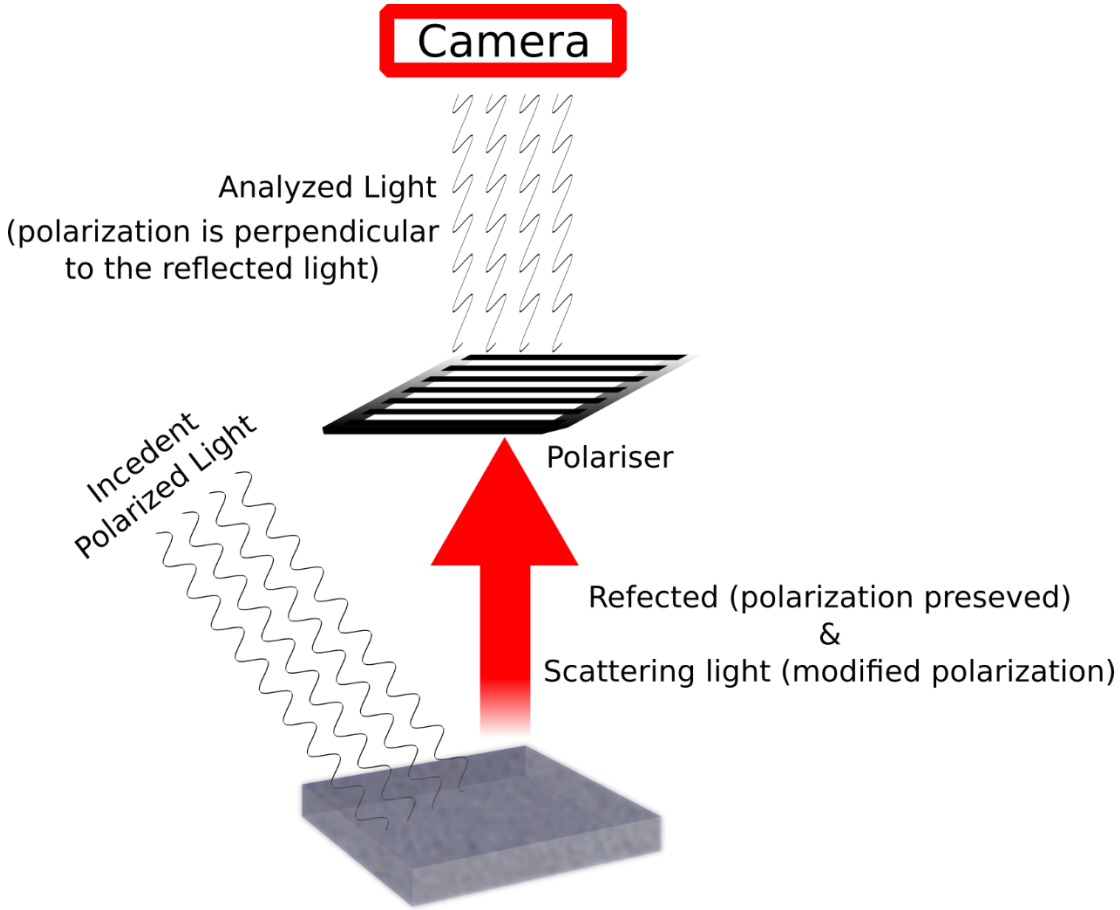

Figure 2. 11 Polarized light detection

Some researchers suggest that using a polarizer is necessary to produce valid results, since the correlation time model is developed based on polarized detection [22].

Some researchers neglect the polarizer in the system due to the difficulty of increasing the optical power twice, and rely on β coefficient of Siegert equation to compensate the effect of non-polarized light detection.

Camera

The third major component of laser speckle contrast imaging is the camera. The backscattered photons coming from the sample pass through the imaging optics, and a subjective speckle pattern is formed on the sensor array. Typically the choice of camera is a monochrome camera with enough number of pixels to resolve multiple

vessels and the dynamic range of 8~12 bits. Both CCD or CMOS cameras can be used; however, a CMOS camera potentially offers better performance regarding its higher frame rate. High dynamic camera with cooling case is not necessary due to the fact that usually adequate number of photons are received in a typical application using biological tissue as a highly scattering media and the dominating noise is usually the shot noise. Richards *et al.* [57] verified results of an expensive high dynamic range camera and a low cost webcam camera, and both produced the same results which supports the statement that it is not necessary to use expensive high dynamic range cameras for Laser speckle contrast imaging.

Nonetheless, advanced CMOS technology allows using the high speed CMOS camera and recording with high frame rates enables more temporal averaging to diminish the speckle noise for the monitoring of cerebral blood flow systematic variation.

For high speed imaging, higher quantum efficiency, larger pixel size, senor filling ratio and low readout noise are important, since only a limited number of photons arrive at each pixel under sub-milliseconds exposure time. Additionally, using a global shutter would be mandatory to avoid unwanted blurring effect caused by possible motions.

On the other hand, to optimize the spatial resolution, one can reduce the size of speckles by choosing better optics. As the magnification and the wavelength are fixed, to use the full resolution of the system, a smaller camera pixel size has to be chosen accordingly.

2.8 LSCI- Contrast Analysis Schemes and Parameters

There are two major contrast neighborhood schemes based on spatial and temporal analysis. Most of the published contrast schemes are developed based on these two analyses.

Spatial Speckle Contrast Analysis

Choosing the neighborhood in the spatial domain is probably the oldest LSCI [19]. A number of pixels has to be selected for calculating the standard deviation and mean value. Insufficient data cannot draw a meaningful estimate of contrast, while a large window results in a poor spatial resolution. A 5x5 or 7x7 pixels window is commonly used. Duncan has shown that 7x7 pixels window is a good tradeoff between meaningful statistical measure and resolution. The spatial speckle contrast analysis provides the highest temporal resolution while sacrificing the spatial resolution.

Calculating speckle contrast based on spatial sampling under the presence of static scattering media can cause an additive offset which increases the speckle contrast. If this value is not calibrated carefully, both absolute blood flow and blood flow variation will be underestimated.

Being computationally expensive is an issue in the spatial speckle analysis. It takes few seconds for computing a single image in Matlab even with an updated computer, since significant amount of data reading counts are required for the calculation of a moving window. However, many have published modified algorithms to optimize the computation in spatial analysis. These methods have significantly reduced the data reading counts for computing the spatial contrast and have allowed real time imaging of spatial analysis to become feasible.

Temporal Speckle Contrast Analysis

Selecting the contrast neighborhood only in temporal domain can provide high spatial resolution, while compromising the temporal resolution. Typically, 40 to 80 [58] consecutive raw images are used and every pixel within the image is picked up and processed with its temporal consecutive images' pixels located at the same coordination on the camera sensor. Theoretically, it can be beneficial to use higher spatial resolution in monitoring slow hemodynamic responses such as stroke or hypoxia that happens in seconds. But its temporal resolution might not be able to monitor fast hemodynamic variation produced by pulsatility or breathing. Additionally, less amount of information can establish an acceptable measure of speckle contrast under temporal scheme by choosing an integration time longer than correlation time of speckles. When the exposure time is longer, speckles are decorrelated before the integration ends. This scheme is advantageous since having all the pixel information in the contrast neighbor are statistically independent of each other. Cheng reported that a minimum number of 15 consecutive pixels can establish meaningful speckle statistics [59].

Static scattering does not introduce spatial-temporal speckle pattern alternation. Instead an unavoidable increase happens at the mean intensity. This means the intensity increase result in a decrease in speckle contrast and also a disturbance in the estimation of absolute correlation time and blood flow. However, this disturbance does not prevent the estimation of relative blood flow, since the disturbance can be cancelled out through the normalization.

Comparing Temporal and Spatial Contrast Analysis

Spatial analysis needs 7x7 pixels to obtain a meaningful speckle contrast statistics. On the other hand, the temporal analysis only requires a minimum of 15 consecutive pixels. If there is a fixed amount of data, temporal analysis can provide more information than spatial analysis.

In several studies, temporal speckle contrast analysis is shown to have the capability to avoid artifact coming from static tissue, and allow the relative blood flow monitoring to be robust while the spatial contrast analysis requires calibration. Parthasarathy et al. [60] proposed a multiexposure scheme for the spatial contrast scheme to calibrate the presence of static tissue.

The computational inexpensiveness of the temporal speckle contrast analysis has drawn another advantage over the spatial analysis. However, advances in computing technology and the efficiency of spatial contrast algorithm enabled the real-time processing of speckle contrast analysis in both spatial and temporal domains.

Contrast Neighborhood Size

The window size for calculating the speckle contrast has its effect on the spatial resolution and contrast estimation accuracy. Larger window sizes can give better estimation, but lower the resolutions. From a theoretical perspective, the small window size might result in wrong estimated speckle contrast. Duncan *et al.* [31] reported that a 3x3 window size has an underestimated error of 13%, whereas the large window size has an ±3% error. Figure 2.12 shows the median parameter of contrast distribution is affected by $N_{pixels}^{1/2}$. Academia is currently settled on $N_{pixels}^{1/2}=7$, as Figure 2.12 indicates. $N_{pixels}^{1/2}=7$ sits on the bended part of the curve, which provides a reasonable trade-off between the spatial resolution and accuracy contrast estimation.

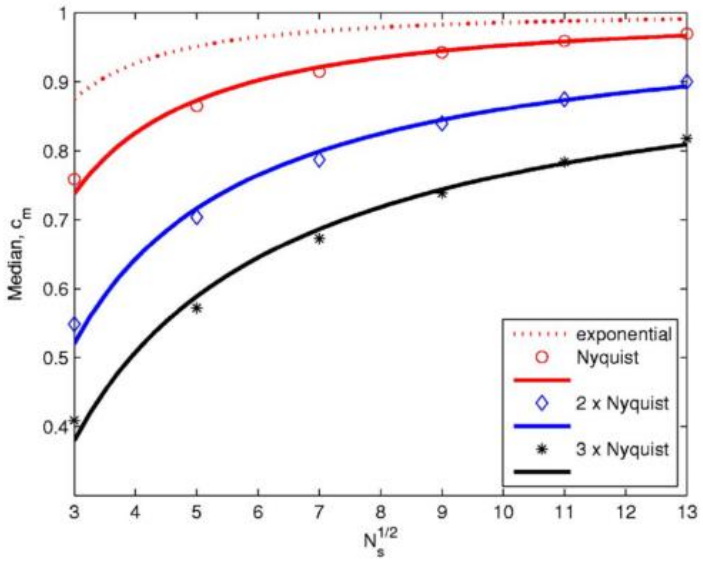

Figure 2. 12 Median Parameter of contrast distribution as a function of local neighborhood and speckle size. Reproduced from [31].

2.9 Velocity Profile Measured in a Tube

When the flow in a pipe is steady, and the pipe roughness is not considered, a laminar flow condition is assumed. The flow profile of a laminar flow has the highest velocity at the center of the tube and the flow at the wall has 0 velocity, the descending curve from the center to the wall of a fully developed laminar flow appears to have a parabolic velocity profile. This parabolic velocity profile can be described as:

$$u(r) = 2V_{avg}\left(1 - \frac{r^2}{R^2}\right),$$

Equation 2. 9

where V_{avg} is the mean velocity, R is the radius of the inner tube wall, and r is the position of interest. The mean velocity is half of the maximum velocity.

$$V_{avg} = \frac{1}{2}U_{max}.$$

Equation 2. 10

2.10 Pulse Wave Analysis

Pulsatility pattern can be in the form of pressure, flow or volume. The patterns have slight differences in different parts of the body. They all originated from the ventricular activity. The main arteries have high compliance where the smaller artery and arteriole have specific protein to help vessels constrict and raise the vascular resistance. This vascular resistance regulates the pressured flow which is significant at arterioles, and allow the gentle flow enter capillaries. This flow is further deformed by the resistance of capillaries and the blood volume leakage. Therefore, the pulsatility pattern not only has the feature of central large artery but it also has the local vascular properties.

Pulsatility pattern is often used to investigate the cardiovascular health. For instance, fingertip Photoplethysmogram (PPG) signal is often used as the morphology of the arterial pressure pulse. Some common features such as Systolic Amplitude, Pulse Width, Augmentation Index and Large Artery Stiffness Index have been quantified to predict the health of major artery and peripheral vessels. A typical PPG signal and its second order derivatives, which often called acceleration plethysmogram (APG), are shown in Figure 2.13.

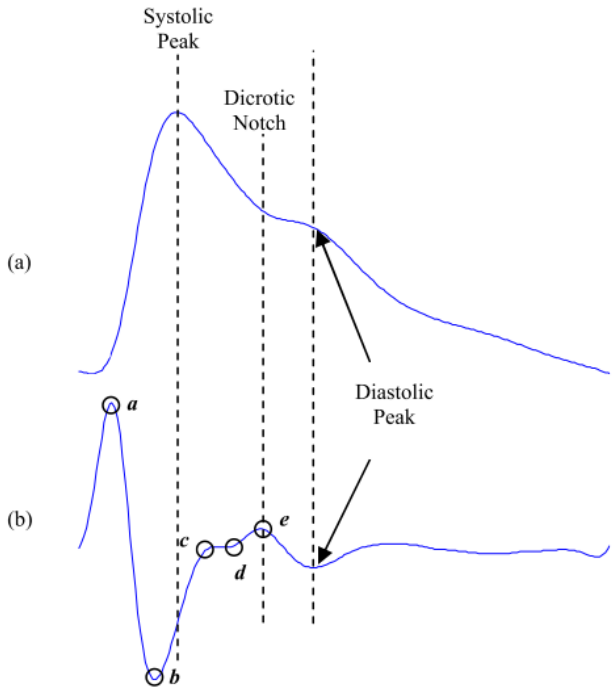

Figure 2. 13 A typical PPG signal and its second order derivatives. Reproduced from [61].

The wave components of APG in Figure 2.13 (b):

- a-wave: early systolic positive wave
- b-wave: early systolic negative wave
- c-wave: late systolic reincreasing wave
- d-wave: late systolic redecreasing wave
- e-wave: early diastolic positive wave

The e-wave represents the dicrotic notch as shown in Figure 2.13 (b). Dicrotic notch corresponds to the closure of the aortic valve and the sudden drop in pressure during the heart valve closing up phase.

The amplitude and timing of a, b, c, d, and e peaks of APG are often used to evaluate the systemic and the peripheral vascular health.

$$Increased\ Vascular\ Stiffness\ Index = \frac{b_{amp}}{a_{amp}}$$

Equation 2. 11

Takazawa *el al.* [62] reported that the amplitude ratio of b/a reflects the vascular stiffness. A healthy artery has the ratio of 1. Imanaga *et al.* found direct evidences [63]. That b/a increases significantly with in patients, who have atherosclerosis.

$$Decreased\ Vascular\ Stiffness\ Index = \frac{c_{amp}}{a_{amp}}$$

Equation 2. 12

Takazawa *et al.* also demonstrates the c/a ratio reflecting decreased vessel stiffness.

2.11 Conclusion

There are many literatures explored different aspects of LSCI in terms of its principles, merits and applications. In LSCI literatures, the highest sample rate of LSCI is 200Hz. To resolve pulsatile flow in rat cerebral, a sample rate that is higher than 500Hz is required. In following chapter, the methodologies of validating LSCI higher sample rate applications and monitoring pulsatile flow are discussed.

Chapter 3

Methodology and System Structure

According to the topics covered in the last two chapters for this project. We developed a LSCI system that can monitor functional brain activation, pulsatile flow and vascular stiffness of animal cerebral cortex.

The front-end of the system consists of optics and camera; the back-end of the system consists of the data acquisition and analysis software. The system is tailored individually for two major goals of the project: monitoring functional brain activation and pulsatile flow measurements. The details of hardware, imaging parameters and data analysis procedures are discussed in this chapter

3.1 Research Materials and Components

Software: National Instruments Labview 2011

National Instruments Labview Vision package

Matlab 2013

ImageJ

Hardware: PC –1T Bytes Hard Disk Drive (HDD), 160G Bytes Solid State Drive (SSD), 8G Bytes RAM

Laser Diode – HL63133DG, Thorlabs, Inc.

Microscope – 2.5x-10x, Trinocular Edmund Optics Inc.

CMOS camera – HS-2000M-RA, Emergent Vision Technology

Others – Double boom stand, Adjustable collimation tube, Laser Driver, Polarizer, Rotational mount, Network interface card

3.2 Hardware Structure

The structure of the system is depicted in Figure 3.1. In this project, a 637nm 170mW laser diode (HL63133DG, Thorlabs, Inc., Newton, NJ, USA) is used, and it is driven by a constant current laser driver (LDC205C, Thorlabs, Inc., Newton, NJ, USA). The laser diode is housed in an adjustable collimation tube (LTN 330A, Thorlabs Inc., Newton, NJ, USA). By turning the front part of the tube, the beam size is adjusted to cover the region of interest. To image the sample under illumination, a 2.5x-10x trinocular microscope (Edmund Optics Inc., Barrington, NJ, USA) which has two 10x eyepieces was chosen. A high speed camera (HS-2000M-RA, Emergent Vision Technology, Coquitlam, B.C., Canada) is installed on the microscope. The camera can capture up to 333 frames per second (fps) at full frame and more than 10k fps at reduced pixels. A wire rendered the captured image to a PC through a 10 Gigabit Ethernet network interface card. For data acquisition, Labview 2011 is used to acquire images and restore the data to a 160 GB solid-state drive.

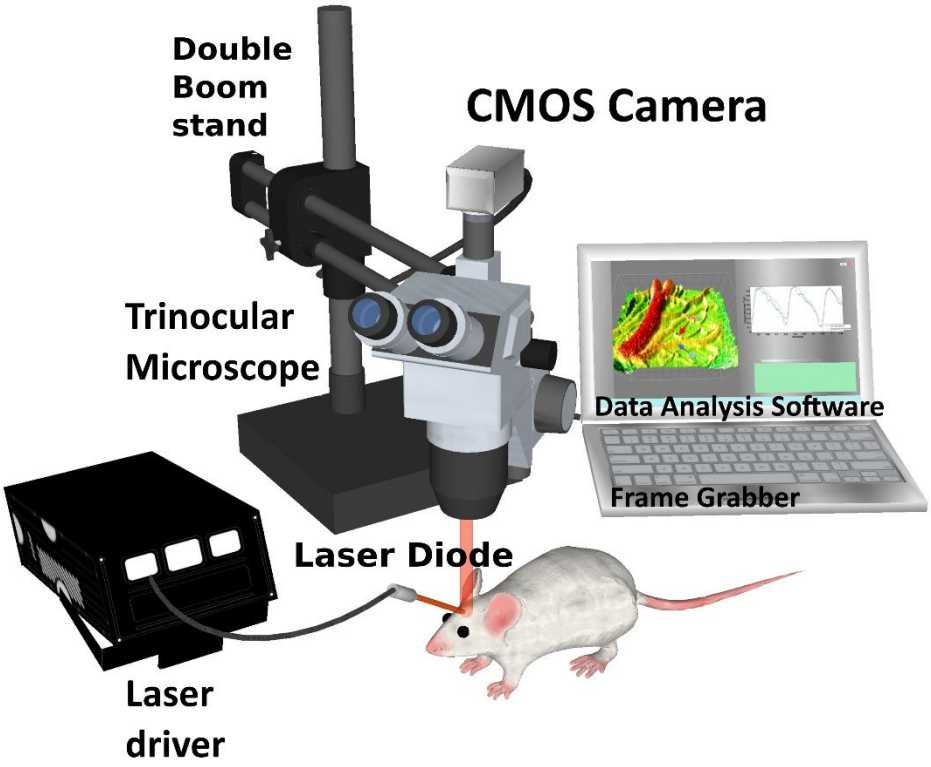

Figure 3. 1 Animated drawing of Laser speckle contrast imaging

High Power Red Laser Diode

A 170 mW optical power 637nm Laser Diode (HL63133DG, Thorlabs, Inc., Newton, NJ, USA) was selected to provide adequate amount of light for the high speed imaging applications. The red visible wavelength was selected for the low absorption coefficient and to ensure enough light backscatters from dense brain tissue. The laser diode is driven by a laser diode driver (LDC205C, Thorlabs, Inc., Newton, NJ, USA) operating in constant current mode.

A typical Laser Diode requires temperature cooling socket to prevent the temperature effect which can unstable the laser diode. However, the bulky cooling socket does not permit the ease of use during animal experiments. In this project, an adjustable collimation tube is selected to perform the beam size adjustment easily (LTN 330A, Thorlabs Inc., Newton, NJ, USA). This collimation tube includes a Laser Diode mount with an aspheric lens. This component not only allow the ease of

positioning, but also allow to perform the beam size adjustment easily. However, since the design of this housing does not allow the temperature of the diode to be controlled, a short operation time is permitted during the high speed imaging section. A 30mW optical power is used during the function activation studies where the temperature of laser is stabilized for 45 degree maximum operating temperature. An optical power test shows that the laser is stable over a period of 23 minutes for the mean optical power of 29.93 mW and the standard deviation of 100 μW.

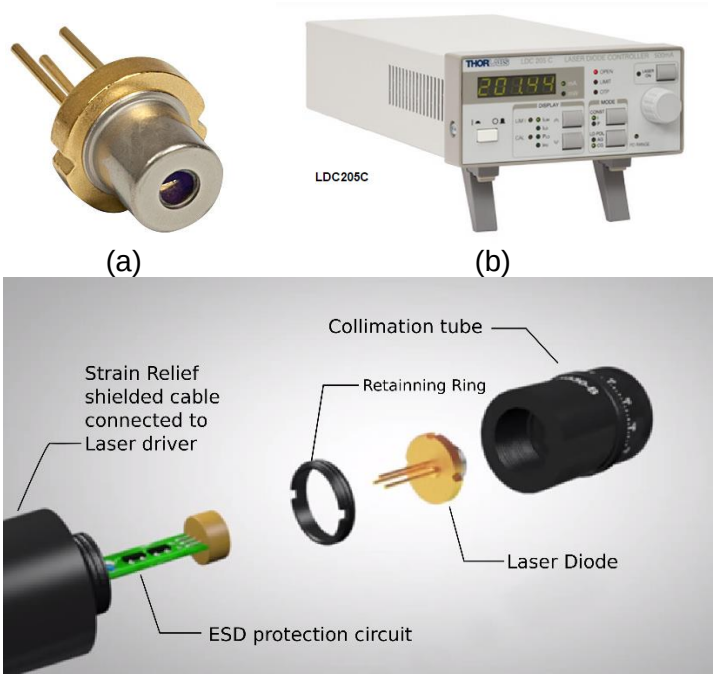

(a) (b)

(c)

Figure 3. 2 Components used for illumination (a) The 5.6mm diameter housing of the laser diode (b) The constant current laser driver (c) The adjustable collimation tube where an adapter between the 5.6mm LD and retaining ring is not shown in the figure

Microscope and Polarizer

A 2.5x to 10x trinocular microscope (Edmund Optics Inc., Barrington, NJ, USA) is seated on a double arm boom stand. The microscope has two 10x eyepieces for ease of navigation. It has a working distance of 36mm. When 2.5x magnification is used, a 7.5 mm diameter field of view is obtained through the eyepiece, and a field of

view of 4.5mm x 2.5mm diagonal is obtained through a 2/3” camera sensor (HS-2000M).

A nano-particle linear film polarizer (LPVIS100, Thorlabs, Inc., Newton, NJ, USA) for visible light is used. The polarizer is mounted between the microscope and the camera through a rotational mount (CLR1A, Thorlabs, Inc., Newton, NJ, USA) which allows a smooth rotational movement of the mounted optics.

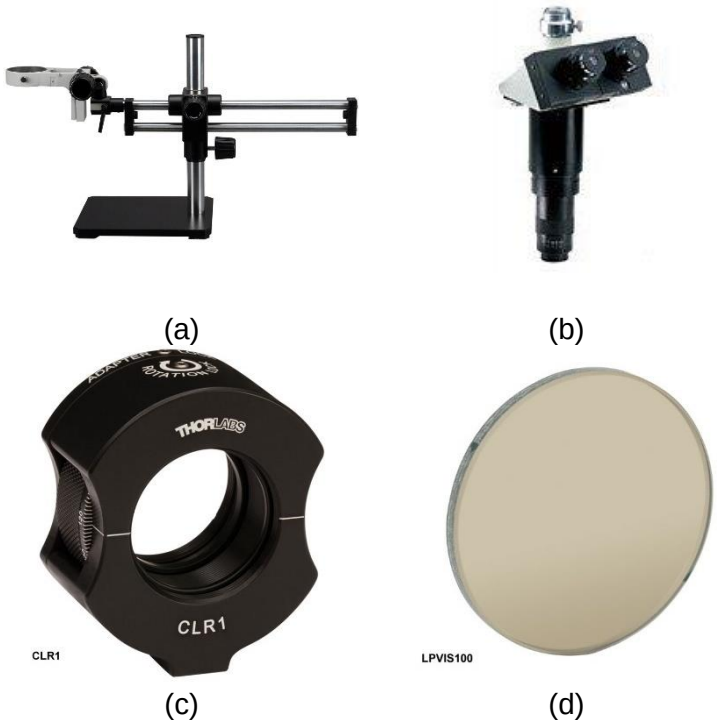

(a) (b)

(c) (d)

Figure 3. 3 Parts used in the imaging optics (a) the double arm boom stand (b) the 2.5x-10x trinocular microscope (c) the rotational mount (d) the linear polarizer

High Speed CMOS Camera

The camera used in this system is a high speed CMOS camera (HS-2000M-RA, Emergent Vision Technology, Coquitlam, B.C., Canada) as Figure 3.5 (a) shows. The 2/3” sensor has 2048 x 1088 pixels. Each pixel has a size of 5.5um by 5.5um. The sensor chip has a spectral response as shown in Figure 3.4. When 637nm is used, the sensor has 55% quantum efficiency. For dynamic range, It has 8 bits and 10 bits. 8 bits per pixel is selected for maximizing the frame transfer rate. This camera uses

10 Gigabits Ethernet as network interface which allows a maximum data transferring rate of 1180 Mbytes/s. The camera has been tested in Labview for real-time data transferring. It can achieve 200 frames per second at full sensor size 1920 x 1088 pixels and 7407 frames per second at a reduced frame size 826 x 36 pixels. Table 3.1 shows the results of real time data rendering test. A higher frame rate is achievable using other programming languages such as C. The camera has a global shutter that prevents the unwanted blurring effect. It has a wide range of exposure time selection ranging from 10 us to 1s.

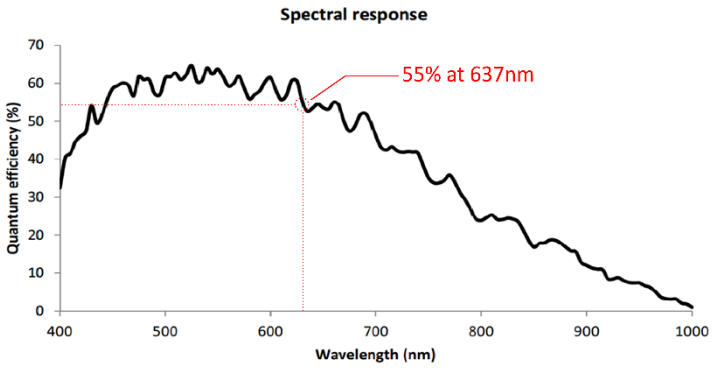

Figure 3. 4 Quantum efficiency of camera sensor

Table 3. 1 Results of real time data rendering test

Frame rate (Fps)	**7407**	**3508**	**1869**	**966**	**394**	**198**	**99**
Width (pixels)	**826**	**698**	**822**	**784**	**769**	**1176**	**2048**
Height (pixels)	**36**	**90**	**142**	**290**	**728**	**946**	**1088**
Transferred data (MB per seconds)	**210.05**	**210.16**	**208.05**	**209.46**	**210.36**	**210.07**	**210.38**

(a)

(c) (d)

Figure 3. 5 The Emergent camera uses 10 GigaEthnet wire to establish the link between the camera and a PC (the PCI 10GigE network interface card is installed on the PC mother board).

3.3 Imaging Parameter and Analyzed Parameter

Function Activation

- Incident angle: 45 degree
- Magnification: 2.5x
- Exposure time: 10ms
- Sensor format: 2048x1088 pixels
- Polarizer Angle: the polarization of detection is perpendicular to the polarization of the coherent source
- Frame Rate: 40fps
- Frames per dataset = 30 (0.75s period of collecting data)
- Record at every 5s
- 30mW optical power

Duration of Function activation experiments ranges from 15 minutes to hours. Since this is relatively long, LSCI image acquisition is configured to optimize the data transfer and storage rate. During experiments, a stack of 40 raw images is acquired every 5 seconds under the frame rate of 30 fps. The frame rate is chosen to cover several cardiac cycles to reduce the pulsatility oscillation. The acquired images are processed using spatial contrast analysis frame by frame in Matlab. The spatial contrast maps in each stack of images are averaged to obtain a reduced noise contrast map. The contrast map is then converted into an Inverse correlation time (ICT) map.

Pulsatile Flow

- Incident angle: 45 degree
- Magnification: 2.5x
- Polarizer Angle: the polarization of detection is perpendicular to the polarization of the coherent source
- Optical power: Up to 150mW

Table 3. 2 Frame-rate table

Exposure time (ms)	**0.25**	**0.5**	**1**	**2.5**	**5**
Frame rate (Fps)	**3508**	**1869**	**966**	**394**	**198**
Width (pixels)	**698**	**822**	**784**	**769**	**1176**
Height (pixels)	**90**	**142**	**290**	**728**	**946**
Frames per dataset	**7000**	**3600**	**1800**	**700**	**400**

The imaging parameter of pulsatile pattern acquisition is optimized based on the limitation of the camera and the data transfer rate. The sensor format sizes are bounded by the data transfer rate of Labview. The acquired images are processed used the same parameter as we mentioned in functional activation studies. To plot pulsatile flow of a vessel, the contour of targeted vessel is manually selected and the

ICT value is averaged over selected area frame by frame. As a result, an ICT time trace of a selected vessel is created.

3.4 Calibration of Speckle Size to Pixel Size Ratio

The speckle size to pixel size ratio is affected by the f-number of the optics, its magnification, and the wavelength of the coherent source. The calibration of this ratio only needs to carry out once for the system. The system is calibrated manually through adjusting the f-number of the imaging system to fulfill the Nyquist criterion and minimize the reduction of speckle contrast.

3.5 Polarized Light Detection Calibration

The non-polarized light detection can lead to a reduction in the speckle contrast. The polarized light detection requires manual calibration in vivo. The process for manual calibration procedure is as folllows:

1. reset the laser current to zero, turn on the camera on live in NI IMAX, open the live histogram window,
2. turn on the laser, slowly increase the current until achieving adequate intensity where the maximum and the minimum intensities are not cropped or saturated,
3. rotate the polarizer until the minimum total intensity is found.
4. readjust the intensity of the source accordingly.

3.6 LSCI Flow Estimate Linearity Verification Experiment in Microchannel Platforms

To verify the linearity of LSCI flow estimate, a microchannel experimental setup is used. A syringe pump perfuses the microchannel with velocity ranging from 0 mm/s to 10mm/s. Two sets of camera parameters were used. For the first set of imaging parameters, we used 75μs exposure time and enabled a frame rate of 9072 fps. Second set of imaging parameter were 300μs exposure time and a framerate of 2980fps. For each velocity, we acquired 9072 and 2980 number of frames distinctively. For the first and second set of parameters, each acquired image was processed by spatial contrast analysis software with a window size of 7x7 pixels to produce contrast maps. A mean contrast value was obtained from averaging the perfusion area and a stack of frames. Then, the correlation time model was used to convert the contrast value to the inverse correlation time.

The relative inverse correlation time was defined as the relative $\tau_c = \frac{\tau_{c0}}{\tau_c}$, where τ_{c0} is the correlation time at a baseline speed of 1mm/Sec. Theoretically, the relative flow estimates are linearly proportional to the controlled flow rates.

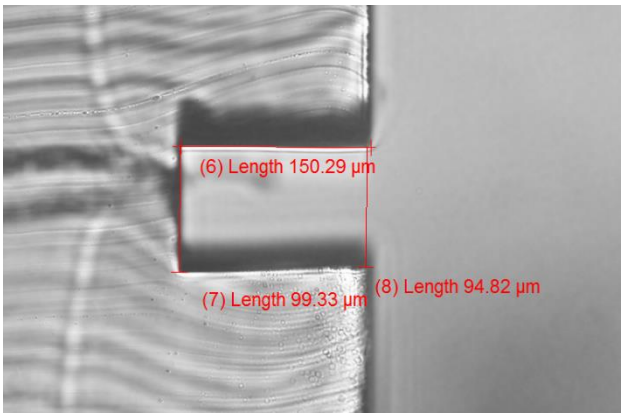

Figure 3. 6 Cross-sections of the microchannel

3.7 Vessel Cross Section Inverse Correlation Time (ICT) Analysis

To increase the signal to noise ratio, multiple cross sections along the same vessel were collected using an automated algorithm to follow the skeleton of the vessel. The procedures of producing the cross-sections are depicted in the following chart. The ensemble average was produced by using multiple cross sections.

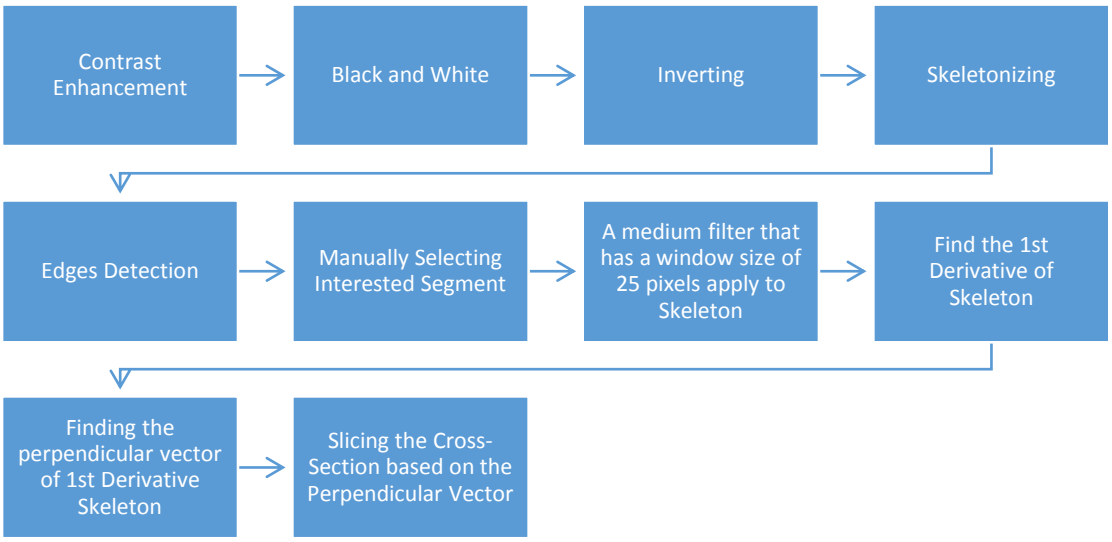

Figure 3. 7 Procedures of slicing multiple cross-sections

3.8 Ensemble Average of Pulsatile Flow

To improve the signal to noise ratio for pulsatility pattern, ensemble average is a common choice among many biological signals such as EKG, EEG, and intracranial pulsatility. The ensemble average clips the pulses based on a reference timing, where the reference timing can either generated from the feature of instantaneous pulses or external reference timing. For example, some researchers use EKG as their reference of timing. The clipped pulses are then averaged to generate a clear ensemble averaged single pulsatile pattern.

In this project, the reference for timing is generated by the signal's local maxima. An interactive peak detector [64] created by Tom O'Haver was used in this project under Matlab environment.

To find the local maximum, autozero, baseline correction, peak amplitude threshold, Gaussian smoothing with window size of 60, and a sweeping window size of 60 were used. We used the iPeak software which slides the sweeping window through all the data points to find the local maximum within the sliding window.

After successfully detecting the reference of timing, the original data were preprocessed with autozero, detrend, and moving average window of 25 data points. Then signals are clipped into individual pulses based on the reference timing.

The last step is averaging the three dimensional array of data with respect to time to create a single beat ensemble averaged flow pattern.

Chapter 4

Experimental Results and Discussion

This chapter is focused on validating the blood flow estimate of LSCI quantitatively using microchannel, validating the algorithms of the ensemble average for eliminating speckle noise in the pulsatile flow pattern and the vascular velocity cross-section, and discerning the merits of LSCI in rodent cerebral cortex and tadpole cardio vasculature. The final part of this chapter is focused on the results of two experiments performing hemodynamic recording during functional brain activation and pulsatile flow in rodent cerebral cortex.

4.1 Calibration of Speckle Size to Pixel Size Ratio

As mentioned in chapter 3, speckle size to pixel size ratio of N=2 is commonly suggested for high spatial specificity while maintaining the statistical robustness of speckle contrast. In this system, the 2.5X to 10X microscope was used, and the magnification of 2.5x was carefully chosen to match the minimum speckle size 2 times larger than the pixel size of the camera. Without the use of apertures, the smallest speckle on the image is around 2 by 2 pixels size in the following image which it represents the spatial sample rate of 2.

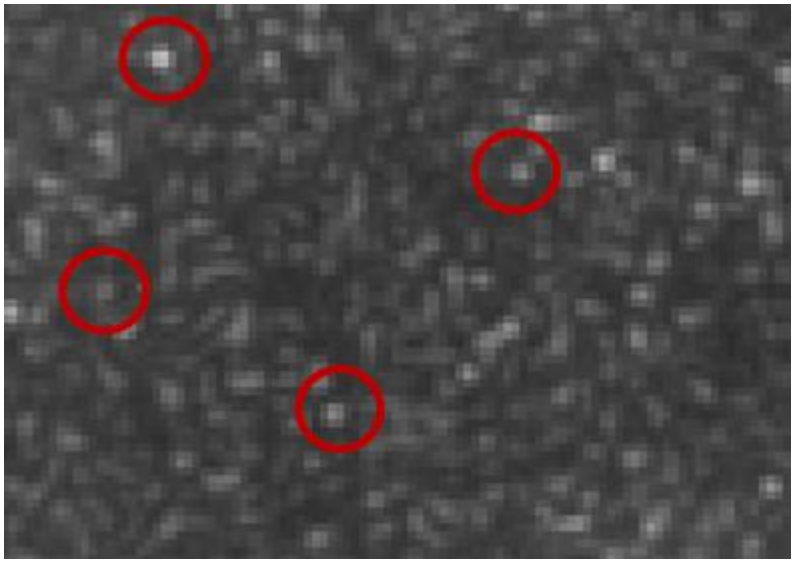

Figure 4. 1 A Laser speckle pattern captured with 2.5x magnification

4.2 Validation of LSCI Flow Estimates Using Microchannel

As mentioned in chapter 3, LSCI is not capable of providing absolute blood flow measurement. However, we can still measure the relative blood flow alternations. In this section, the linearity between the LSCI flow estimate and controlled flow rate in a microchannel is carefully studied.

In this experiment, two exposure time settings that are shorter than commonly suggested 5ms exposure time in cerebral blood flow monitoring were tested. In Figure 4.2, results show the linearity over a range of microchannel flow rate from 0-10mm/s with R^2 (coefficient of determination) of 99.6%.

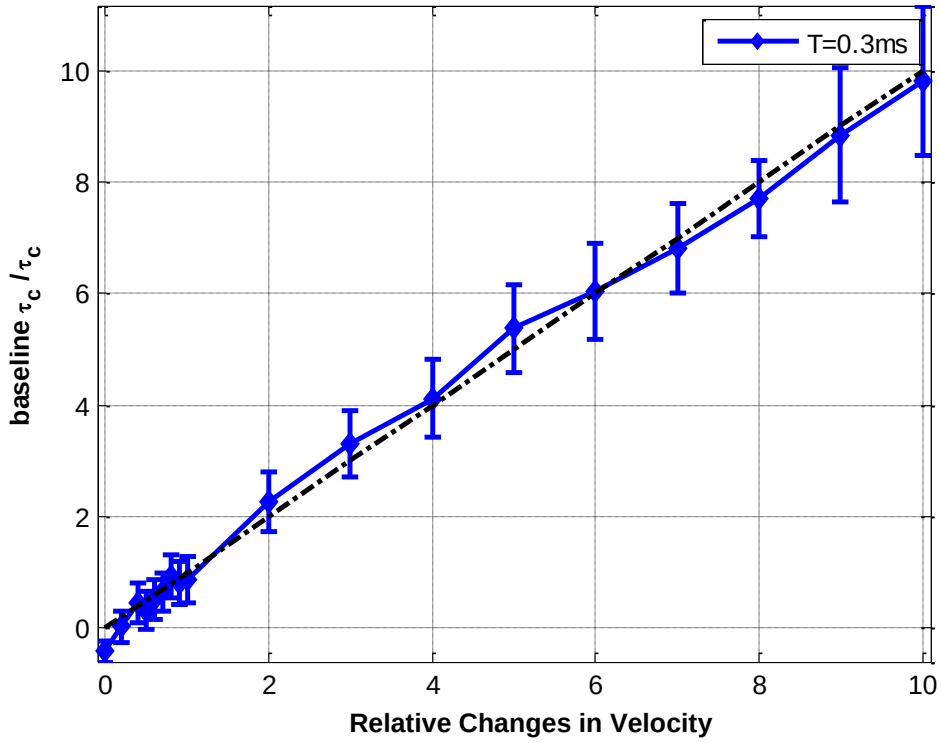

Figure 4. 2 Relative ICT flow estimates versus relative changes in velocity ranging from 0 to 10mm/s and exposure time of 0.3ms.

In Figure 4.3, results show the exposure time of 0.075ms also provides a linear relation between flow estimates of LSCI and microchannel flow velocities ranging from 0 to10mm/s with R^2 (coefficient of determination) of 96%.

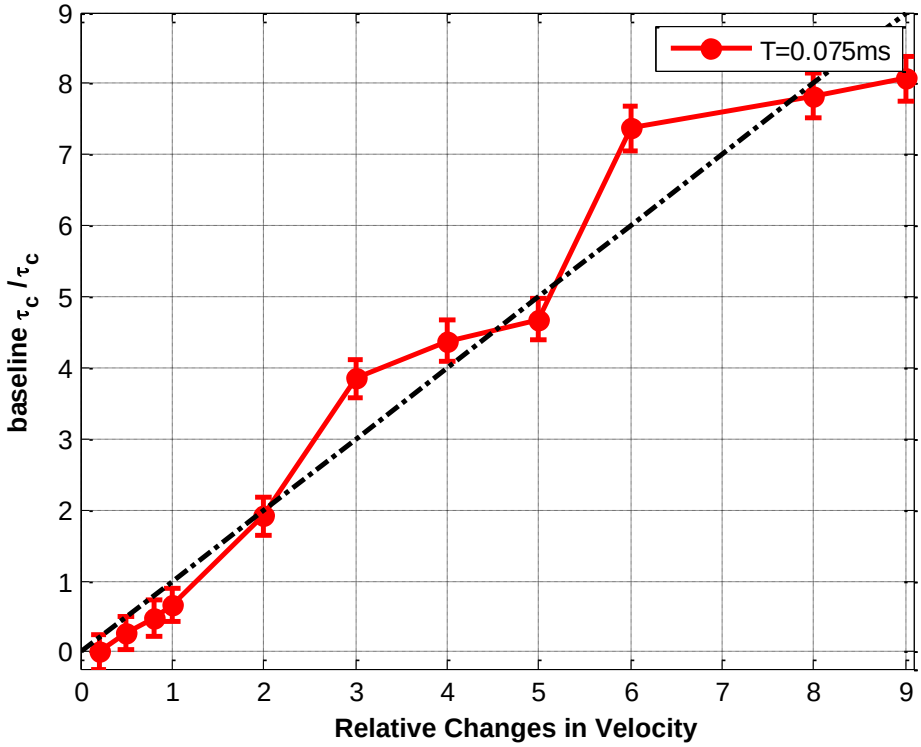

Figure 4. 3 Relative ICT flow estimates versus relative changes in velocity ranging from 0 to 10mm/s and exposure time of 0.075ms.

Both results show the shorter exposure time applications of LSCI do provide sufficient linearity between normalized ICT values and relative velocities. In Figure 4.4, both exposure settings are shown together on a semi-log scale along x axis. This result shows that both settings provide adequate linearity across two orders of magnitude in relative velocities. This result suggests that the acquisition rate of LSCI 200 Hz, the highest sample rate found in current literature, can be improved further to few thousand Hz and can be used to monitor the instantaneous changes of in vivo blood flow.

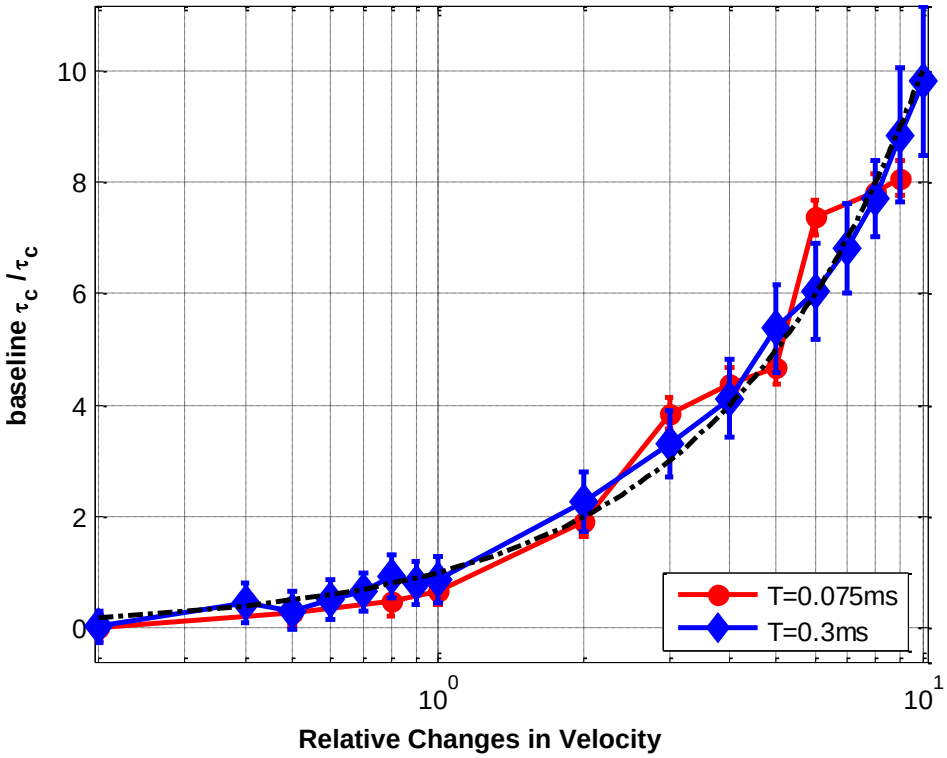

Figure 4. 4 Semi-log scale of relative ICT flow estimates versus relative changes in velocity ranging from 0 to 10mm/s and exposure time of 0.3ms and 0.075ms.

4.3 Early Experiments with Tadpoles

4.3.1. Animal Preparation

A one-month-old and a two-month-old tadpoles were used in the instrumentation verification process. The procedure of preparing tadpoles for LSCI imaging is as follows. First, we place a tadpole in a culture dish with enough water to cover the tadpole. Secondly, we add few drops of Tricane to anesthetize the tadpole.

4.3.2. Validation of Speckle Contrast Analysis

The spatial speckle contrast analysis computes the ratio of the standard deviation to the mean intensity of a local window, which was 7pixels x 7pixels, captured under 634nm coherent light illumination as shown in Figure 4.5 (a). The result of spatial contrast analysis is shown in Figure 4.5 (b). The area with higher blood flow has lower

speckle contrast value and appears darker in the speckle contrast map, e.g., the region of larger vessels. Theoretically, speckle contrast values laid between 0 and 1. A spatial contrast of 1 indicates that within the analyzed window there is no moving speckle to produce the blurring effect on the image, while a spatial contrast of 0 indicates the fast moving scatterers blurring pixels completely and creating a uniform intensity over the analyzed window.

Exposure time was optimized for imaging the vasculature of tadpole. A 250ms relatively long exposure time was chosen. Since the concentration of the red blood cell in the tadpole was relatively low compared to cerebral cortex, it requires longer exposure time to obtain detectable blurring effect.

Within the speckle contrast map, the tadpole's vascular structure and its stomach are clearly visible.

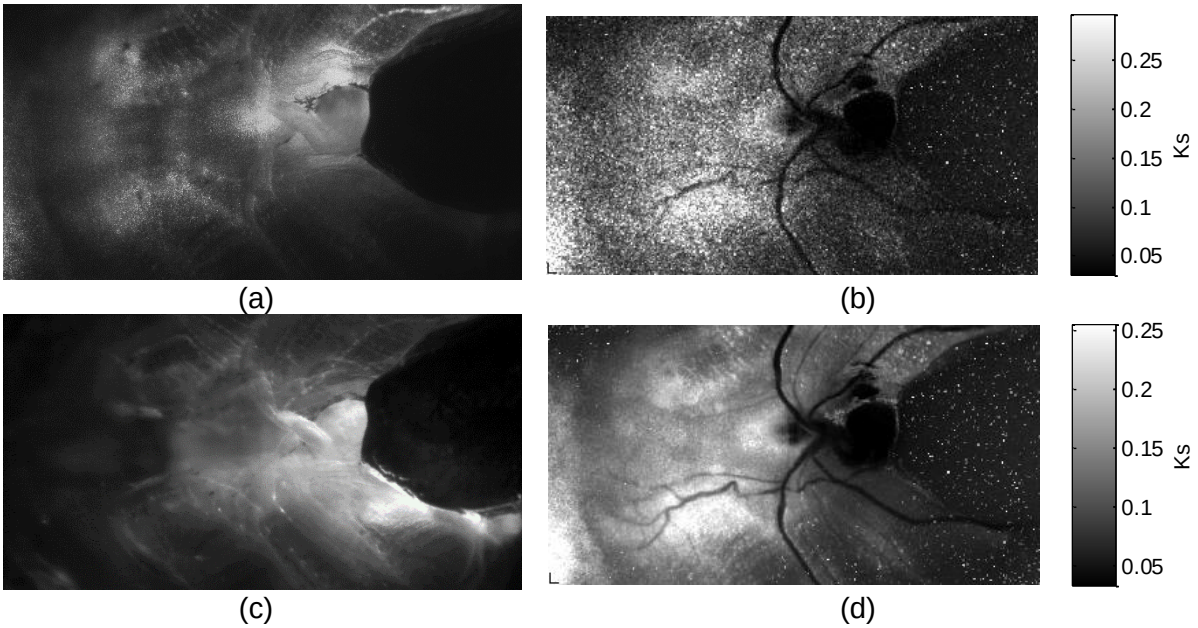

Figure 4. 5 (a) The raw speckle image of tadpole's heart and arteries while the tadpole is illuminated and imaged from the bottom. The speckle contrast image (b) is computed directly from the image (a) through the contrast equation representing the 2D blood flow. The scale bars in images are 100 microns. Image (c) is the bright field image. Image (d) is the averaged contrast map using 200 spatial speckle contrast maps that is similar to (b).

With a frame rate of 100fps, the ventricular activity of the tadpole's vascular system is observed in a two-month-old tadpole. In the following 25-image montage, a duration of 1.9 seconds was captured. One vessel is highlighted by a red arrow. This vessel appears in the first few images of the montage and then disappears due to the pulsation. The tadpole heart rate is around 1Hz, and the montage shows two pulsatile peaks in its pulsation, since the highlighted vessel appears again in the frame number 104.

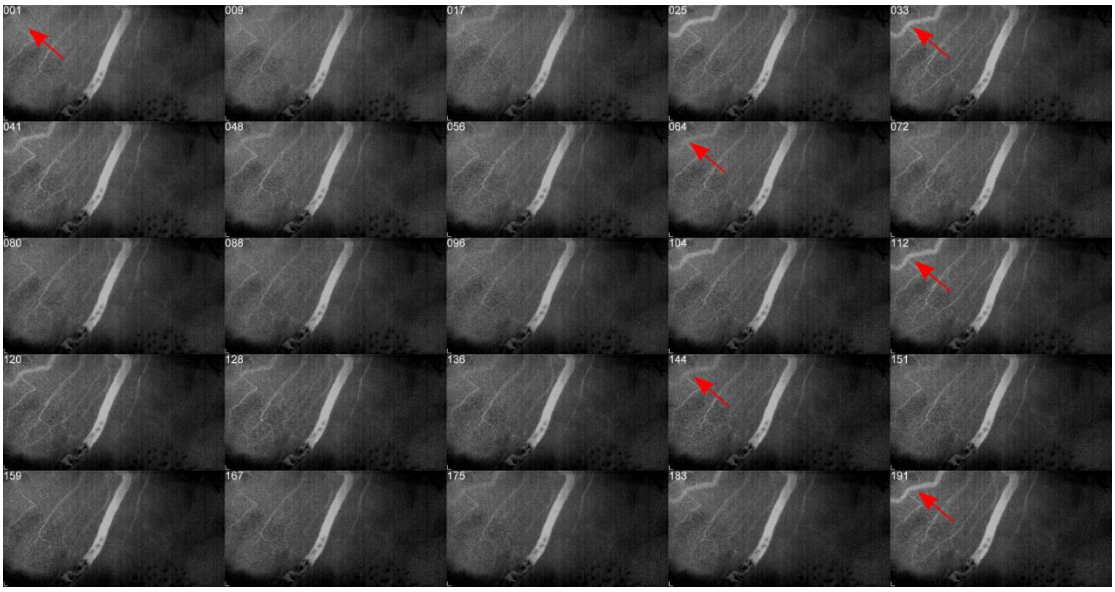

Figure 4. 6 A montage view of the speckle contrast video showed in 1/K_s The 25 images are selected from 191 spatial contrast images and the moving-averages filter is applied with a window size of 10 frames, the raw data is captured under 10ms exposure time. The contrast images are shown in the intensity of the inverted contrast value 1/Ks for better perception. Bright vessel are indicating higher flow rate.

To quantify this observation, Figure 4.7 (b) shows the spatial-averaged time trace of the selected area in Figure 4.7 (a). It clearly shows two waves within one cardio cycle, which matches the previous observation in Figure 4.6. It also shows that the dynamic characteristics of the flow rate such as the fall time and rise time. It also shows the preliminary wave before systole flow wave where it is not distinguishable in the montage.

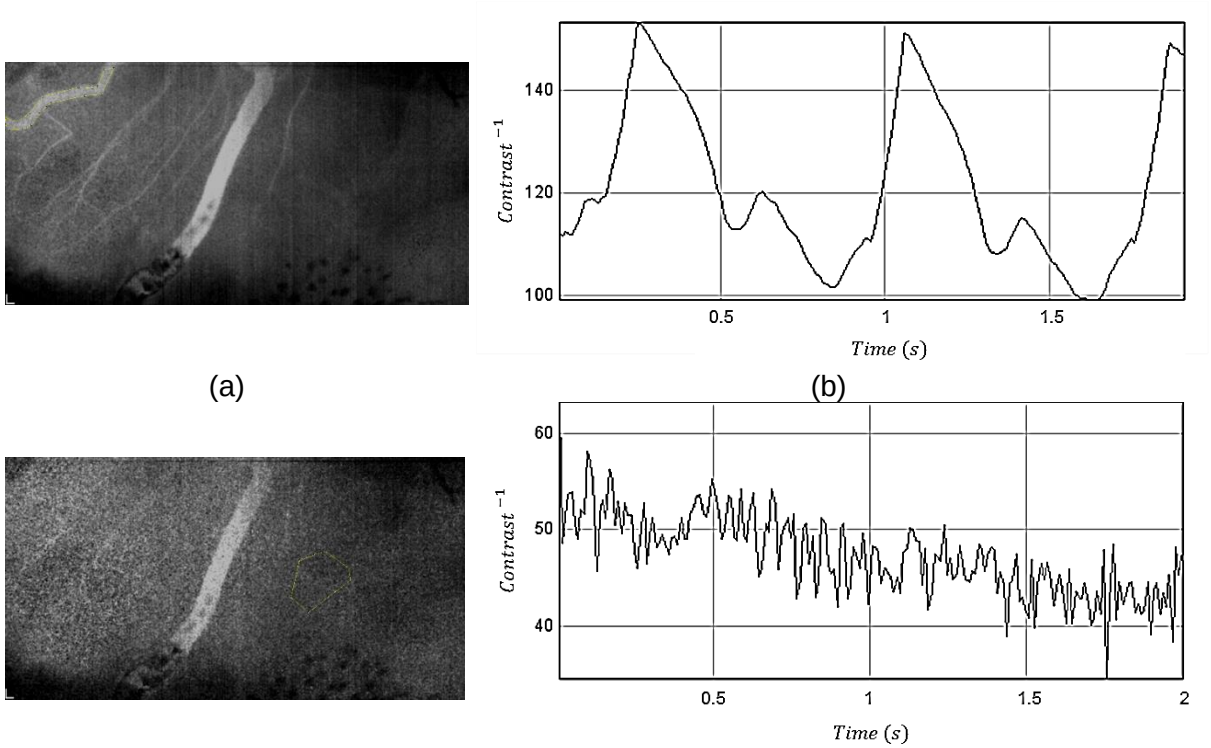

Figure 4. 7 (a) Capturing the raw data with exposure time 10ms at 99fps, and processing with spatial contrast analysis with 10 frames moving-averages filter, (b) the time series profile from a selected area of the image (a), (c) capturing the raw data with exposure time 50ms at 99fps, and processing with spatial contrast analysis without applying the moving-average filter, (d) the time series profile of a selected area of the image(c).

4.3.3. Effect of Exposure Time

In Figure 4.8, a two-week old tadpole's heart and arteries are shown. In this stage of development, the animal has a fish-like circulatory path and only has one ventricle. When the blood is pushed out of the ventricle, it entered the truncus arteriosis which has a sinus which helps the flow to be divided into left aortic arches and right aortic arches.

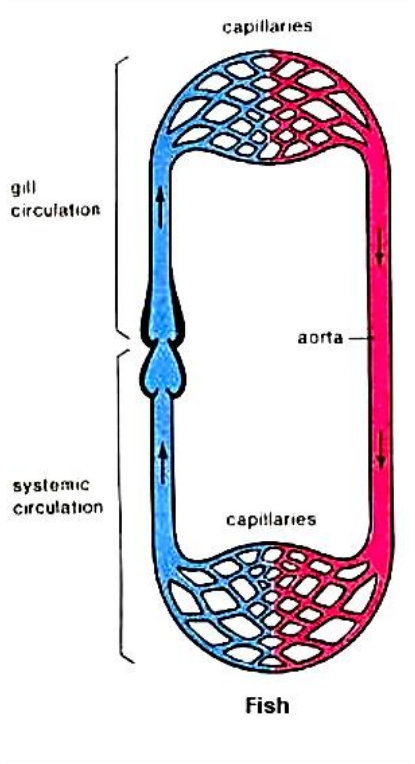

(a)

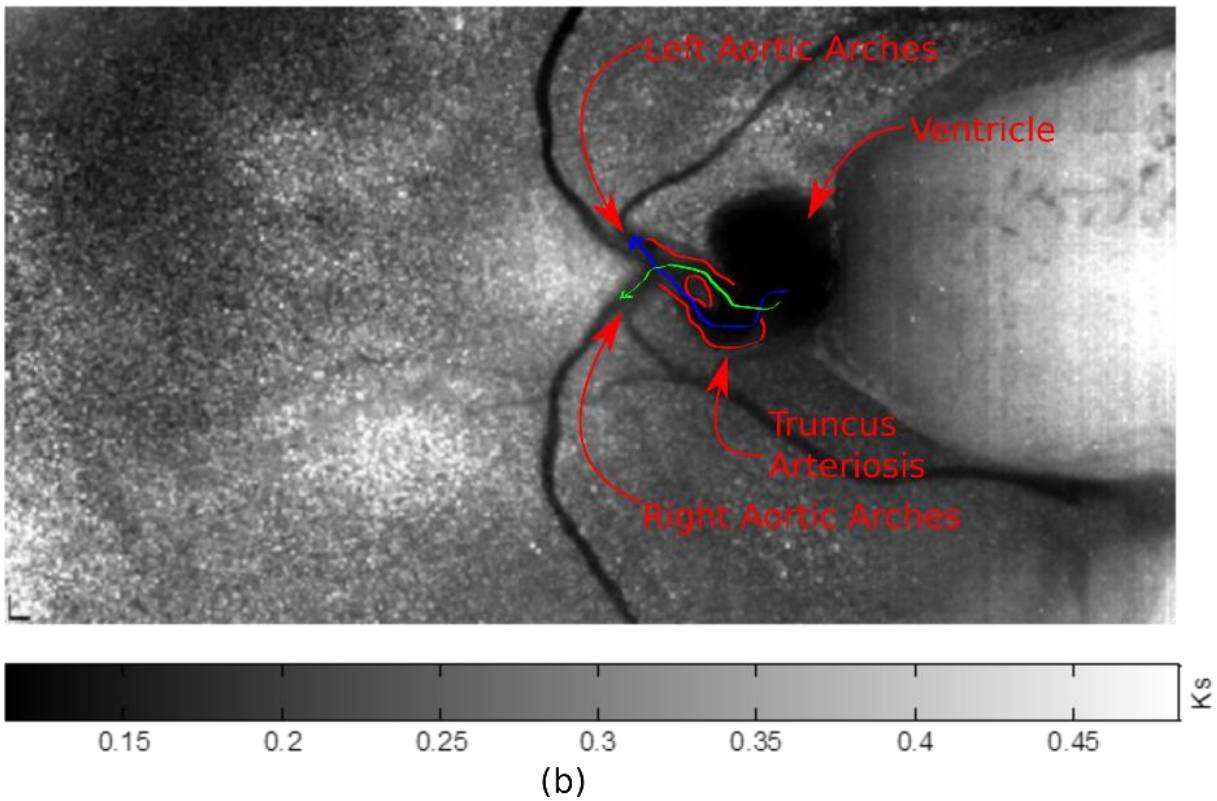

(b)

Figure 4. 8 (a) Circulatory of a fish (b) The heart anatomy of the two-week old tadpole.

To compare the effect of exposure time, the data of exposure time settings ranging from 1ms to 250ms are collected and processed. The result is shown in Table 4.1. In all the exposure time settings, the major arteries are visible. The red circle highlights the area in T=5ms image of table 4.1 which clearly shows a sinus inside the truncus arteriosis. As the exposure time increases, the sensitivity of slower motion increases and the small vessels appears. However, for the high velocity region, the specificity drops, and the sinus inside the truncus arteriosis disappears in the 250 ms image. This result proves the hypothesis mentioned in section 2.5.

Table 4. 1
Images collected under different exposure times and processed by the spatial contrast with 7x7 analysis window size.

1ms	2.5ms	5ms
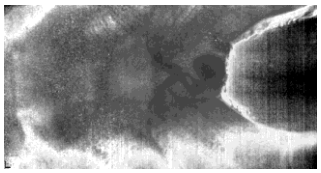	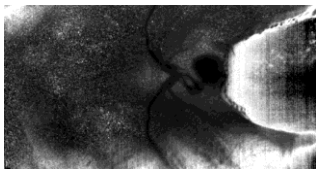	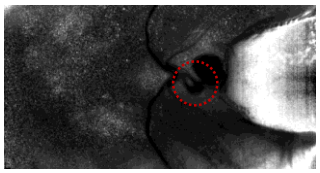
10ms	25ms	50ms
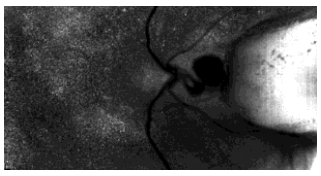	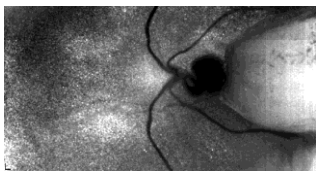	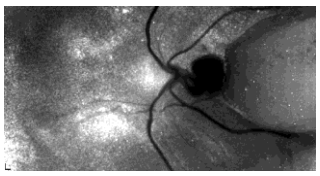
100ms		250ms
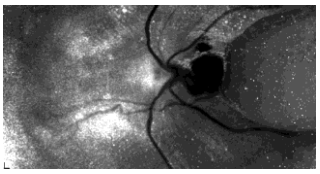		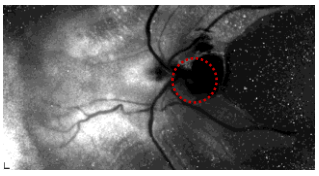

4.3.4. Verification of Optimized Spatial Contrast Analysis Window Size

The effect of the spatial contrast analysis window size was reviewed in chapter 2. Duncan et al. [31] stated that the insufficient spatial sample results in the underestimation of the speckle contrast. In this section, the discussion is carried out

by analyzing the same dataset with different window sizes starting from $N_{pixels}^{1/2} = 3$ to $N_{pixels}^{1/2} = 13$. The results are illustrated in Table 4.2 are the collections of the spatial contrast processed images without temporal averaging. In the indicated area for the $N_{pixels}^{1/2} = 3$ image, one can find that the sharpness between the ventricle and background is reduced due to the underestimation of contrast caused by the insufficient spatial sample. As the window size increases, the contrast estimation error reduces. In the indicated area for the $N_{pixels}^{1/2} = 7$ image, the background and the ventricle are clearly divided. Table 4.3 shows a collection of contrast images produced by averaging 200 frames along time. It also shows the sharpness of the image increases as $N_{pixels}^{1/2}$ increases, and the sharpness of image settles at $N_{pixels}^{1/2} = 7$. considering the tradeoff between the of accuracy of statistical estimation and spatial resolution, $N_{pixels}^{1/2} = 7$ shows a reasonable compromise, which makes it the current settled point in academia as the number of pixels used in most spatial contrast analysis algorithms.

Table 4. 2
Single frame analyzed by spatial contrast.

$N_{pixels}^{1/2} = 3$	$N_{pixels}^{1/2} = 5$
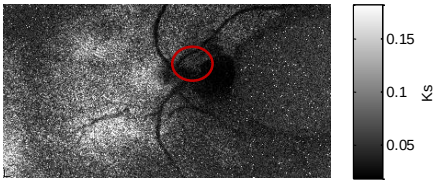	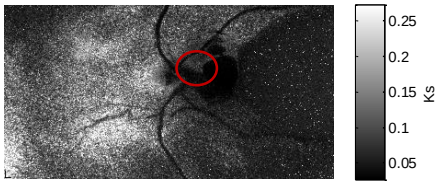
$N_{pixels}^{1/2} = 7$	$N_{pixels}^{1/2} = 9$
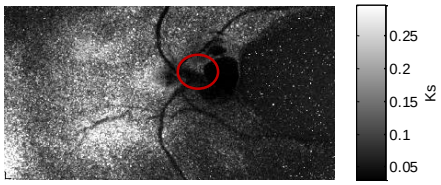	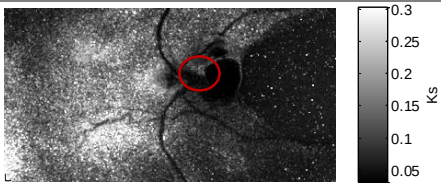
$N_{pixels}^{1/2} = 11$	$N_{pixels}^{1/2} = 13$
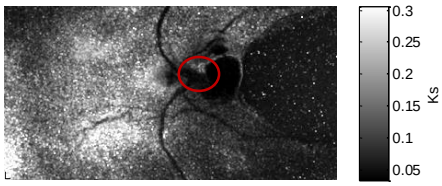	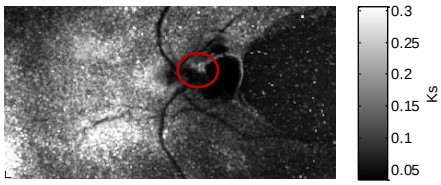

Table 4. 3
Averaging 200 frames of spatial contrast analysis results.

$N_{pixels}^{1/2} = 3$	$N_{pixels}^{1/2} = 5$
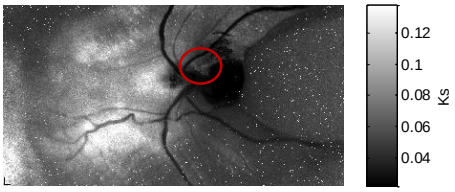	
$N_{pixels}^{1/2} = 7$	$N_{pixels}^{1/2} = 9$
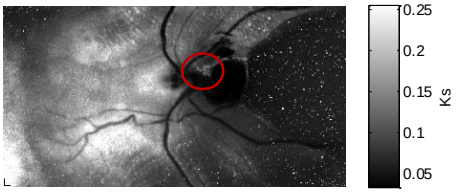	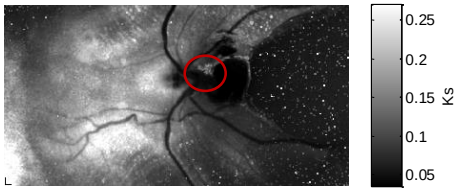
$N_{pixels}^{1/2} = 11$	$N_{pixels}^{1/2} = 13$
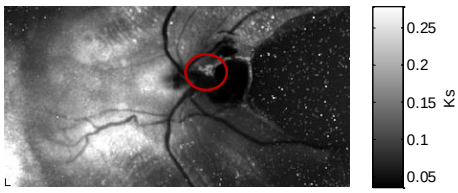	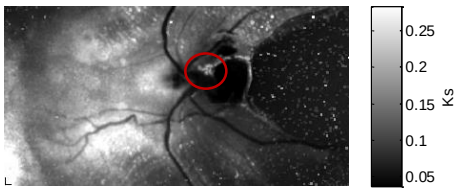

4.4 Experiments with Rats

4.4.1. Animal Preparation

Two Sprague-Dawley rats are used for the experiments. Both animals were around 12-week-old. The animals were anesthetized through inhaling isoflurane and immobilized by a stereotaxic instrument. A craniotomy with 2.5mm diameter was created in the region that is 1mm away from Bregma toward the direction of its tail and 2 mm away from the sagittal suture as shown in Figure 4.10.

Figure 4. 9 An anesthetized rat immobilized by stereotaxic instrument.

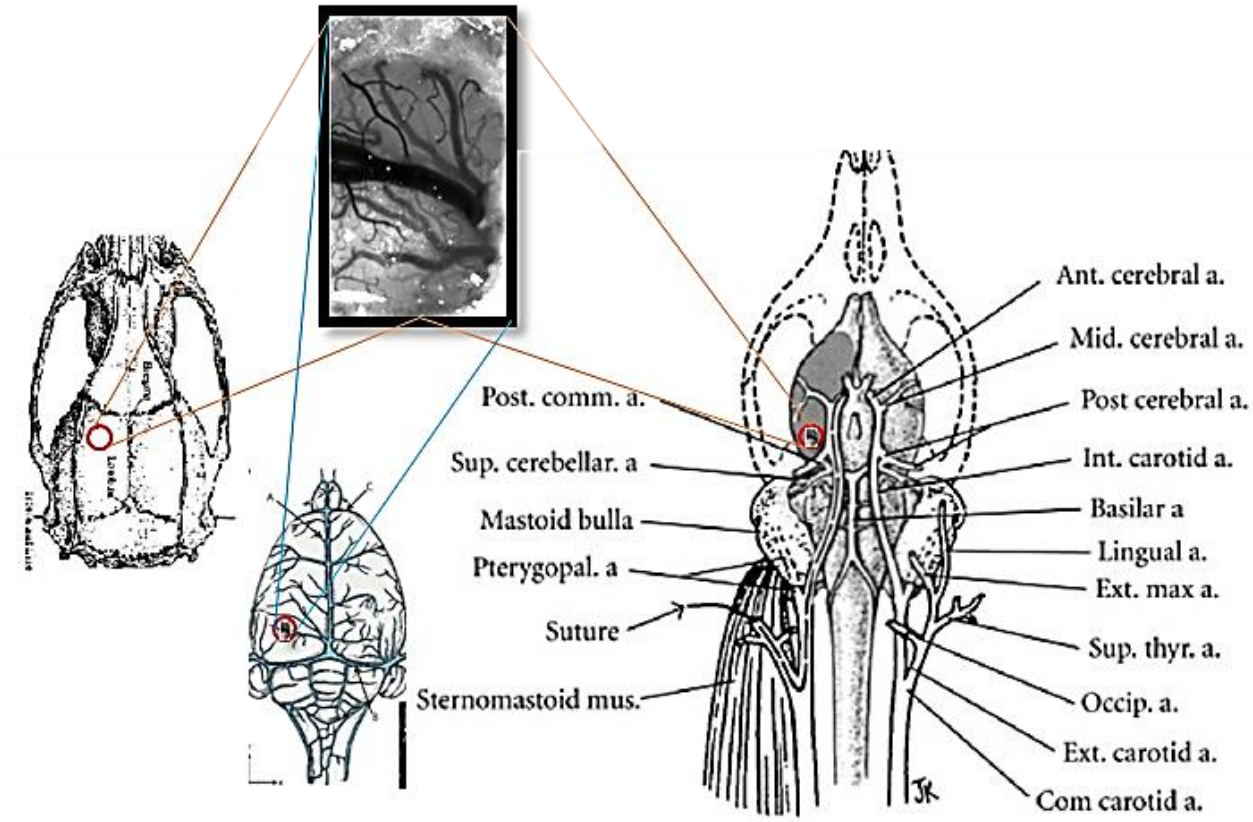

Figure 4. 10 Position of cranial window

After removing the dura, a glass coverslip was placed on the cortex, then dental cement was applied to seal the glass coverslip. The resulting transparent area (diameter 2mm) is shown in Figure 4.11. During the experiment, a constant flow of saline was keeping the skull moist.

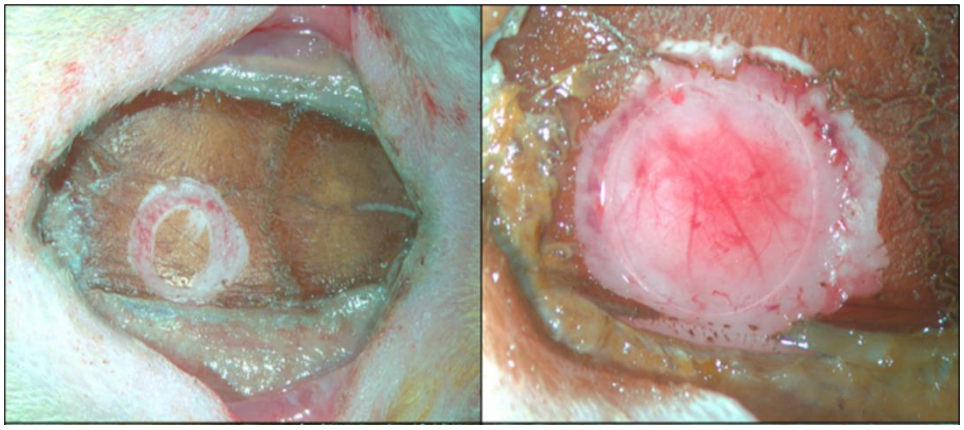

Figure 4. 11 Bright-field image of cranial window

4.4.2. Validation of the Polarized Detection

As discussed in section 2.6, the polarized light detection only allows the photons that experience multiple-scattering to be detected by the camera detector. So it is beneficial to reduces the specular reflection coming off the surfaces of the coverslip and the cortex.

To calibrate the polarized light detection, the polarization of detected light was changing from 0 to 90 degree with respect to the polarization of laser.

In Figure 4.12, the result of 0 degrees from the polarization of laser contains highly disturbed speckle noise. The noise reduced as the angle increased. The result of 90 degrees has most of the speckle noise removed. The highlighted diagonal regions make this noise reduction apparent. Besides, in all images, the salt and paper (the red highlighted circle) noise caused by saturation of pixels remains.

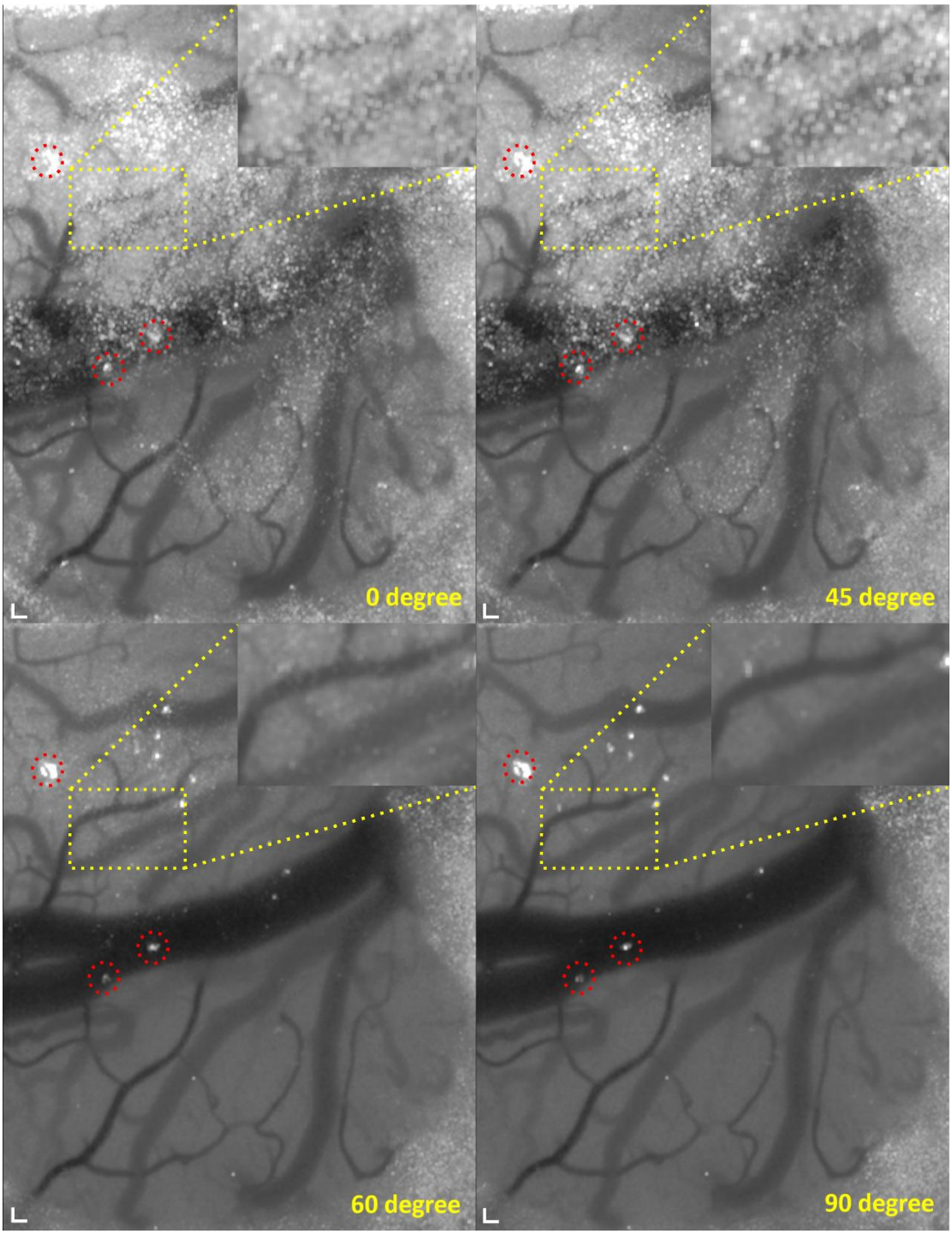

Figure 4. 12 Effect of polarized light detection from 0 to 90 degrees angle with respect to the angle over which the maximum intensity is detected. The scale bars are 100 µm.

4.4.3. 2D and 3D Mean Contrast Maps

By averaging the contrast 2D map over 12000 contrast maps acquired with 5ms exposure time, a high definition mean velocity profile, shown in figure 4.13 (a), is

produced. The ImageJ [65] interactive 3D function is used to produce the 3D surface plot in figure 4.13 (b).

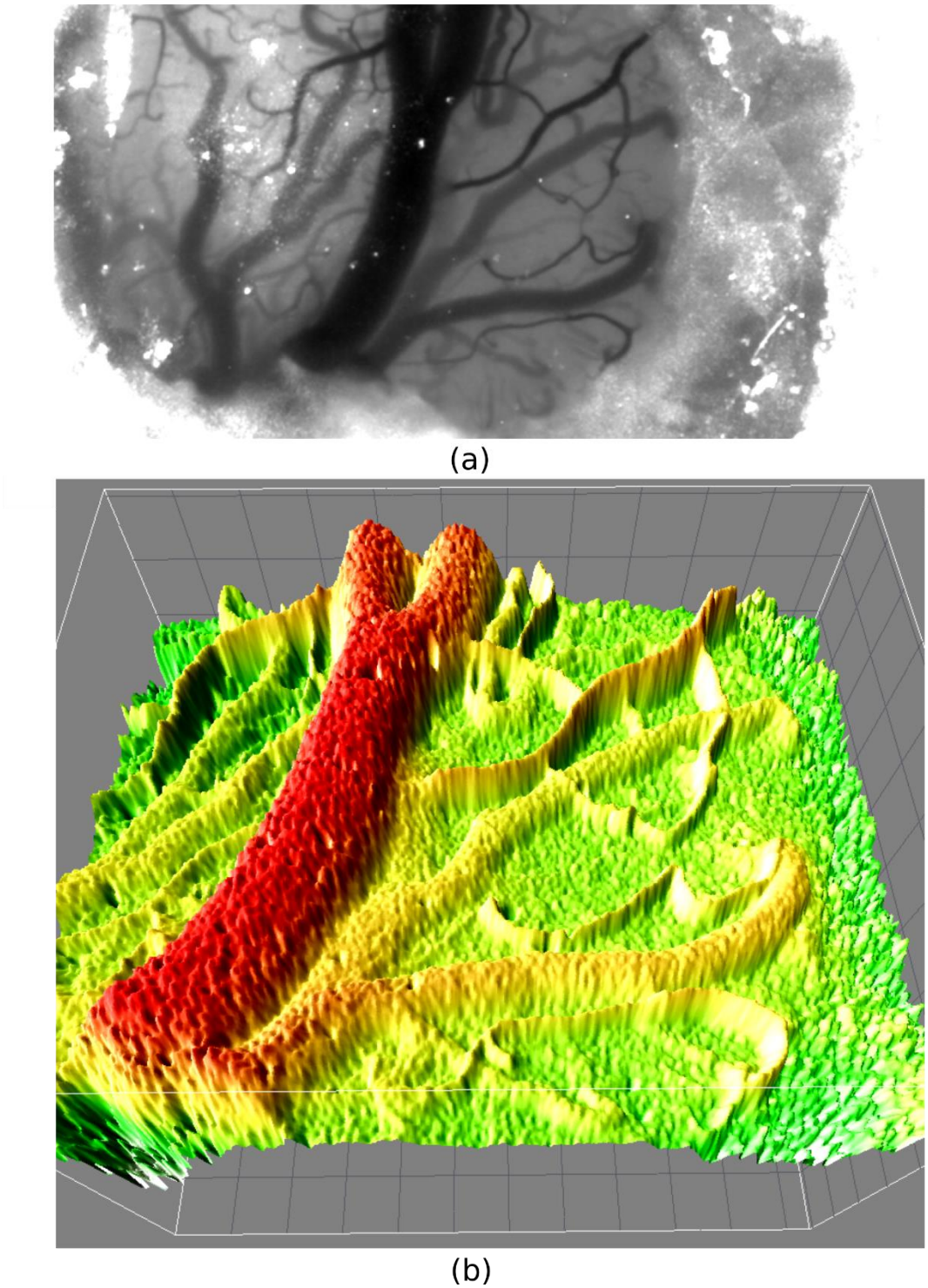

Figure 4. 13 (a) Mean speckle contrast profile, (b) 3D surface plot with 1/Ks as the z axis.

4.4.4. Labeling Vessels Based On Being an Artery or a Vein

In Figure 4.14 (a) and (b), veins and arteries cerebral anatomies are shown respectively, and the LSCI field of view is placed at an approximated position in both images. Based on these anatomies and the position of our field of view, one can predict the direction of vessels. For veins, blood is collected along the venule and eventually moves toward central sulcus. For arteries, the vessels are coming off the Middle Cerebral Artery (MCA), and branch as much as possible to deliver nutrients to the tissue. The ratio of vessel diameter to flow rate is typically high in arteries compared to veins. Based on these three facts, the prediction of vascular types are drawn in the field of view as shown in Figure 4.14 (d) for arteries and (e) for veins. In the rest of this chapter, individual vessels will be investigated. A labeled image in which arteries and veins are separated is depicted in Figure 4.14 (c).

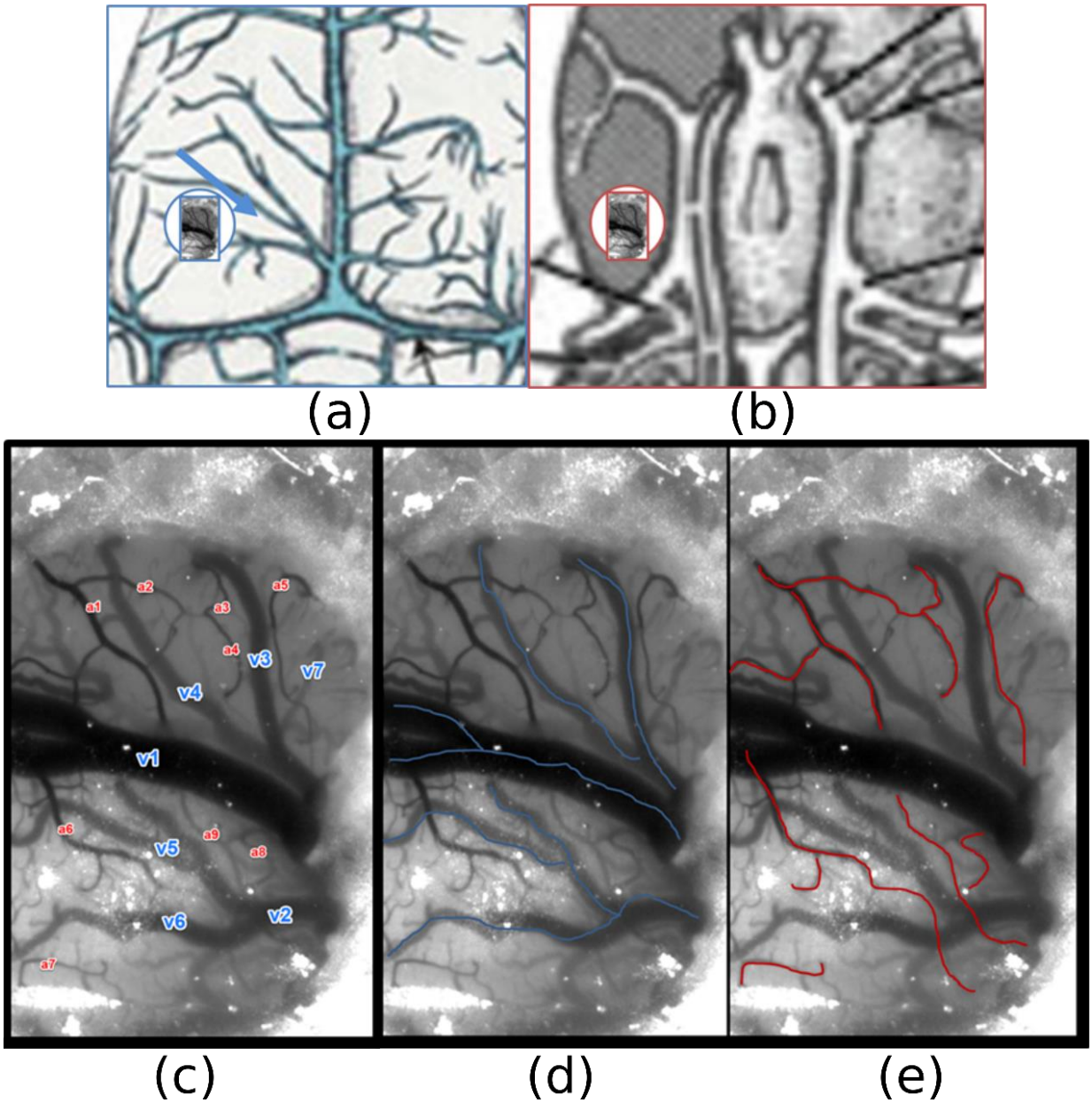

Figure 4. 14 (a) Cerebral anatomy of veins (b) Cerebral anatomy of arteries (c) Labeling of vessels. (d) and (e) show distinguished veins (blue) and arteries (red) through empirical knowledge in the field of view of rat cerebral cortex.

4.4.5. Validation of Correlation Model in Vivo

To validate the correlation model, a selected vessel data and its spatial averaged contrast value were obtained under various exposure times ranging from 0.25ms to 5ms. In total, 15 data points were collected over a period of 27 mins. A set of β=0.02, instrumentational factor, and τ_c=0.185ms, correlation time, was found to

give a minimum error between the model predictions and experimental results. These settings produce Mean-Square-Error (MSE) of 1.5235e-06.

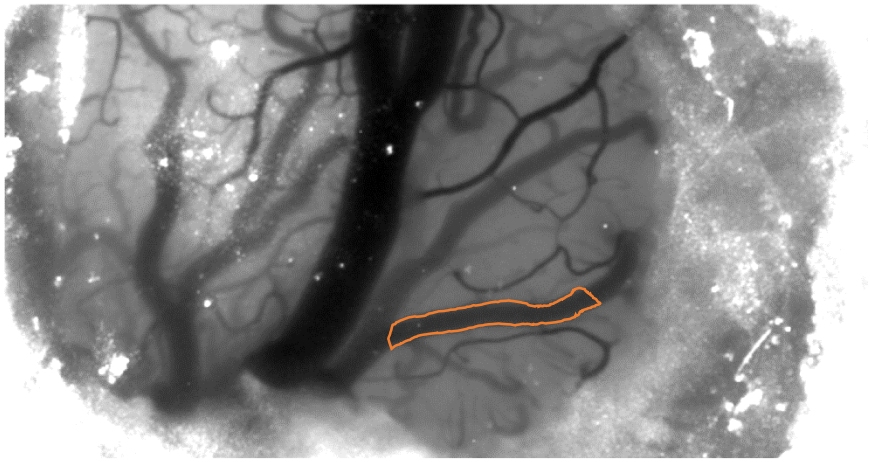

Figure 4. 15 Indicating the position of the selected vessel in the field of view.

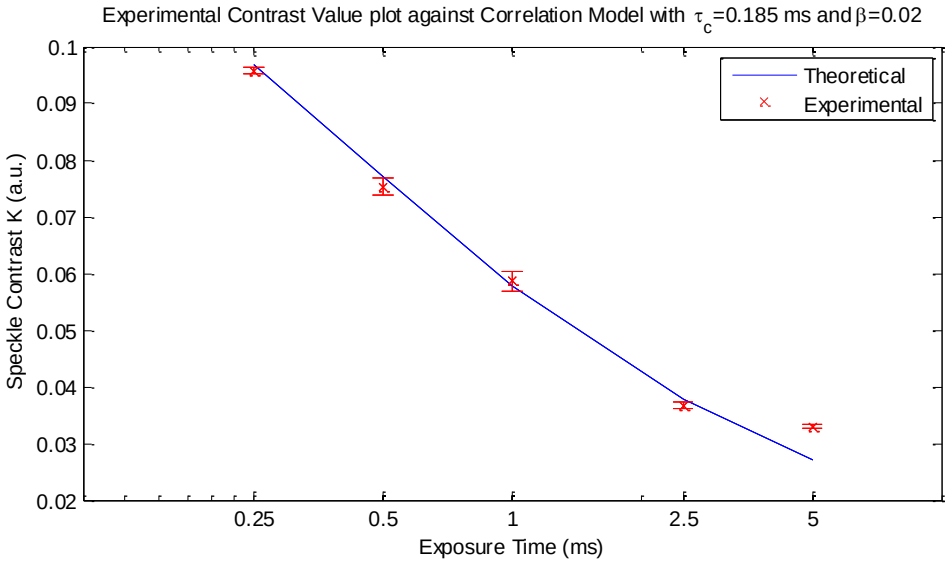

Figure 4. 16 Speckle contrast values obtained at the selected vessel under different exposure times.

4.4.6. Validation of Cross-Section Ensemble Average Algorithm

The first part of the ensemble average algorithm is skeletonization. Figure 4.16 shows the process of preprocessing and the result of skeletonization. The results show the algorithm is successful in producing the skeleton of small and medium-size vessels.

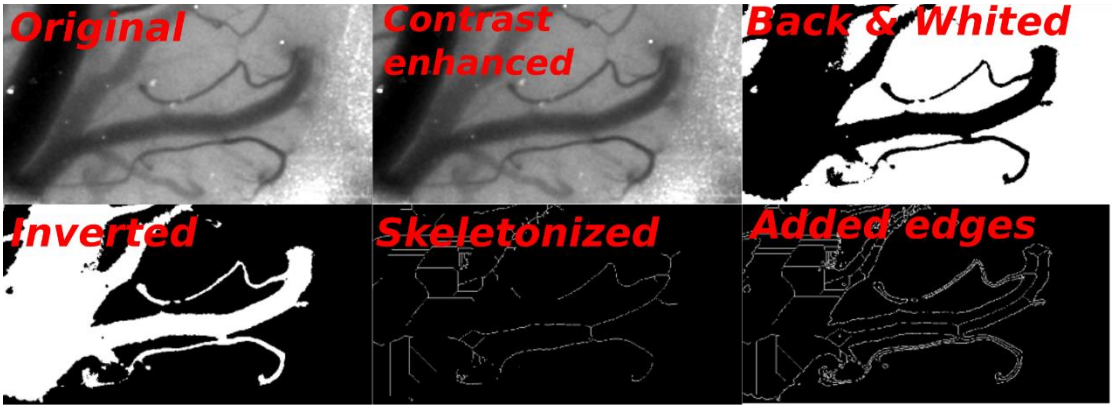

Figure 4. 17 The procedures of preprocessing and the result of skeletonization.

The second part of the ensemble average algorithm is the automated slicing algorithm. Figure 4.18 shows the ensemble average velocity profile of multiple slices.

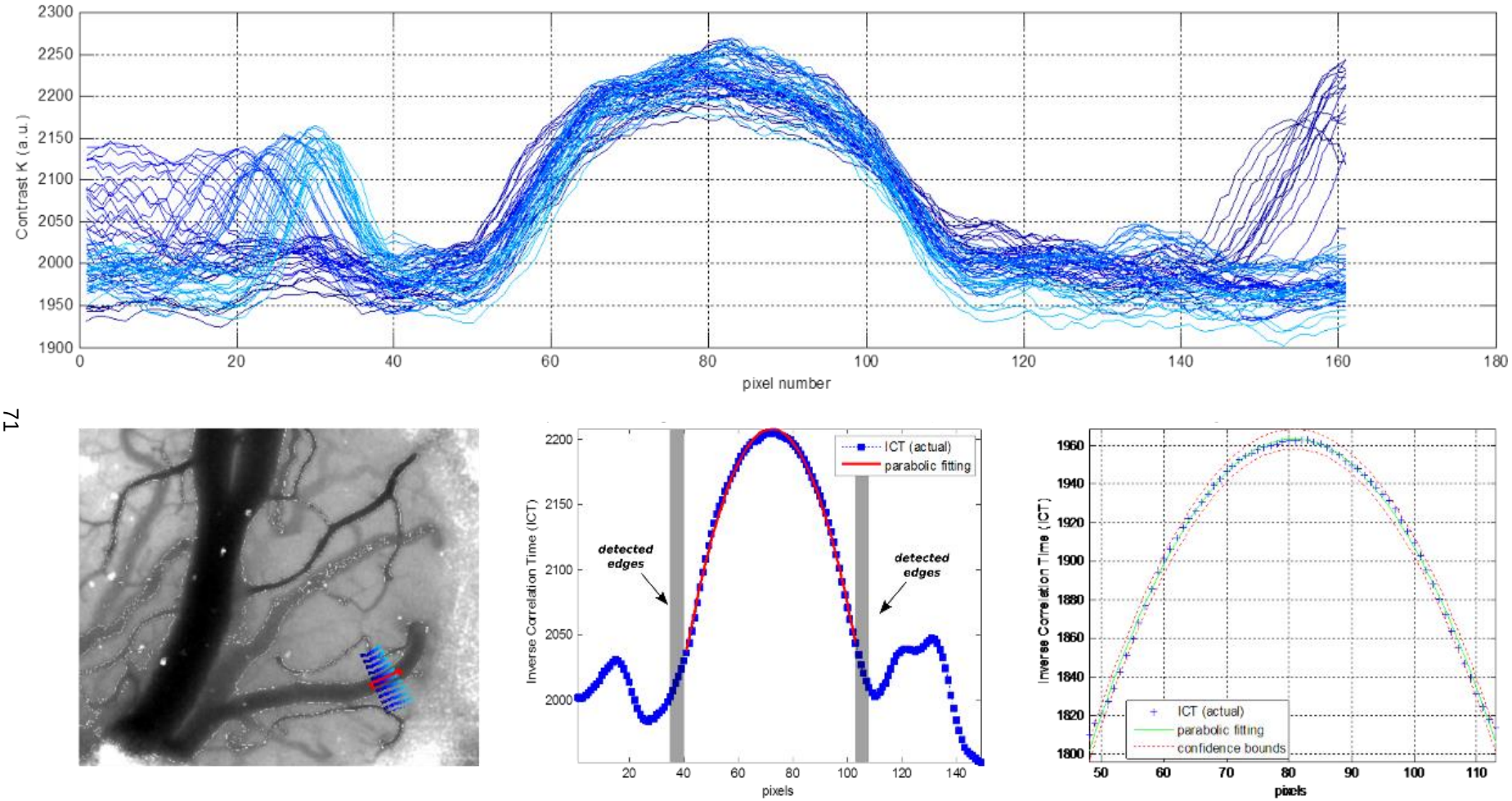

Figure 4. 18 The top panel is the velocity profile of multiple cross-sections. The lower left panel shows the slicing area of velocity profiles corresponding to the top panel. The lower middle panel shows the ensemble average of multiple cross-sections shown in top panel. The lower right panel shows the ensemble average of velocity profile with the corresponding parabolic fitted curve and the 5% confidence bounds.

4.4.7. Validation of LSCI Flow Index in Vivo

To validate the flow estimate of LSCI in vivo, a cross section of velocity profile were investigated. Ideally, if a vessel is smooth and has a minimum turning angle and roughness, that vessel develops a laminar pipe flow with parabolic velocity profile. In this analysis, ***v3*** vein was chosen.

In Figure 4.19, the results are shown for exposure time settings ranging from 0.25-5ms which have good correlations with the corresponding parabolic fitted curves. The coefficient of determination R^2 is above 99% for all exposure settings. These results support that the relative ICT estimate provides sufficient linearity to resolve relative blood flow differences.

These results also support that the short exposure time speckle imaging is as reliable as the commonly suggested exposure time (5ms) in terms of the linearity of the ICT index.

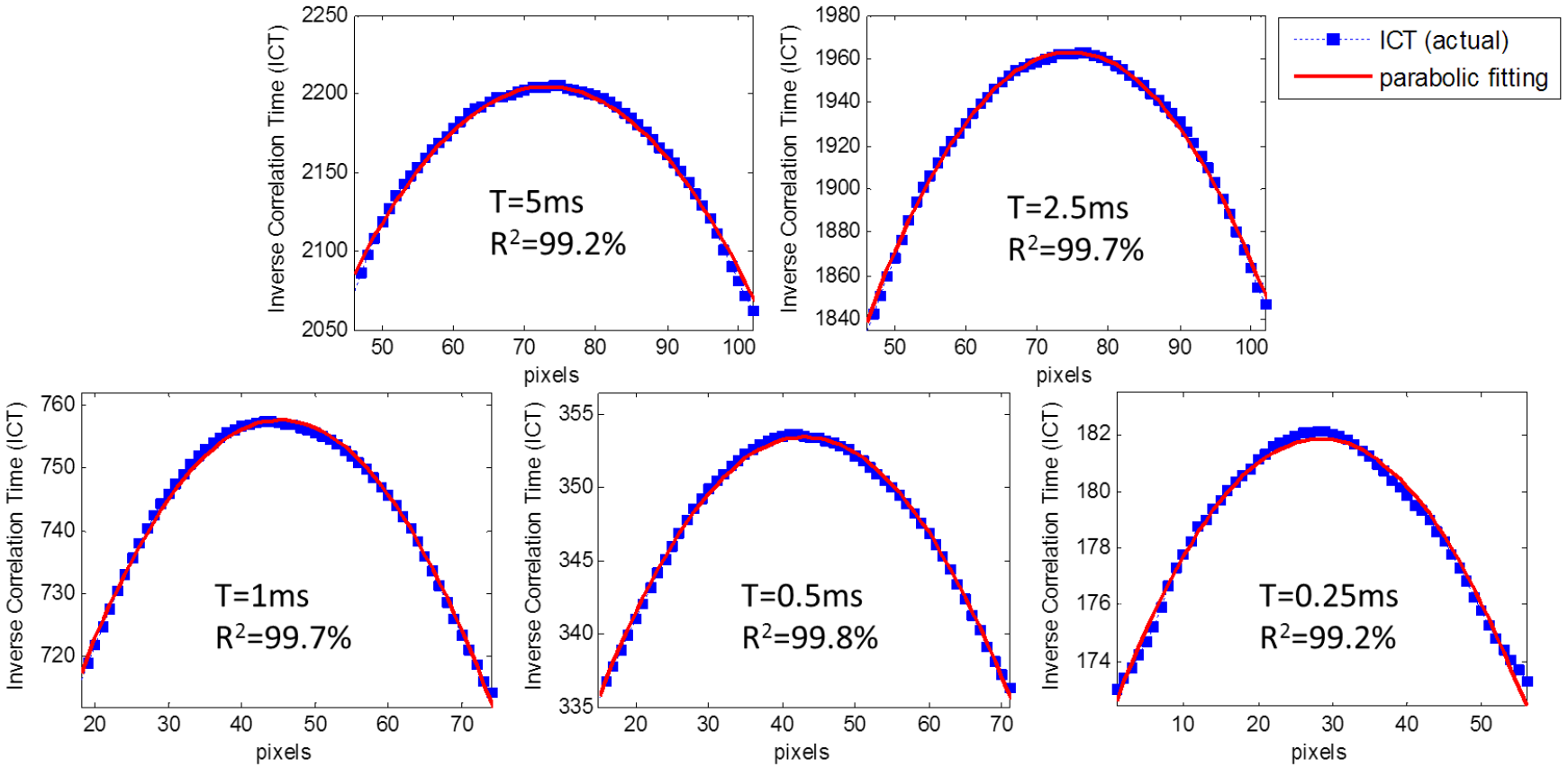

*Figure 4. 19 The velocity profile of the **v3** vein cross-section captured with different exposure times. The vein (**v3**) has a diameter of 64 μm.*

4.4.8. Experimental Results of Functional Brain Activation

Phenylephrine Tail Injection

Uncontrolled high blood pressure increases a person's stroke risk four to six times. Over time, hypertension leads to atherosclerosis and hardening of the large arteries. This, in turn, can lead to blockage of small blood vessels in the brain and results in an ischemic stroke. In this section, the LSCI system is used during a Phenylephrine tail injection event to observe the cerebral hemodynamic response. When Phenylephrine is injected into the tail of the rat, its blood pressure increases rapidly and creates a hypertension event. Since the blood flow variation in the Phenylephrine tail injection is relatively high, it is clearly visible in the montage of the inverse contrast level 3D surface plot.

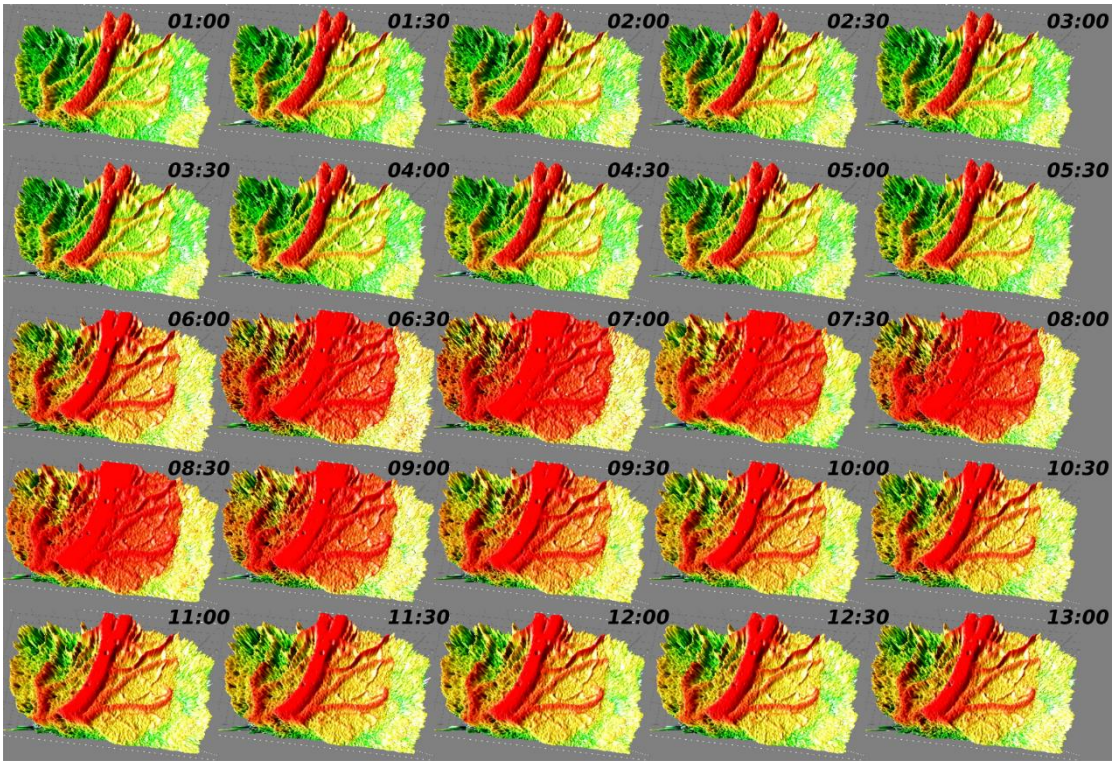

Figure 4. 20 A montage of Phenylephrine activated hemodynamic event.

The Phenylephrine is injected in the tail around 5:00 (minutes: seconds) after the beginning of the imaging section. The sudden increase of the blood is seen around

the sixth minute after imaging began, and the effect of Phenylephrine lasted for 10 minutes. The blood flow is slowly coming back to normal at the fourteenth minute. For three vessels, ***a6*** artery ***v3*** vein and ***v6*** vein, relative blood flow time traces over Phenylephrine activated hemodynamic event are plotted in the Figure 4.21.

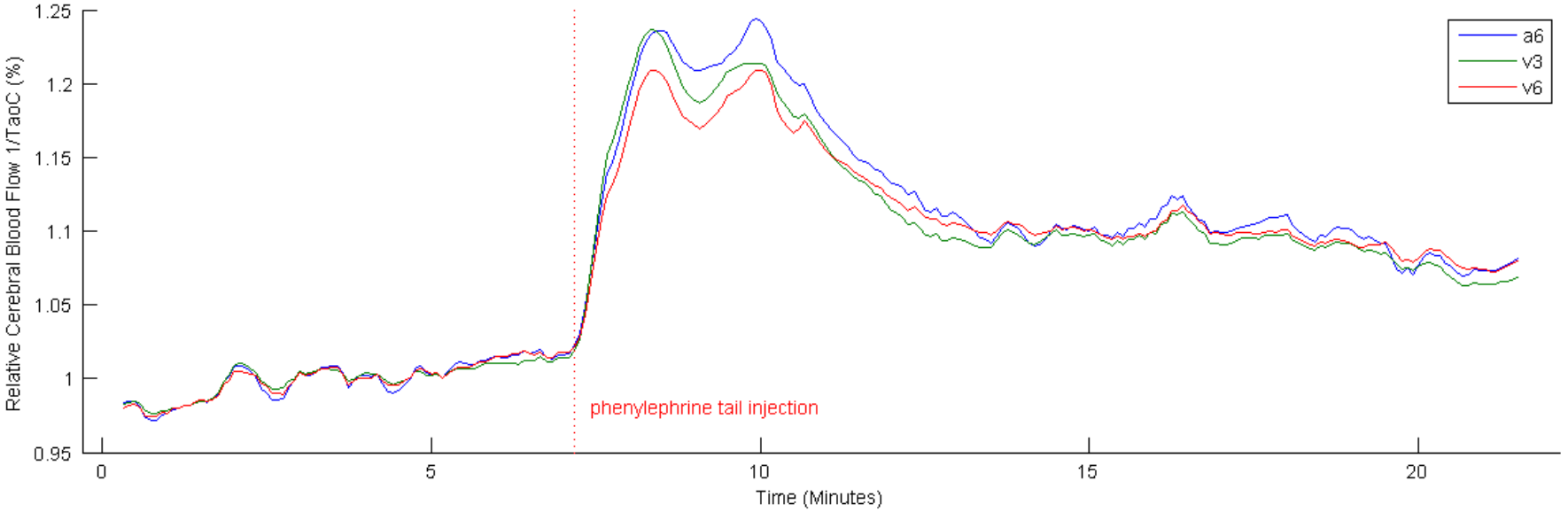

*Figure 4. 21 Relative blood flow time traces of the **a6** artery, **v3** and **v6** veins over Phenylephrine activated hemodynamic event*

12% Hypoxia

In this section, the LSCI system is used during a hypoxia event to observe the cerebral hemodynamic response. A time traces of the hemodynamic response of a vein that is encircled in Figure 4.22 is plotted in the top panel of Figure 4.23. The pulse wave velocity (PWV) derived from aortic blood pressure is plotted in the bottom panel of Figure 4.23. Increases in PWV are typically related to the increased arterial resistance. This result matches LSCI ICT flow estimate.

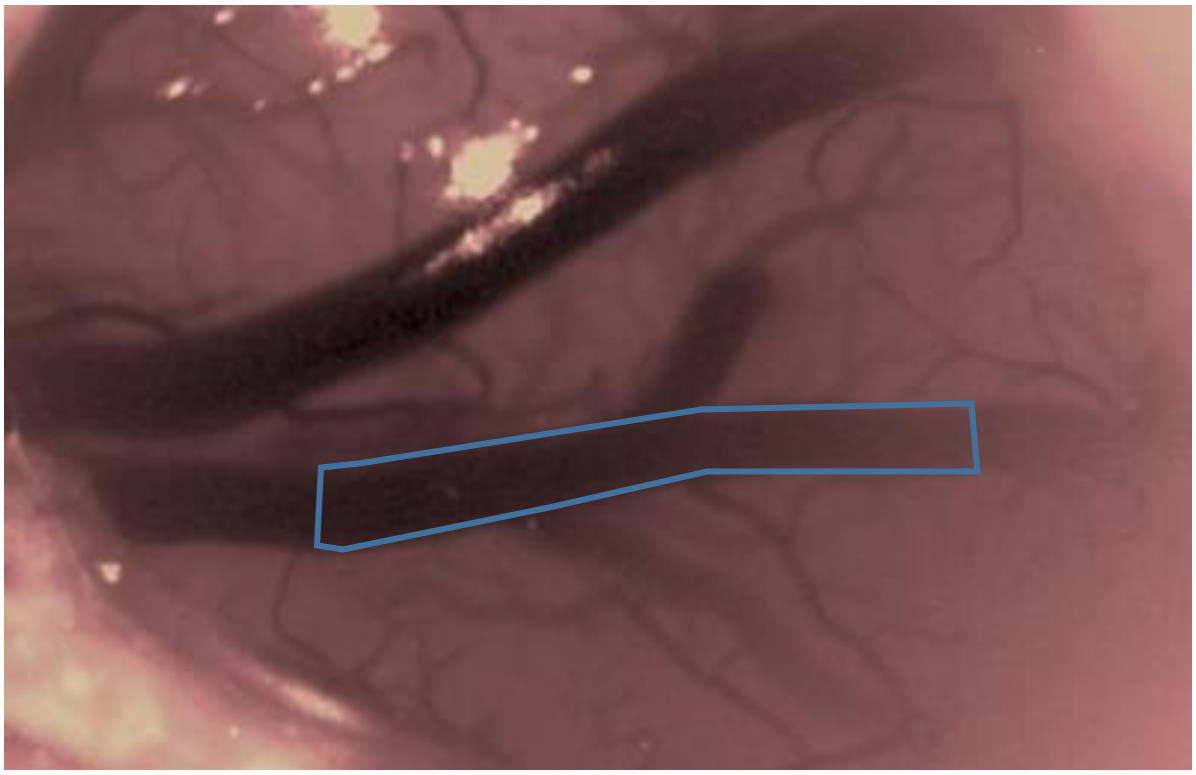

Figure 4. 22 The highlighted vessel in the LSCI contrast map.

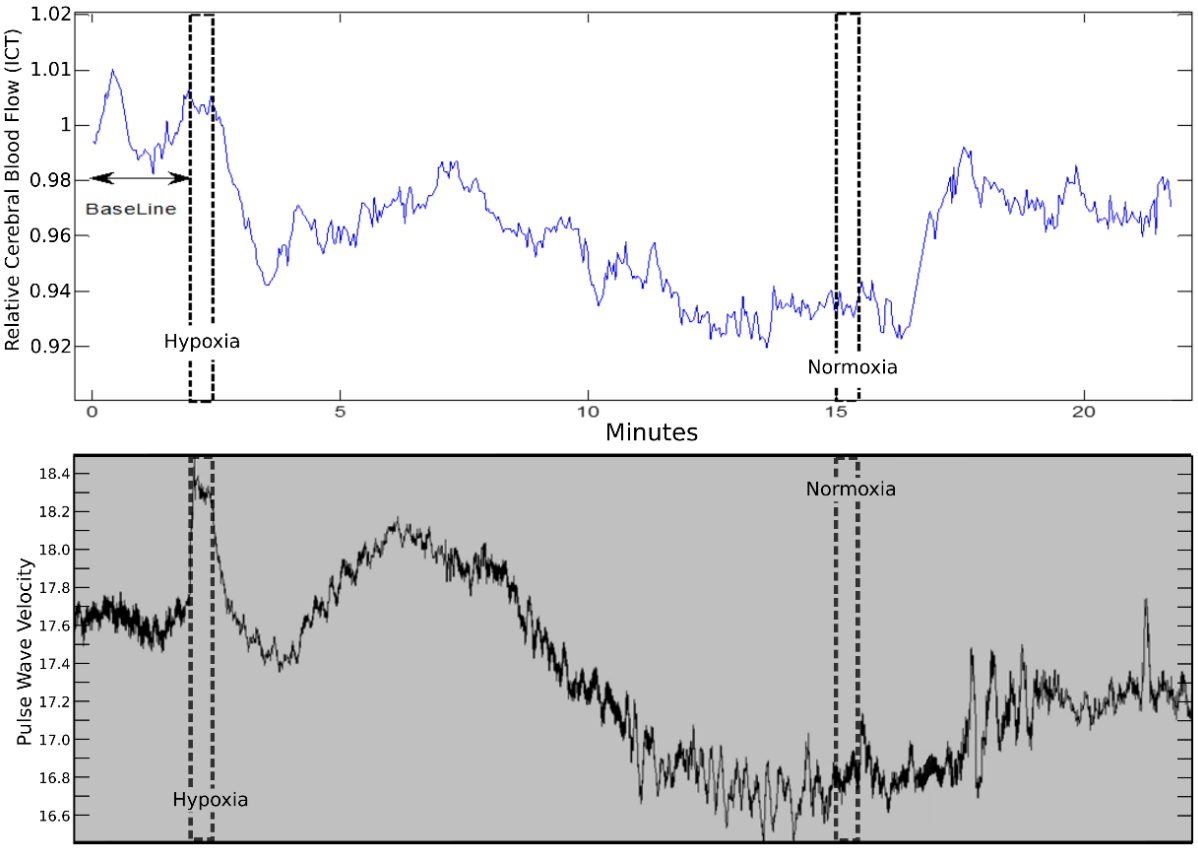

Figure 4. 23 (top) LSCI ICT flow trace (bottom) Aorta blood pressure derived Pulse Wave Velocity (PWV) trace during the 12% hypoxia event. "Hypoxia" indicates the start of 12% Hypoxia. "Normoxia" indicates the moment of back to normal oxygen level.

4.4.9. Experimental Results of Instantaneous Pulsatility Pattern

In this session, the developed system was used to acquire cerebral pulsatility patterns of rat. Rats' heart rates are typically around 300-400 beats per minute, which is about 5 times more than human. Another fact is that the pulsatility pattern in the brain has smaller dynamic variation when compared to systemic arteries. In systemic arteries, the flow fluctuates from 0 to its highest velocity, where the flow within the brain has a constant flow with a small fluctuation on top of it.

To resolve the feature of rats' pulsatility, a hundred data points are required within one cardio cycle. Since, the single frame of spatial contrast map often contains high level of speckle noise, averaging a stack of images is a common practice to discriminate the speckle noise. To resolve individual pulses, the choice of sample rates

between 966 Hz, 1869 Hz, and 3500 Hz within a 2 seconds acquisition period demonstrated.

At 966 Hz, a window size of 698 x 784 pixels is obtained which contains the ***a4*** artery, ***a5*** artery and ***v3*** vein. The manually selected polygram covers the vessel to produce an average flow rate and it becomes one single data point. A size of 20 data points moving-average filter was applied. The result in Figure 4.24 shows the comparison between the time traces of the ***a4*** artery and ***v3*** vein. The results show a distinguishable rise time difference between ***a4*** artery and ***v3*** vein. The contour also shows the feature of small dicrotic notch and diastolic peak.

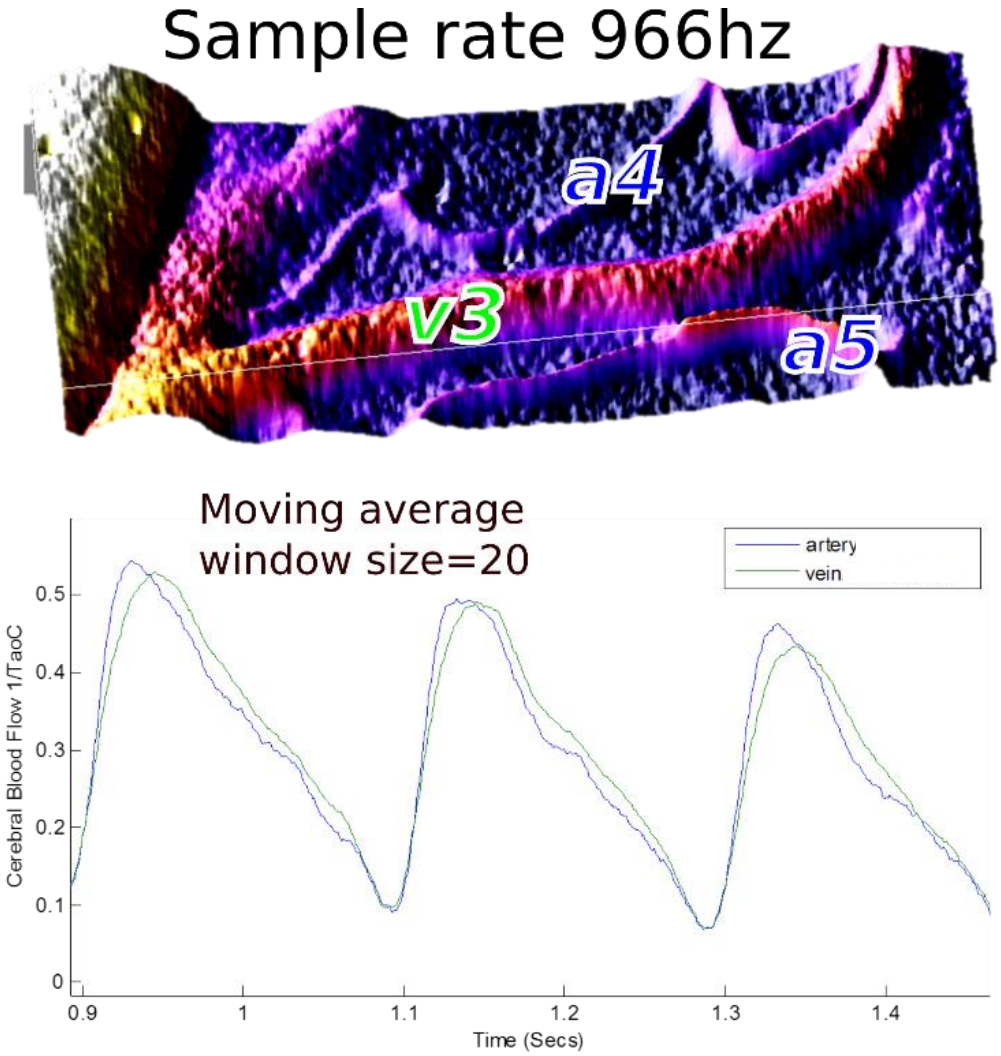

*Figure 4. 24 (top) surface plot of 1/contrast map (bottom) the time traces of the **a4** artery and **v3** vein ICT values captured at 966 Hz*

At 1869 Hz, a window size of 822 x143 pixels was obtained. The results of the ***a5*** artery and ***v3*** vein with a moving-average window size of 30 data points are plotted in Figure 4.25. The results also show a distinguishable rise time and fall time differences, but with an improved visibility of dicrotic notches and diastolic peaks.

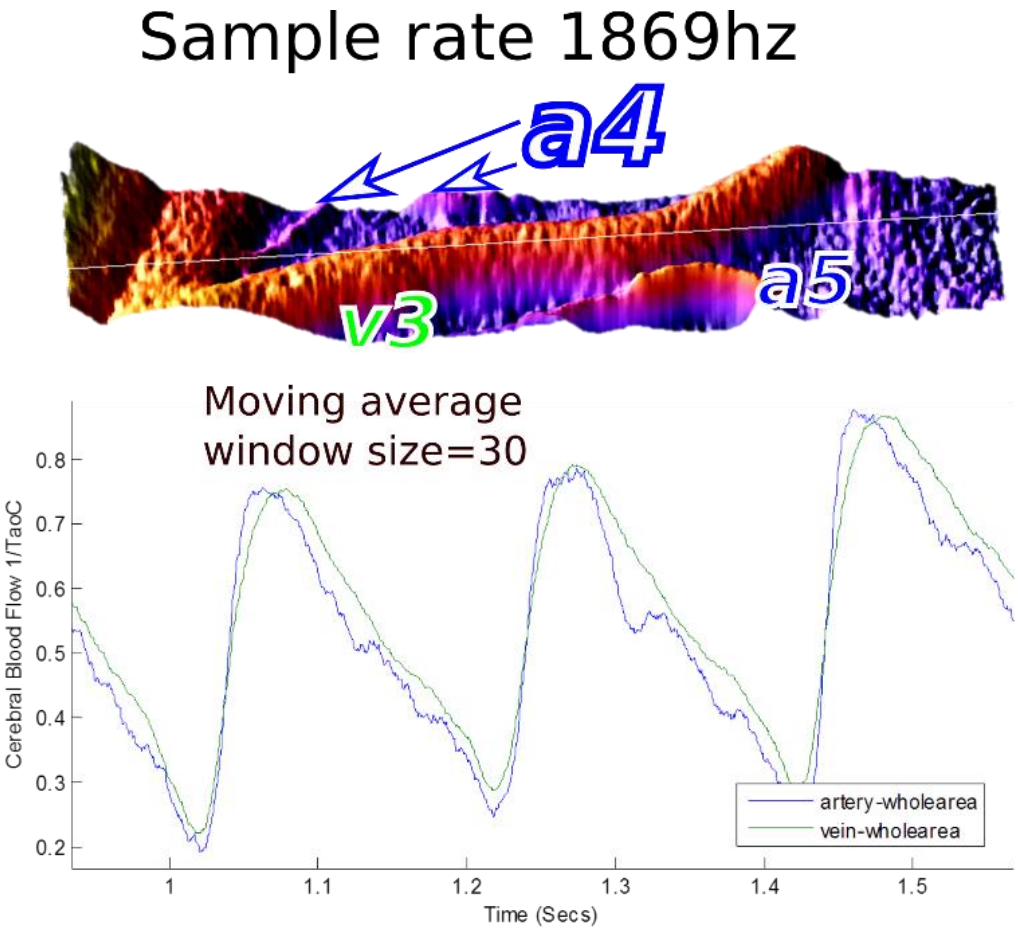

*Figure 4. 25 (top) surface plot of 1/contrast map (bottom) the time traces of the **a5** artery and **v3** vein ICT values captured at 1869 Hz*

At 3500 Hz, the windows size is 698 x 90 pixels, and it contains part of ***v3*** anf a portion of ***a4***. Since the number of pixels on ***a4*** is less, the spatial averaging of ***a4*** signal does not discriminate the speckle noise. It requires more temporal averaging. Figure 4.25 shows the results after applying the moving-average filter with the window size of 50. The artery ***a4*** signal appears to be noisy compared to the artery signal captured under the sample rate of 1869 Hz.

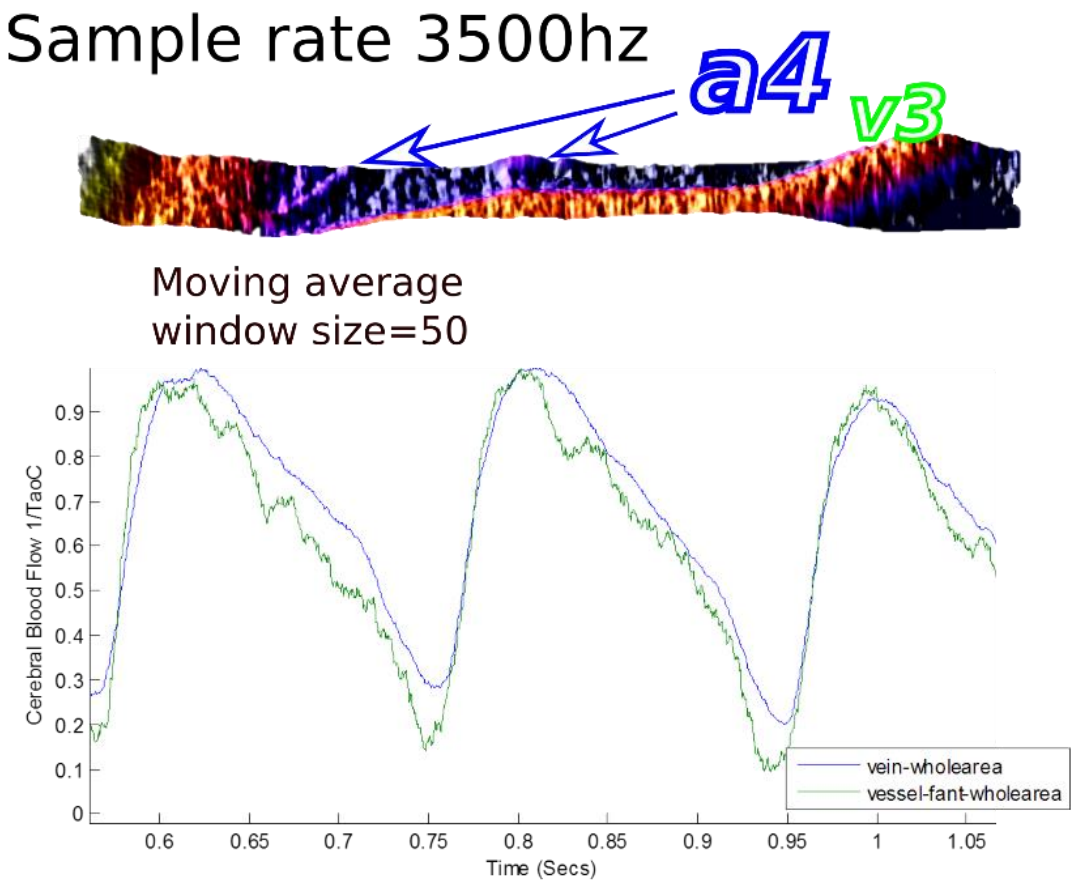

*Figure 4. 26 (top) surface plot of 1/contrast map (bottom) the time traces of the **a4** artery and **v3** vein ICT values captured at 3500 Hz*

4.4.10. Validation of Ensemble Average Algorithm

As chapter 3 stated the signal feature can be improved with the ensemble average. In this section, a validation of the ensemble average algorithm is shown with two sample data, ***a5*** artery and ***v3*** vein, collected under 1869 Hz.

Figure 4.24 shows that the iPeak software successfully detected all 10 peaks using the setting mentioned before in the Chapter 3.

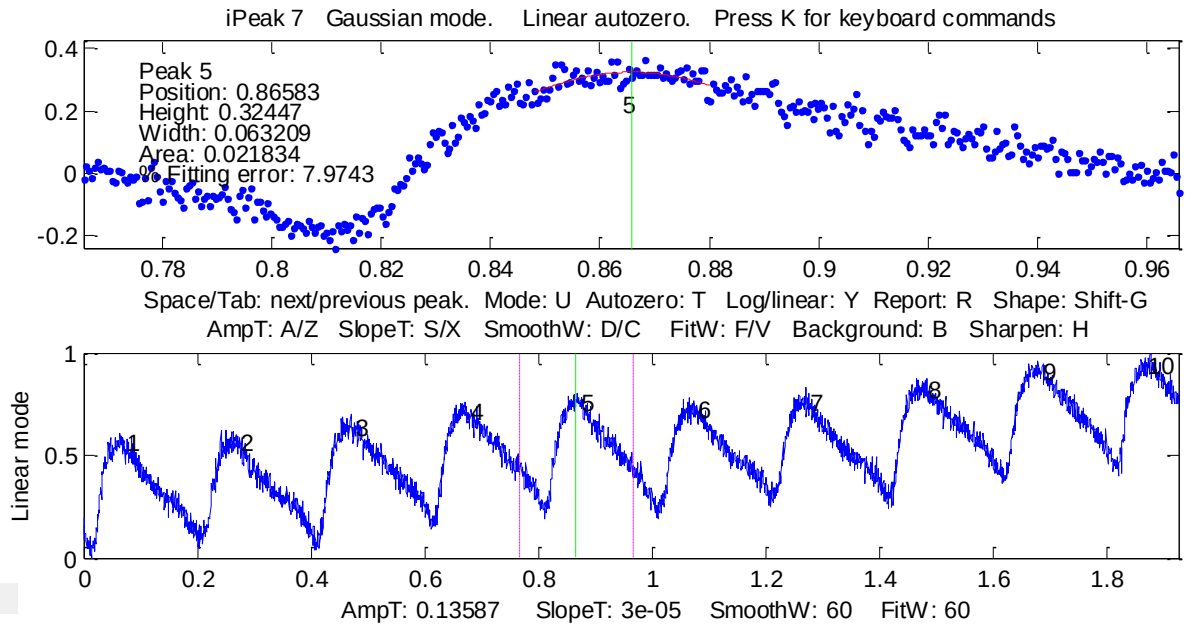

Figure 4. 27 Peak detection using iPeak Matlab package.

After successfully detecting the reference of timing, the original signals are preprocessed with auto zero, detrended and moving averaged. Figure 4.28 demonstrates the preprocessing of the signals.

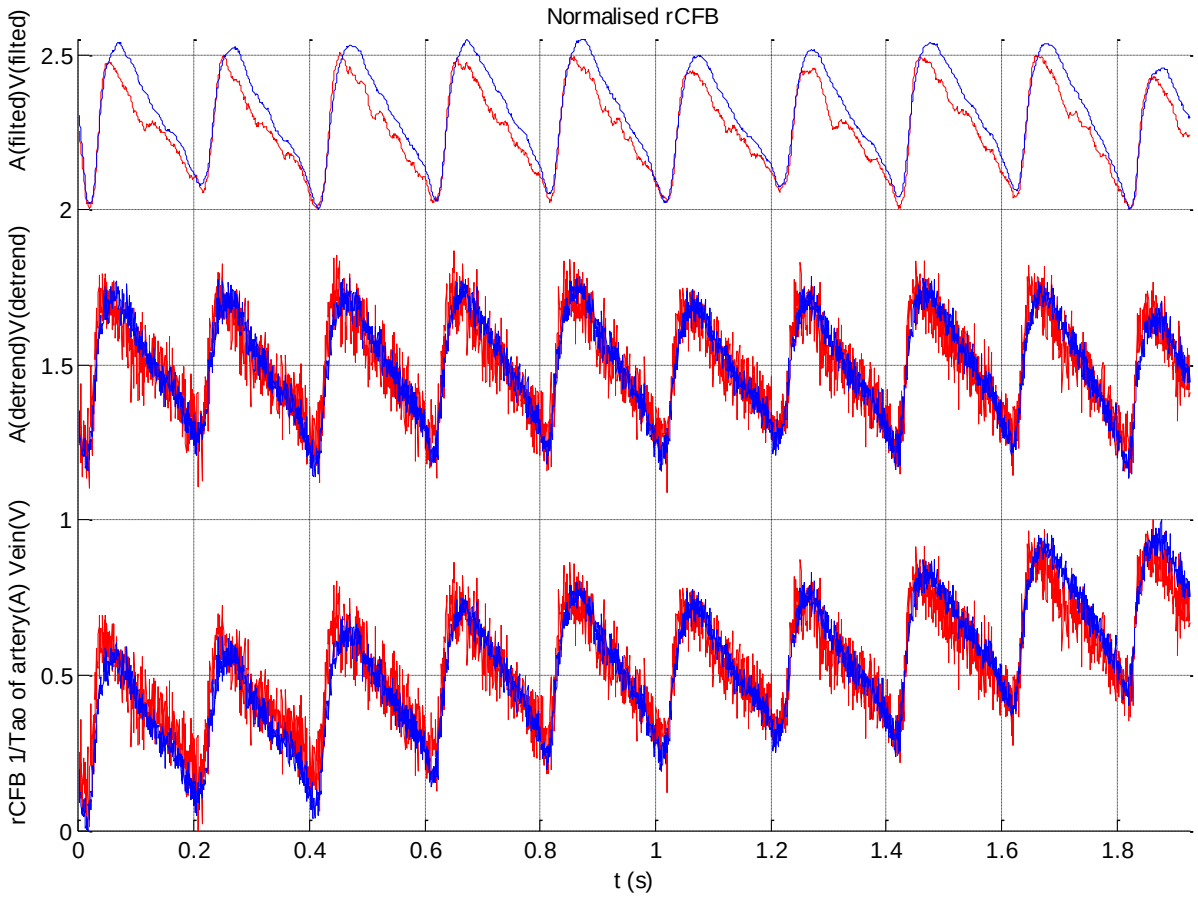

Figure 4. 28 Preprocessing of original signal

The reference of timing is used to do the segmentation. That results in 7 individual pulses. Each individual pulse is displayed in the 3D plot of Figure 4.29.

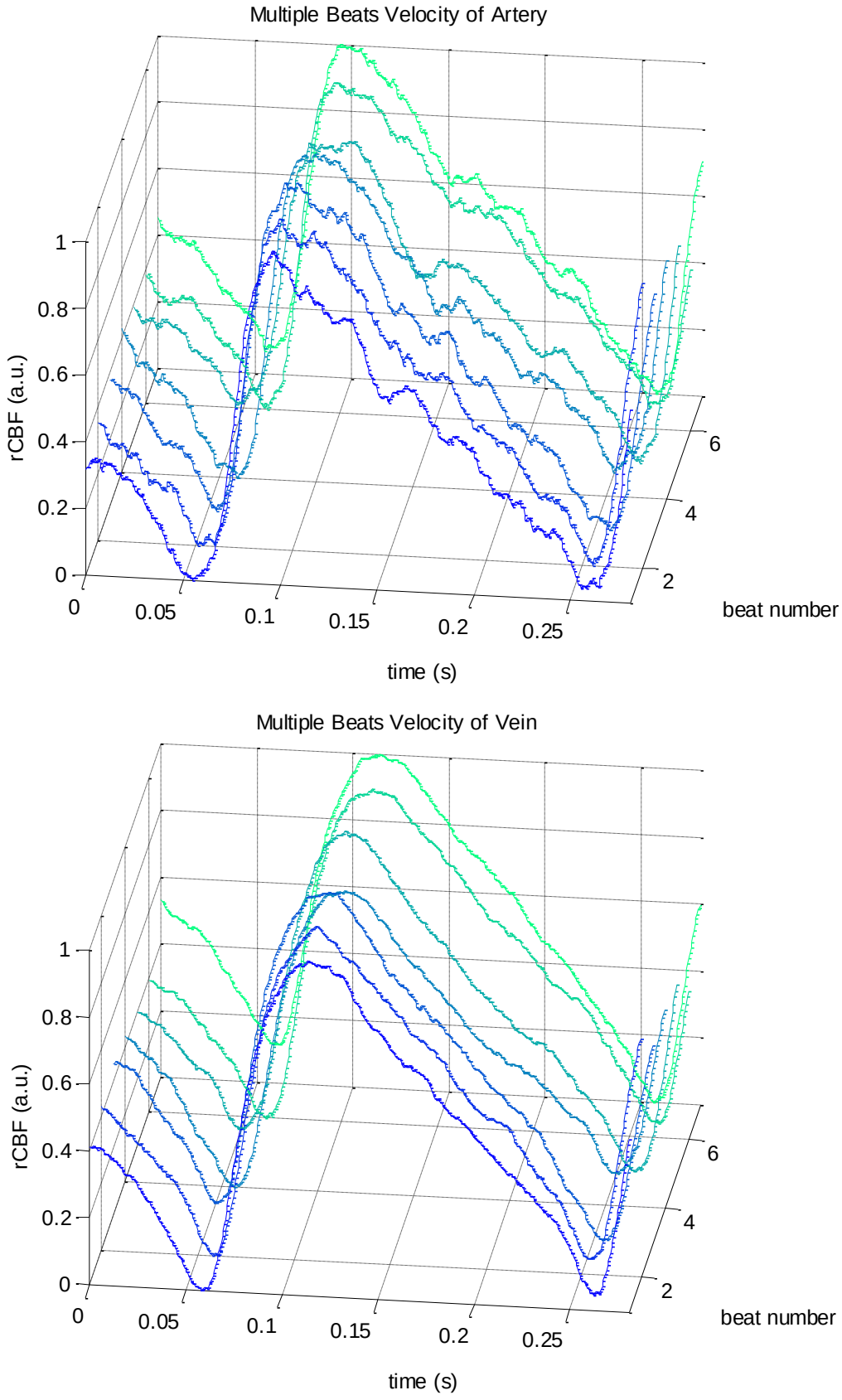

*Figure 4. 29 Segmentation of beats based on the reference of timing (top) beats of the **a4** artery (bottom) beats of the **v3** vein*

The results show the ensemble averages of pulsatile patterns in Figure 4.30 and the corresponding standard deviations.

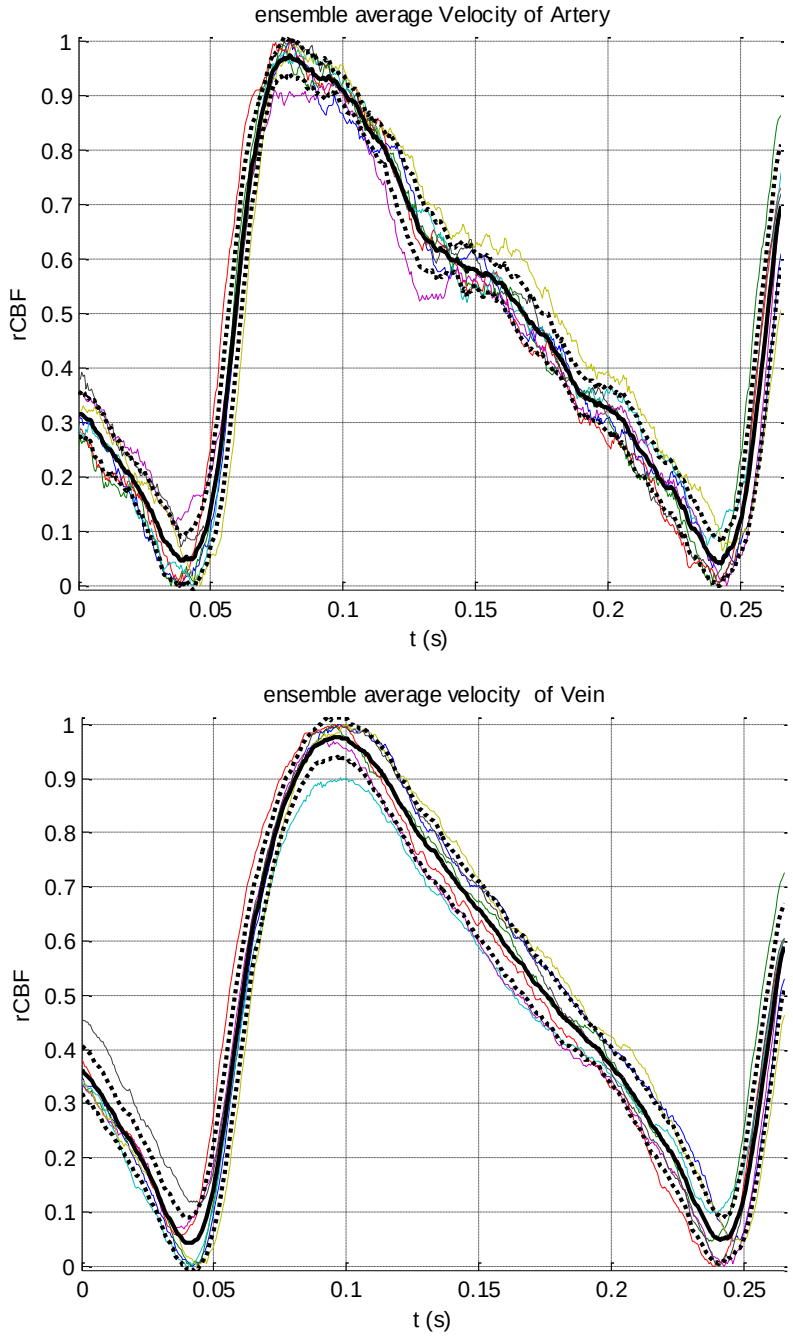

Figure 4. 30 Ensemble average of pulsatile pattern: (top) the a4 artery; (bottom) the v3 vein. Solid dark line is presenting the ensemble average. The dotted line is designated to one standard deviation away from the mean.

At the end, the ensemble averaged pulses of the ***a5*** artery and ***v3*** vein are plotted together for comparison in Figure 4.28. The ***v3*** vein's ensemble averaged

result shows a smooth pattern, while the ***a5*** artery's result shows a clear visibility of the dicrotic notch and the diastolic peak.

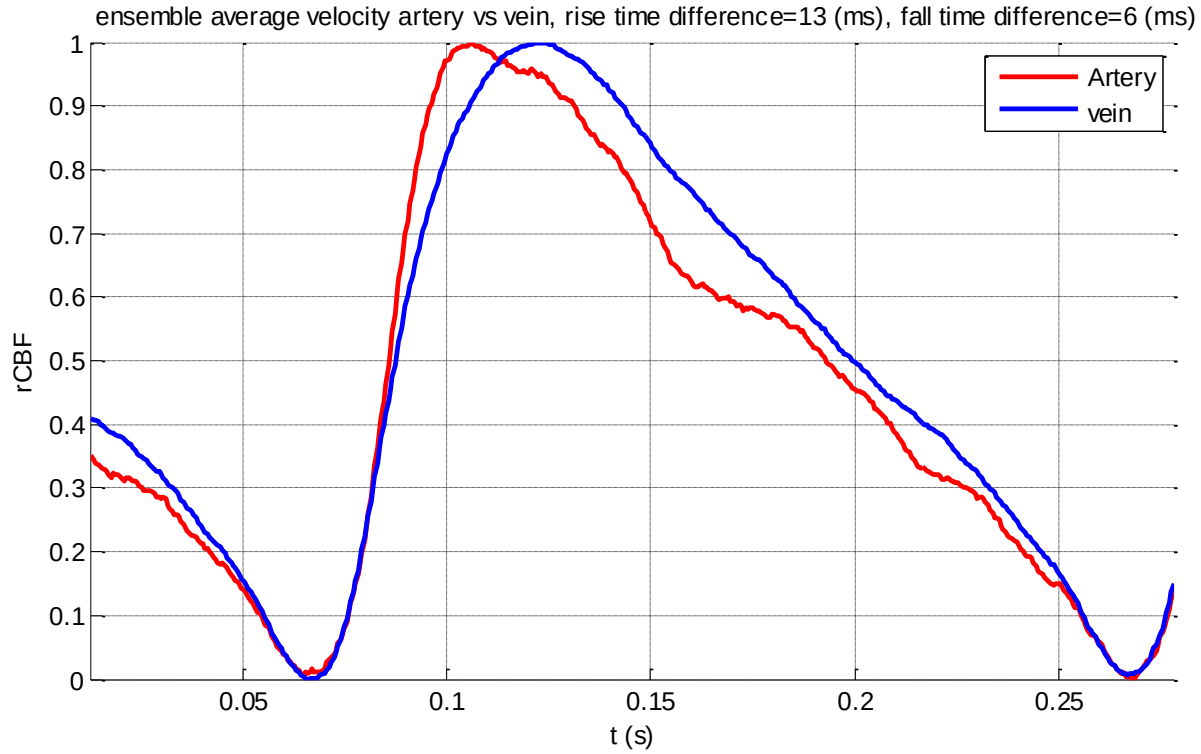

Figure 4. 31 The ensemble averaged pulse of a5 artery and v3 vein.

4.4.11. Experimental Results of Dynamic Properties of Pulsatility Patterns

To measure the rise time and fall time accurately, the ratio of lower boundary and upper boundary are set at 10% and 90 % of maximum. The rise time of ***a5*** artery is 20 ms and fall time is 125 ms.

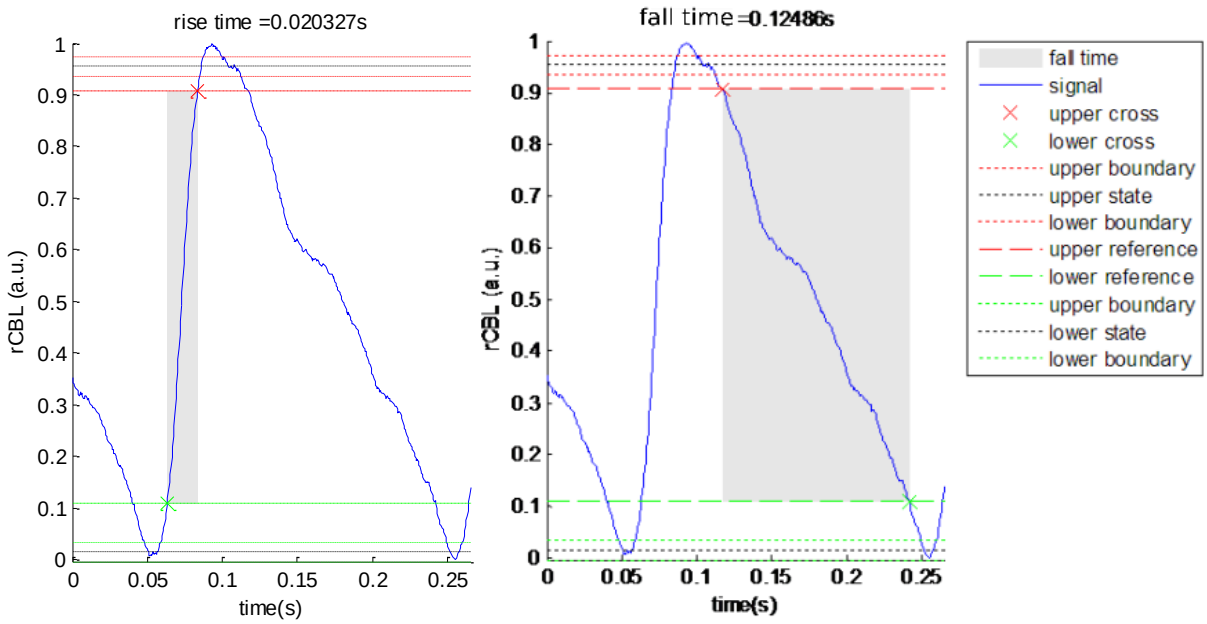

*Figure 4. 32 Rise time and fall time of **a5** artery ensemble average pulsatile pattern.*

The rise time of ***v3*** vein, is 33 ms and fall time is 119 ms.

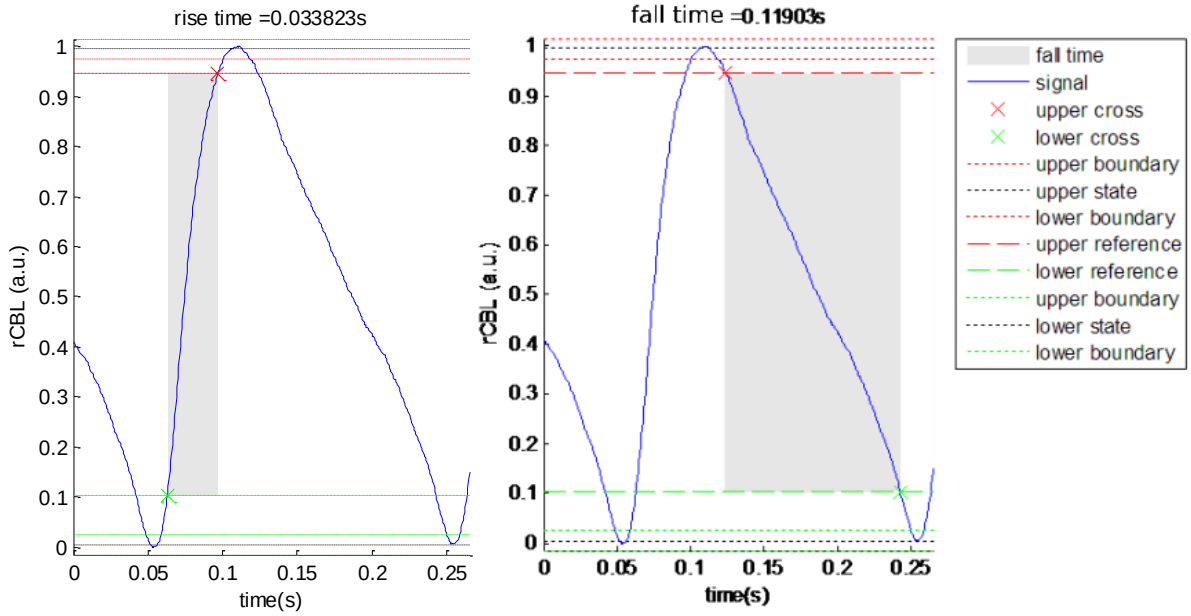

*Figure 4. 33 Rise time and fall time of **v3** vein ensemble average pulsatile pattern.*

In comparison, the ***a5*** artery rises 13ms faster than ***v3*** vein, and it takes 6ms longer for ***a5*** artery to fall below the lower boundary.

4.4.12. Experimental Results of Vascular Stiffness Estimates

In this section, the 2nd order derivative of pulsatile pattern is calculated based on the data of the ***a5*** artery and the ***v3*** vein. The results of the 2nd order derivative of pulsatile patterns is shown in Figure 4.34.

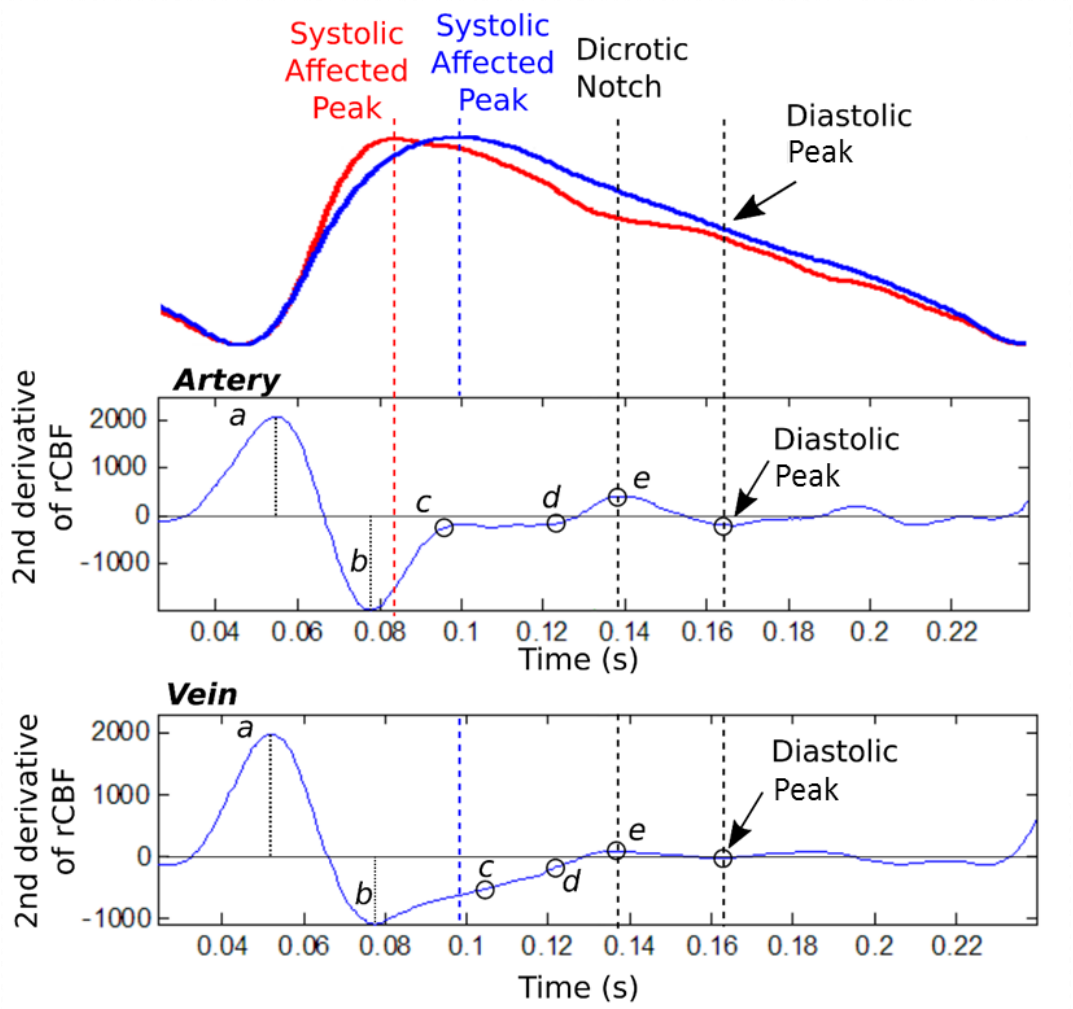

*Figure 4. 34 (top) Ensemble average of pulsatile pattern of a5 artery and v3 vein (middle) 2nd order derivative of pulsatile flow of the **a5** artery (bottom) 2nd order derivative of the **v4** pulsatile flow of vein.*

The increased vascular stiffness index (IVSI, b/a ratio) and the decreased vascular stiffness index (DVSI, c/a ratio) are both calculated based on the data of the ***a5*** artery and the ***v3*** vein. The results show the ***a5*** artery has IVSI of 0.95 and the ***v3*** vein has an IVSI of 0.74. On the other hand, the ***a5*** artery has DVSI of 0.125 and the ***v3*** vein has a DVSI of 0.35.

The results are coherent with the features reported in [61]. In particular, the 2nd order derivative of rCBF has all the wave components that the 2nd order derivative of Photoplethysmogram or Accelerated Photoplethysmogram (APG) has as mentioned in section 2.10. In terms of timing, since the systole affected peak and the dicrotic notch are determined by the ventricular activity, the results show a-wave, b-wave, d-wave and e-wave of the ***a5*** artery and the ***v3*** vein all are happening at the same moment,. The results of stiffness indices correlated well with Takazawa's report [62], since the wall of arteries are usually more rigid compared to veins.

Chapter 5

Conclusion and Future Works

5.1 Conclusion

The fast in vivo blood flow monitoring device developed in this project, in addition to monitoring mean blood flow activity, can measure the pulsatile pattern of blood flow and provide dynamic properties of vessels which can potentially relate to the physical characteristics of vessels.

In this research, shorter exposure time settings, 0.25ms and 0.075ms, were used to demonstrate the linear relationship between our device flow estimates and controlled flow rates using a microfabricated channel. This result allows LSCI to be used in higher sample rate regimes and enables LSCI to monitor physical oscillation of cerebral blood flow. Our results show a clear difference between the dynamical properties of arterial and venous flows. Moreover, vascular stiffness indices were evaluated by analyzing second derivative of pulsatile cerebral blood flow measurements. In our experiment both stiffness indices suggest that the selected arteriole has a higher vascular stiffness than the venule under study.

The original goals of this project are listed below:

Monitoring the spatial and temporal variations of relative mean flow

The developed system was used to monitor hemodynamic responses in two functional brain activation experiments in rat cerebral cortex. In one experiment of phenylephrine tail injection, we observed the subsequent cerebral blood increases after the injection of phenylephrine. In another experiment, the hemodynamic

response of 12% hypoxia experiment monitored by this system was well correlated with the pulse wave velocity derived from the aorta blood pressure.

Spontaneous monitoring of pulse wave contour within individual vessels

We used the developed system to monitor two selected vessels spontaneously. The processed data shows clear pulsatile contours. The pulsatile contours of vessels are similar to the results coming from peripheral vasculature found in the literature.

Analysis of vascular stiffness in individual vessels

We used the second derivative of cerebral blood flow signals to evaluate the dynamical properties of pulsatile flow. Two blood flow indices were used to describe the physical properties of vessels.

5.2 Future Work

There are some suggestions given below to improve the hardware and software of the system.

Real-Time LSCI

The current LSCI system only allows raw speckle images to be collected during experiments, and processed after the experiment. A modified Labview software integrated with C++ dynamic linking library (DLL), which can process spatial contrast analysis algorithm efficiently, can enable us to implement real time LSCI systems. It will provide real time blood flow monitoring, and benefit the operator with vascular visualization, so the navigation in the region of interest becomes easier. The real time blood flow imaging greatly facilitates aligning the illumination or the adjustment of the imaging device such as the orientation of the polarization filter.

Establishing New Vascular Characterized Indices

By recording more pulsatile blood flow data to develop a database and taking more variables such as rise time, fall time, heart rate, vessel diameter, features of second derivative rCBF into account, a custom cerebral vascular stiffness index can be created.

References

[1] G. Michelson and B. Schmauss, “Two dimensional mapping of the perfusion of the retina and optic nerve head,” *Br. J. Ophthalmol.*, vol. 79, no. 12, pp. 1126–32, Dec. 1995.

[2] J. D. Briers, “Laser Doppler, speckle and related techniques for blood perfusion mapping and imaging,” *Physiol. Meas.*, vol. 22, no. 4, pp. R35–66, Nov. 2001.

[3] S. A. Pape, C. A. Skouras, and P. O. Byrne, “An audit of the use of laser Doppler imaging (LDI) in the assessment of burns of intermediate depth,” *Burns*, vol. 27, no. 3, pp. 233–9, May 2001.

[4] A. Serov and T. Lasser, “High-speed laser Doppler perfusion imaging using an integrating CMOS image sensor,” *Opt. Express*, vol. 13, no. 17, pp. 6416–28, Aug. 2005.

[5] J. rgen Czarske, L. B ttner, T. Razik, and H. M ller, “Boundary layer velocity measurements by a laser Doppler profile sensor with micrometre spatial resolution,” *Meas. Sci. Technol.*, vol. 13, no. 12, pp. 1979–1989, 2002.

[6] L. Büttner and J. Czarske, “Determination of the axial velocity component by a laser-Doppler velocity profile sensor,” *J. Opt. Soc. Am. A. Opt. Image Sci. Vis.*, vol. 23, no. 2, pp. 444–454, 2006.

[7] L. Büttner, J. Czarske, and H. Knuppertz, “Laser-Doppler velocity profile sensor with submicrometer spatial resolution that employs fiber optics and a diffractive lens,” *Appl. Opt.*, vol. 44, no. 12, pp. 2274–2280, 2005.

[8] S. Yuan, A. Devor, D. A. Boas, and A. K. Dunn, “Determination of optimal exposure time for contrast imaging,” vol. 44, no. 10, pp. 1823–1830, 2005.

[9] A. K. Prasad, “Stereoscopic particle image velocimetry,” *Exp. Fluids*, vol. 29, no. 2, pp. 103–116, 2000.

[10] M. L. Smith, D. S. Long, E. R. Damiano, and K. Ley, “Near-wall micro-PIV reveals a hydrodynamically relevant endothelial surface layer in venules in vivo,” *Biophys. J.*, vol. 85, no. 1, pp. 637–45, Jul. 2003.

[11] H. Zheng, L. Liu, L. Williams, J. R. Hertzberg, C. Lanning, and R. Shandas, “Real time multicomponent echo particle image velocimetry technique for opaque flow imaging,” *Appl. Phys. Lett.*, vol. 88, no. 26, pp. 86–89, 2006.

[12] P. Vennemann, R. Lindken, and J. Westerweel, “In vivo whole-field blood velocity measurement techniques,” *Exp. Fluids*, vol. 42, no. 4, pp. 495–511, Mar. 2007.

[13] W. R. Bauer, K. H. Hiller, P. Galuppo, S. Neubauer, J. Köpke, A. Haase, C. Waller, and G. Ertl, “Fast high-resolution magnetic resonance imaging

demonstrates fractality of myocardial perfusion in microscopic dimensions," *Circ. Res.*, vol. 88, no. 3, pp. 340–6, Feb. 2001.

[14] M. Markl, F. P. Chan, M. T. Alley, K. L. Wedding, M. T. Draney, C. J. Elkins, D. W. Parker, R. Wicker, C. A. Taylor, R. J. Herfkens, and N. J. Pelc, "Time-resolved three-dimensional phase-contrast MRI," *J. Magn. Reson. Imaging*, vol. 17, no. 4, pp. 499–506, Apr. 2003.

[15] R. Nezafat, P. Kellman, J. A. Derbyshire, and E. R. McVeigh, "Real-time blood flow imaging using autocalibrated spiral sensitivity encoding," *Magn. Reson. Med.*, vol. 54, no. 6, pp. 1557–61, Dec. 2005.

[16] A. Devor, S. Sakadžić, V. J. Srinivasan, M. a Yaseen, K. Nizar, P. a Saisan, P. Tian, A. M. Dale, S. a Vinogradov, M. A. Franceschini, and D. a Boas, "Frontiers in optical imaging of cerebral blood flow and metabolism," *J. Cereb. Blood Flow Metab.*, vol. 32, no. 7, pp. 1259–76, Jul. 2012.

[17] J. W. Goodman, "Some fundamental properties of speckle," *J. Opt. Soc. Am.*, vol. 66, no. 11, p. 1145, 1976.

[18] J. C. Dainty, "Some Statistical Properties of Random Speckle Patterns in Coherent and Partially Coherent Illumination," *Optica Acta: International Journal of Optics*, vol. 17, no. 10. pp. 761–772, 1970.

[19] A. Fercher and J. Briers, “Flow visualization by means of single-exposure speckle photography,” *Opt. Commun.*, 1981.

[20] J. Goodman, “Statistical properties of laser speckle patterns,” *Laser speckle Relat. Phenom.*, 1975.

[21] R. Bonner and R. Nossal, “Model for laser Doppler measurements of blood flow in tissue.,” *Appl. Opt.*, vol. 20, pp. 2097–2107, 1981.

[22] R. Bandyopadhyay, A. S. Gittings, S. S. Suh, P. K. Dixon, and D. J. Durian, “Speckle-visibility spectroscopy: A tool to study time-varying dynamics,” 2008.

[23] a K. Dunn, H. Bolay, M. a Moskowitz, and D. a Boas, “Dynamic imaging of cerebral blood flow using laser speckle,” *J. Cereb. Blood Flow Metab.*, vol. 21, no. 3, pp. 195–201, Mar. 2001.

[24] T. Durduran, T. Durduran, M. G. Burnett, M. G. Burnett, Y. Guoqiang, Y. Guoqiang, C. Zhou, C. Zhou, D. Furuya, D. Furuya, A. G. Yodh, A. G. Yodh, J. a Detre, J. a Detre, J. H. Greenberg, and J. H. Greenberg, “Spatiotemporal Quantification of Cerebral Blood Flow During Functional Activation in Rat Somatosensory Cortex Using Laser-Speckle Flowmetry,” *J. Cereb. Blood Flow Metab.*, vol. 24, pp. 518–525, 2004.

[25] H. Bolay, U. Reuter, A. K. Dunn, Z. Huang, D. a Boas, and M. a Moskowitz, “Intrinsic brain activity triggers trigeminal meningeal afferents in a migraine model,” *Nat. Med.*, vol. 8, no. 2, pp. 136–142, 2002.

[26] H. K. Shin, A. K. Dunn, P. B. Jones, D. a Boas, M. a Moskowitz, and C. Ayata, “Vasoconstrictive neurovascular coupling during focal ischemic depolarizations,” *J. Cereb. Blood Flow Metab.*, vol. 26, no. 8, pp. 1018–1030, 2006.

[27] J. Briers and S. Webster, “LASER SPECKLE CONTRAST ANALYSIS (LASCA): A NONSCANNING, FULL-FIELD TECHNIQUE FOR MONITORING CAPILLARY BLOOD FLOW,” *J. …*, vol. 1, no. 2, pp. 174–179, 1996.

[28] C. J. Stewart, R. Frank, K. R. Forrester, J. Tulip, R. Lindsay, and R. C. Bray, “A comparison of two laser-based methods for determination of burn scar perfusion: Laser Doppler versus laser speckle imaging,” *Burns*, vol. 31, no. 6, pp. 744–752, 2005.

[29] P. Li, S. Ni, L. Zhang, S. Zeng, and Q. Luo, “Imaging cerebral blood flow through the intact rat skull with temporal laser speckle imaging,” vol. 31, no. 12, pp. 1824–1826, 2006.

[30] S. J. Kirkpatrick, D. D. Duncan, and E. M. Wells-gray, “Detrimental effects of speckle-pixel size matching in laser speckle contrast imaging,” vol. 33, no. 24, pp. 2886–2888, 2008.

[31] D. D. Duncan, S. J. Kirkpatrick, and R. K. Wang, “Statistics of local speckle contrast,” *J. Opt. Soc. Am. A. Opt. Image Sci. Vis.*, vol. 25, no. 1, pp. 9–15, Jan. 2008.

[32] D. D. Duncan and S. J. Kirkpatrick, “Can laser speckle flowmetry be made a quantitative tool?,” *J. Opt. Soc. Am. A. Opt. Image Sci. Vis.*, vol. 25, no. 8, pp. 2088–2094, 2008.

[33] H. Cheng and T. Q. Duong, “Simplified laser-speckle-imaging analysis method and its application to retinal blood flow imaging,” vol. 32, no. 15, pp. 2188–2190, 2007.

[34] A. B. Parthasarathy, W. J. Tom, A. Gopal, X. Zhang, and A. K. Dunn, “Robust flow measurement with multi-exposure speckle imaging,” *Opt. Express*, vol. 16, no. 3, pp. 1975–89, Feb. 2008.

[35] D. D. Duncan, S. J. Kirkpatrick, J. C. Gladish, and S. a. Hurst, “Laser speckle contrast imaging for the quantitative assessment of flow,” *Proc. SPIE*, vol. 7176, pp. 717603–717603–8, 2009.

[36] P. B. Jones, H. K. Shin, D. a Boas, B. T. Hyman, M. a Moskowitz, C. Ayata, and A. K. Dunn, “Simultaneous multispectral reflectance imaging and laser speckle flowmetry of cerebral blood flow and oxygen metabolism in focal cerebral ischemia,” *J. Biomed. Opt.*, vol. 13, no. 4, p. 044007, 2008.

[37] V. Kalchenko, D. Israeli, Y. Kuznetsov, and A. Harmelin, “Transcranial optical vascular imaging,” *Sci. Rep.*, pp. 1–7, 2014.

[38] M. Gramer, D. Feuerstein, a. Steimers, M. Takagaki, T. Kumagai, M. Sué, S. Vollmar, M. Kohl-Bareis, H. Backes, and R. Graf, “Device for simultaneous positron emission tomography, laser speckle imaging and RGB reflectometry: Validation and application to cortical spreading depression and brain ischemia in rats,” *Neuroimage*, vol. 94, pp. 250–262, 2014.

[39] A. Rege, K. Murari, N. Li, and N. V Thakor, “Imaging Microvascular Flow Characteristics Using Laser Speckle Contrast Imaging,” pp. 1978–1981, 2010.

[40] A. K. Dunn, “Laser speckle contrast imaging of cerebral blood flow,” *Ann. Biomed. Eng.*, vol. 40, no. 2, pp. 367–377, 2012.

[41] S. M. S. Kazmi, A. J. Salvaggio, A. D. Estrada, M. a Hemati, N. K. Shaydyuk, E. Roussakis, T. a Jones, S. a Vinogradov, and A. K. Dunn, “Three-dimensional mapping of oxygen tension in cortical arterioles before and after occlusion,” *Biomed. Opt. Express*, vol. 4, no. 7, pp. 1061–73, 2013.

[42] S. M. S. Kazmi, L. M. Richards, C. J. Schrandt, M. a Davis, and A. K. Dunn, “Expanding applications, accuracy, and interpretation of laser speckle contrast imaging of cerebral blood flow,” *J. Cereb. Blood Flow Metab.*, no. February, pp. 1–9, 2015.

[43] K. J. Barnard, “Random laser speckle based modulation transfer function measurement of midwave infrared focal plane arrays,” *Opt. Eng.*, vol. 51, no. 8, p. 083601, 2012.

[44] M. FRANÇON, *Laser Speckle and Applications in Optics*. Elsevier, 1979.

[45] J. Senarathna, A. Rege, N. Li, and N. V Thakor, “Laser Speckle Contrast Imaging: theory, instrumentation and applications,” *IEEE Rev. Biomed. Eng.*, vol. 6, pp. 99–110, Jan. 2013.

[46] L. M. Richards, E. L. Towle, D. J. Fox, and A. K. Dunn, “Intraoperative laser speckle contrast imaging with retrospective motion correction for quantitative assessment of cerebral blood flow,” *Neurophotonics*, vol. in press, 2014.

[47] P. Miao, H. Lu, Q. Liu, Y. Li, and S. Tong, “Laser speckle contrast imaging of cerebral blood flow in freely moving animals,” *J. Biomed. Opt.*, vol. 16, p. 090502, 2011.

[48] M. Draijer, E. Hondebrink, T. van Leeuwen, and W. Steenbergen, “Review of laser speckle contrast techniques for visualizing tissue perfusion,” *Lasers Med. Sci.*, vol. 24, no. 4, pp. 639–51, Jul. 2009.

[49] J. D. Briers and S. Webster, “Quasi real-time digital version of single-exposure speckle photography for full-field monitoring of velocity or flow fields,” *Opt. Commun.*, vol. 116, no. 1–3, pp. 36–42, 1995.

[50] J. C. Ramirez-San-Juan, J. S. Nelson, and B. Choi, “Comparison of Lorentzian and Guassian based approaches for laser speckle imaging of blood flow dynamics,” in *Biomedical Optics*, 2006, pp. 607924–607924–4.

[51] D. D. Duncan, S. J. Kirkpatrick, and J. C. Gladish, “What is the proper statistical model for laser speckle flowmetry?,” *Complex Dyn. Fluctuations Biomed. Photonics V. Proc. SPIE*, vol. 6855, no. 2, pp. 685502–685502–7, 2008.

[52] D. a Boas and A. K. Dunn, “Laser speckle contrast imaging in biomedical optics,” *J. Biomed. Opt.*, vol. 15, no. 1, p. 011109, 2010.

[53] M. a Davis, S. M. S. Kazmi, and A. K. Dunn, “Imaging depth and multiple scattering in laser speckle contrast imaging,” *J. Biomed. Opt.*, vol. 19, no. 8, p. 86001, 2014.

[54] H. He, Y. Tang, F. Zhou, J. Wang, Q. Luo, and P. Li, “Lateral laser speckle contrast analysis combined with line beam scanning illumination to improve the sampling depth of blood flow imaging.,” *Opt. Lett.*, vol. 37, no. 18, pp. 3774–6, Sep. 2012.

[55] S. J. Kirkpatrick, D. D. Duncan, and E. M. Wells-Gray, “Detrimental effects of speckle-pixel size matching in laser speckle contrast imaging,” *Opt. Lett.*, vol. 33, no. 24, pp. 2886–8, Dec. 2008.

[56] M. Martínez-Ripoll, “Scattering and diffraction,” *Churchill College, Cambridge*, 1996. [Online]. Available: http://www.xtal.iqfr.csic.es/Cristalografia/parte_05-en.html. [Accessed: 13-Jul-2015].

[57] L. M. Richards, S. M. S. Kazmi, J. L. Davis, K. E. Olin, and A. K. Dunn, “Low-cost laser speckle contrast imaging of blood flow using a webcam,” *Biomed. Opt. Express*, vol. 4, no. 10, pp. 2269–83, Jan. 2013.

[58] N. Li, X. Jia, K. Murari, R. Parlapalli, A. Rege, and N. V. Thakor, “High spatiotemporal resolution imaging of the neurovascular response to electrical stimulation of rat peripheral trigeminal nerve as revealed by in vivo temporal laser speckle contrast,” *J. Neurosci. Methods*, vol. 176, no. 2, pp. 230–236, 2009.

[59] H. Cheng, Q. Luo, S. Zeng, S. Chen, J. Cen, and H. Gong, “Modified laser speckle imaging method with improved spatial resolution,” *J. Biomed. Opt.*, vol. 8, no. 3, pp. 559–64, Jul. 2003.

[60] A. B. Parthasarathy, S. M. S. Kazmi, and A. K. Dunn, “Quantitative imaging of ischemic stroke through thinned skull in mice with Multi Exposure Speckle Imaging,” *Biomed. Opt. Express*, vol. 1, no. 1, pp. 246–259, Jan. 2010.

[61] M. Elgendi, “On the Analysis of Fingertip Photoplethysmogram Signals,” *Curr. Cardiol. Rev.*, vol. 8, no. 1, pp. 14–25, 2012.

[62] K. Takazawa, N. Tanaka, M. Fujita, O. Matsuoka, T. Saiki, M. Aikawa, S. Tamura, and C. Ibukiyama, “Assessment of vasoactive agents and vascular aging by the second derivative of photoplethysmogram waveform,” *Hypertension*, vol. 32, no. 2, pp. 365–370, 1998.

[63] I. Imanaga, H. Hara, S. Koyanagi, and K. Tanaka, “Correlation between wave components of the second derivative of plethysmogram and arterial distensibility,” *Jpn. Heart J.*, vol. 39, no. 6, pp. 775–784, 1998.

[64] T. O. Haver, “A Pragmatic Introduction to Signal Processing,” pp. 1–121, 2014.

[65] W. S. Rasband, “ImageJ,” *National Institutes of Health, Bethesda, Maryland, USA*. [Online]. Available: http://imagej.nih.gov/ij/, 1997-2015.